Study of corrosion mechanism of new zircaloys

Haixia Zhang

Université de Grenoble – Grenoble

Xi'an Jiaotong University – Xi'an

PhD Thesis

To be graduate of

Docteur de l'Université de Grenoble, Spécialité Physique des Matériaux
&
Doctor of the Xi'an Jiaotong University

Presented by

ZHANG Haixia

Study of corrosion mechanism of new zircaloys

Xi'an, November 20th 2009

Jury :

LI Zhongkui	Research Director at NIN	Reporter
CHATEIGNER Daniel	Professor at ENSICAEN	Reporter
SUN Jun	Dean, Professor at Xi'an Jiaotong University	Examinator
XUE Xiangyi	Professor, Head of «SuperCrystal Lab.»	Examinator
ORTEGA Luc	Researcher at Néel Institut	Examinator
ZHOU Lian	Professor at NPU, Doctor Honoris Causa UJF	Supervisor
FRUCHART Daniel	Research Director at Néel Institut	Supervisor
HLIL El Kébir	Assistant Professor at UJF	Supervisor

PhD thesis prepared at the Institut Néel, CNRS Grenoble, France
and at the Northwestern Institut for Non-ferrous Metal Research, Xi'an, China
in the framework of the French-Chinese International Associated Laboratory LAS2M.

Thanks

The present thesis was prepared both at Nortwestern Institute for Non Ferrous Metals, Xi'an (China) and at Institute Néel, CNRS, Grenoble (France) under the frame of the International Laboratory (LIA) LAS2M founded by the CNRS and the Chinese Academy of Sciences, gathering the two Institutes.

Thanks are due to Ambassy of France in Beijing which has granted all stays I made in Grenoble, France, so allowing the successful preparation of the thesis work.

The thesis is placed under the co-tutelle of the North-Western Polytechnic University (NPU) Xi'an China and the Université de Grenoble, France.

Thanks are due to Mr ZHOU Lian, Professor at NPU, Doctor Honoris Causa UJF, Chinese supervisor of the thesis, to Mr HLIL El Kébir, Assistant Professor at UJF, and Mr FRUCHART Daniel Research Director at Néel Institut, both French supervisors of the thesis.

Thanks are due to the members of the Jury who have accepted to report the thesis work: Mr LI Zhongkui, Research Director at NIN (China) and Mr CHATEIGNER Daniel, Professor at ENSICAEN (France).

Thanks are due to the members of the Jury who have accepted to evaluate the thesis work: Mr SUN Jun, Dean, Professor at University Jiaotong Xi', Mr XUE Xiangyi, Professor, Head of «Super Crystal-Lab», Mr ORTEGA Luc, Researcher at Néel Institut.

Thanks are due to all my colleagues at NIN, NPU, CNRS who have help, encouraged and support me, day by day, for the best achievement of the present work.

Thanks are due to all my friends in the Chinese and French Laboratories.

Outline

Chapter 1

Introduction

Chapter 1 Introduction

1.1 The development of nuclear power

The nuclear industry is the important application field of zirconium and zirconium alloys. The metallurgy industry of zirconium and zirconium alloys develops with the exploitation and using of nuclear energy.

The nuclear energy age commences with the discovering of the nuclear fission and the development of nuclear reactor pile realizes the using of the nuclear energy. The characteristic of nuclear energy is its high energy density. The using of nuclear energy can greatly decrease the exploitation of fossil fuel, thus alleviate the energy crisis. In addition, the nuclear power plants don't release CO_2, SO_2 and NO_x, so this can lighten the environment pollution and decrease the harm of global calefaction. Also the accident probability of nuclear power plant is very low [1,2]. Therefore, the nuclear power is a kind of high efficient, economical, safe and cleanly energy, and the final energy requirement of the human will depend on the nuclear energy.

The first test nuclear power plant was found in Soviet Russia in 1954 and the first commercial nuclear power plant was found in America in 1957. Nuclear industry has developed for more than half one of century, and the loading capability and the ability of furnishing power are enhancing steadily. At the end of 2004, there were 440 nuclear power plants in the whole world, 104 in American, 59 in France, 53 in Japan. The amount of nuclear generating electricity was 16% in the world [3].

In China, the nuclear power development started at the middle time of 1980's, but the design work started at 1970's. The first nuclear power plant (Qinshan nuclear power plant) was built in 1985. Its favoring run finished the nonnuclear power history of China. At present, there are 3 nuclear power plants in China: Qinshan nuclear power plant in Zhejiang province, Dayawan nuclear power plant in Guangdong province and Tianwan nuclear power plant in Jiangsu province. Another two new nuclear power plants are planning: Sanmen nuclear power plant in Zhejiang province and Yangjiang nuclear power plant in Guangdong province. The loading capability in China is 8.7 GW and the amount of furnishing power is 2.3%. China government proposed that the nuclear power should be developed greatly and the loading capability would reach 40 GW in 2020[4]. So the decrease of nuclear power cost will promote its great development. The best measure decreasing the nuclear power cost is to heighten fuel consume, prolong the changing fuel period. Thus the security and reliability of reactor pile are required, and the using problems of key materials in nuclear reactor pile are greatly noticed.

1.2 The nuclear reactor and fuel cladding

The reactor piles used at best are PWR. It is a thermal neutron reactor pile whose once cooling water is under the boil pressure (14 ~ 16 MPa). PWR reactor piles occupy 67.5% of the gross of nuclear power piles and 74.1% of the total power[1,5]. Because PWR has many advantages: 1) Mature technique and high security; 2) Low investment.

The reactor pile is the reaction equipment that can do fission reaction by controllable method. Fig. 1-1 is structural scheme of PWR. It
consists of pile core, reflected shell, control club, pile container and shield shell et al. The fuel subassembly is collected in the pile core, which consists of fuel core, cladding and port plug et al. Nuclear fuel core is the matter that arises the fission reaction in the reactor pile. The fuel core is packed in the cladding and becomes fuel assembly (Fig. 1-2). So the fuel assembly is the most important components in the reactor pile. It decides the security and economy of the reactor pile. However the using life of fuel assembly is close related to the properties of

cladding materials. The actions of cladding include: 1) Separating the fuel core and cooling water, preventing the chemical reaction between the fuel core and cooling water; 2) Stopping the transgression of fission productions, preventing the pollution of matter with radioactivity. It's the first safe barrier of the reactor pile; 3) Transferring the heat energy caused by the fission of fuel core to the refrigerant, and providing enough structure strength to make the fuel components remain the integrity of structure and the steady of size. Therefore, the cladding material is a kind of key material preparing the nuclear fuel components.

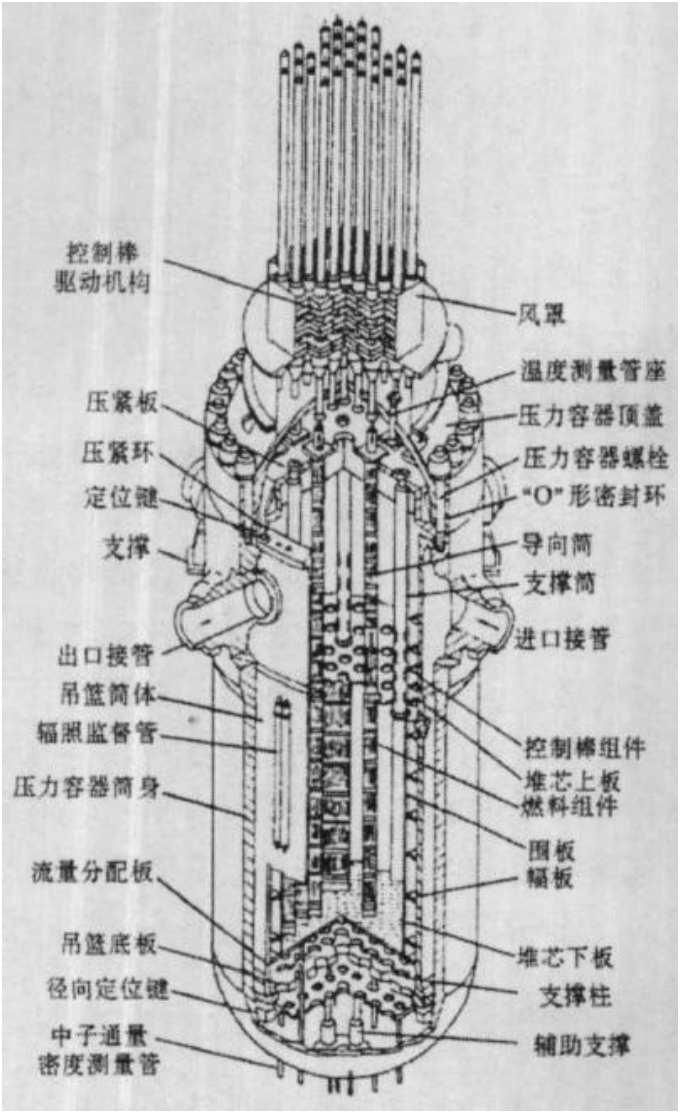

Fig.1-1 The structure scheme of PWR

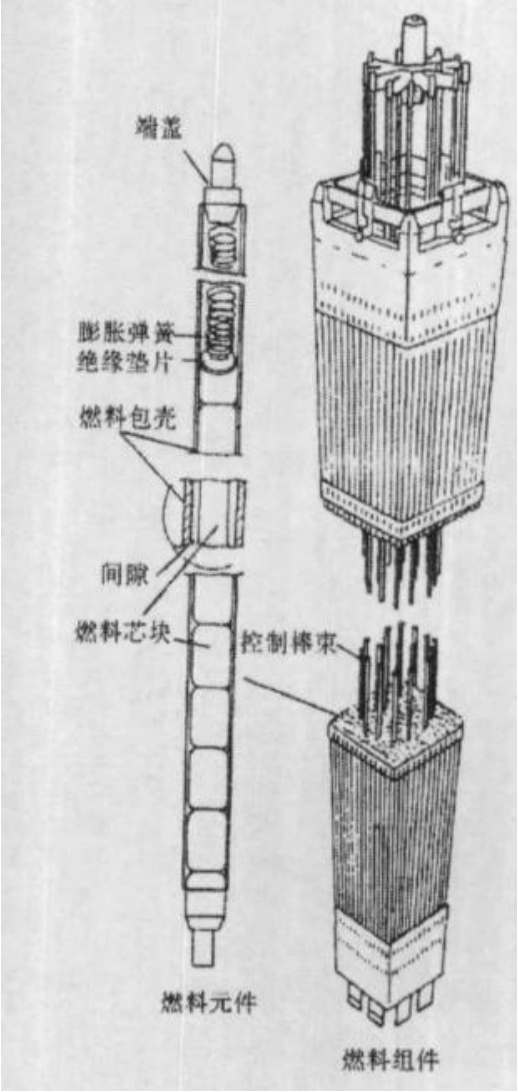

Fig. 1.2 The fuel assembly of PWR

1.3 The main problems of zirconium alloys cladding

Due to the small thermal neutron absorption section, good corrosion resistance in high temperature and pressure water and good high temperature strength et al, zirconium alloy is the only cladding material in the water-cooling nuclear reactor pile at present.

When the reactor pile runs, the cladding material works in the high temperature and pressure water and is corroded to ZrO_2, at the same time, Hydrogen is released. On the one hand, the cladding thickness reduces by the corrosion, thus the using life of fuel components is shortened; On the other hand, a part of hydrogen released by the corrosion reaction is absorbed by zirconium alloy, other hydrogen will precipitate to form hydride which makes zirconium alloys brittle [6,7]. There are many studies about the hydrogen weight gain performance [8-11]. The corrosion and hydrogen pickup are two important problems in the using of zirconium alloys. To reduce the nuclear power cost, the fuel consume has to be heightened. Thus how to improve the corrosion resistance of cladding material and reduce hydrogen pickup should be further studied.

1.4 The purpose, significance and content of this research

In general, after the corrosion resistance of zirconium alloys is improved, the corresponding hydrogen pickup is reduced. So the corrosion resistance of zirconium alloys is an important aspect exploiting new alloys. It is good for the choice of the alloying elements and adjusting of the heating treatment techniques to study the effects of alloying composition, precipitate, oxide crystal structure and stress distribution et al on the corrosion behaviours.

In this thesis, several aspects as follows are studied:

(1) Studying the effect of matrix microstructure (alloying element composition, the category and distribution of the precipitates) on the corrosion behaviours of zirconium alloys;

(2) Studying the effect of oxide crystal structure (phase transformation and stress distribution) on the corrosion behaviours of zirconium alloys;

(3) Doing the above studies using two kinds of water chemical conditions.

The three aspect studies are not isolated, and they are interdependent. Understanding the microstructure effect on the corrosion behaviour, this can provide the foundation to choose alloying elements while developing the new zirconium alloys; It is good to improve corrosion resistance and explore the corrosion mechanism t study the relation of oxide crystal structure and corrosion behaviours.

There are 9 chapters in this thesis.

Chapter 1 introduces the nuclear power development, main problems of zirconium alloys cladding in reactor pile and purpose, significance and content of this research.

Chapter 2 introduces the research summary of the corrosion resistance of zirconium alloys.

Chapter 3 introduces the study methods, including material, experimental conditions, equipments and the analysis methods et al.

Chapter 4 introduces corrosion kinetics of new zirconium alloys in different mediums.

Chapter 5 studies the effects of microstructure, including alloying element composition, precipitates, on corrosion resistance.

Chapter 6 studies how to the oxide structure change affect the corrosion resistance.

Chapter 7 is about the study of stress state in the oxide film; Chapter 8 discusses the corrosion resistance of new zirconium alloys.

Chapter 9 is a summary of the total thesis.

Chapter 2

Research summary of the corrosion resistance of zirconium alloys

Chapter 2 Research summary of the corrosion resistance of zirconium alloys

2.1 Brief introduction on zirconium alloys used in nuclear reactor

2.1.1 Basic characteristics of zirconium

Pure zirconium crystal is hcp structure at room temperature, and the c/a is 1.593. The crystal lattice constant is a=0.323 nm, c=0.515 nm [12]. At 865°C pure zirconium has an allotropic transformation from α hcp phase to β bcc phase. While cooling zirconium has martensite phase transform. The α-phase formed in sheet β crystal. The melting point of zirconium is 1860°C. The main physical properties of zirconium are given in Tab. 2-1.

Tab. 2-1 Physical properties of Zr[13]

	Unit	Mean value	[11-20] direction	[0001] direction
Density	$Kg\ m^{-3}$	6.500		
Coefficient of heat expand	K^{-1}	6.7×10^{-6}	5.2×10^{-6}	10.4×10^{-6}
Young modulus	GPa		99	125
Lattice constant	nm		a = 0.323	c = 0.515
Heat conduction	$W\ m^{-1}\ K^{-1}$	22		
Specific heat	$J\ kg^{-1}\ K^{-1}$	276		
Thermal neutron seizing section	barn ($10^{-28}m^2$)	0.185		

2.1.2 Zirconium alloys used in nuclear reactor

Due to the low heat neutron absorption section, zirconium alloys are used as nuclear fuel cladding. Thus good corrosion resistance and mechanics properties are gained. To remain the property of low heat neutron absorption section, element composition with high heat neutron absorption section should be very low[14]. Now main zirconium alloys include Zr-Sn, Zr-Nb and Zr-Sn-Nb three systems

1. Zr-Sn system alloys [15,16]

The corrosion resistance of pure zirconium is good. But the impurity elements caused by the metallurgy process, N, C, Ti, Al, Si et al, weaken the corrosion resistance. Sn is the element stabilizing α and can form substitute solid solution in α and β phases. So it can counteract the deleterious action of N in zirconium. The initial zirconium alloy was Zr-Sn alloy, the composition is Zr-2.5Sn, called Zr-1 alloy. But the corrosion resistance of Zr-1 alloy is too bad to be used. Later Zr-2 alloy was developed. Ni is main element causing to the high hydrogen weight gain of Zr-2 alloy. So Ni was removed from Zr-2 alloy and Fe was

increased to get Zr-4 alloy. Zr-2 and Zr-4 alloys have been used commercially. Zr-2 is used to the cladding material in BWR, and Zr-4 is used in PWR. They belong to Zr-Sn system, called the first zirconium cladding material.

With the improvement of metallurgy technique, N can be controlled at lower level. Because it is not good for the improvement of corrosion resistance to increase Sn content, Zr-4 composition is optimized: adjusting Sn content to lower limit (1.2 ～ 1.5 Sn), Fe and Cr contents to upper limits (Fe ～ 0.24, Cr ～ 0.13). This is improved Zr-4 alloy. Its corrosion resistance is better than the normal Zr-4 alloy and has been used widely. This is called the second cladding material.

2. Zr-Nb sytem alloys

When American and some west counties tried to develop Zr-Sn system alloys, Soviet Russia developed another series of alloys, Zr-Nb alloys. The merits of Nb are low thermal neutron absorption section. Nb can eliminate the harm of C, Al, Ti et al to corrosion resistance and reduce the hydrogen pickup. At present, E110 alloys of Russian, M5 of France, Zr-2.5Nb alloys are commercially used [19-21]. Zr-2.5Nb is specially used in CANDU pile. Zr-2.5Nb-0.5Cu alloy is exploited to gain higher strength material [14,22].

The corrosion resistance of Zr-Nb alloys is sensitive to the processing and heat treatment. Small and well-distributed β-Nb precipitates are good, however the β-Zr is not good [25].

3. Zr-Sn-Nb system alloys

Zr-Sn-Nb system alloys integrates the merits of Zr-Sn alloys and Zr-Nb alloys to meet the need of high fuel consume. ZIRLO alloys of American, E635 alloys of Russian, NDA alloys of Japan, HANA alloys of Korea , NZ2 and NZ8 alloys of China [26-47], the in-pile corrosion resistance of above alloys is better than that of Zr-4. At present, NZ2 alloys in China have been used in in-pile testing.

The development of nuclear energy is gradually promoting the research work of zirconium. Tab. 2-2 shows some main alloys used and studied.

Tab. 2-2 Main zirconium alloys in nuclear industry

Name	Composition	Country	Remark
Zr-2	Zr-1.5Sn-0.2Fe-0.1Cr-0.05Ni	American	Using
Zr-4	Zr-1.5Sn-0.2Fe-0.1Cr	American	Using
Zr-2.5Nb	Zr-2.5Nb	Canada	Using
Zr-1Nb	Zr-1Nb	Soviet Union	Using
ZIRLO	Zr-1.0Sn-1.0Nb-0.1Fe	American	Using
M5	Zr-1.0Nb-0.16O	France	Using
E635	Zr-1.2Sn-1.0Nb-0.4Fe	Russia	Using
NDA	Zr-1.0Sn-1.0Nb-0.4Fe	Japan	Studying
NZ2	Zr-1.0Sn-0.1Nb-0.28Fe-0.16Cr-0.01Ni	China	Studying
NZ8	Zr-1.0Sn-1.0Nb-0.3Fe	China	Studying
HANA6	Zr-1.1Nb-0.05Cu	Korea	Studying
HANA3	Zr-1.5Nb-0.4Sn-0.1Fe-0.1Cu	Korea	Studying
HANA4	Zr-1.5Nb-0.4Sn-0.2Fe-0.1Cr	Korea	Studying

2.2 Research summary of the waterside corrosion of zirconium alloys

2.2.1 Water chemical effect on corrosion behaviour

Now more than 90% commercial nuclear power plants are light water reactor plants, others are heavy water plants. Because zirconium alloys have good corrosion resistance, mechanics property and high heat exchange property, the fuel component cladding or the pressure tube material is made of zirconium alloys [14]. When the nuclear plant of light water pile runs, the internal side of zirconium alloy cladding contacts with the fission products at 400^{o}C, and the external surface contacts with high temperature and high pressure water (280～350^{o}C, 10～16 MPa). Generally H_3BO_3 and LiOH are added to cooling water to adjust the pH value.

The corrosion resistance of zirconium alloys are an important index deciding its using properties in nuclear power plant. During the study on the corrosion behaviour, the out-pile autoclave experiments are carried out to simulate the in-pile situation. For the same alloy, the transition time and the post-transition corrosion rate in different mediums are different. And the sensitivity of the same alloy to different water chemical conditions are different [48].

2.2.2 Alloys composition effect on corrosion behaviour

To get the zirconium alloys with better corrosion resistance, many researches about the alloying element effect on the corrosion resistance have been done [15,38,43,49-59]. The alloying element effects are very complicated, associating to the kind of alloying element, ratio and water chemical condition. In general, low Sn content, high Fe content, the additions of a little Nb and Cu, can improve the corrosion resistance of zirconium alloys. However, Mo is harm and the function of V is not clear. For Zr-Sn alloys, Nb content should not be too high, and a little Cu addition can further improve the corrosion resistance; For Zr-Sn-Nb alloys, decreasing Sn and Nb contents can further improve the corrosion resistance.

To implode the zirconium with high properties, it is necessary to establish a clear relation between alloying element and corrosion resistance, understand really the alloying element effect on the corrosion resistance.

2.2.3 Heat treatment effect on the microstructure and corrosion behaviour of the alloys

Alloying composition and heat treatment decide the microstructure of the alloy, moreover the microstructure decides the corrosion resistance and the mechanics property. In the case of certain alloying composition, appropriate heat treatment can further improve the corrosion resistance.

In Zr-2 and Zr-4 alloys, the solid solutions of alloying elements Sn, Fe, Cr, Ni are high in β-Zr, however those are low in α-Zr [23]. Most alloying elements exist in the precipitates. The heat treatment in α phase region after β quenching can affect the precipitate size and distribution. So Steinberg [60] introduced the accumulative annealing parameter A, and studied the relation between A value and corrosion resistance of Zr-2, Zr-4 alloys [53,61-66]. The results shown that $2\times10^{-18}h \leq A \leq 5\times10^{-17}h$ was good for even corrosion resistance and $A \leq 10^{-18}h$ was good for nodular corrosion resistance.

Garzarolli and Foster [62,65,67] thought that the precipitate size, amount and distribution were changed by the A value change. When the size of precipitate was small (～50 nm), the corrosion resistances of Zr-2 and Zr-4 in 420^{o}C steam and 360^{o}C water were bad, but the nodular corrosion resistances in 500 ^{o}C steam were good. That's contrary when the size of precipitate was more than 200 nm. So they thought that the effect of heat treatment on the corrosion resistance was related to the precipitate size and amount changed by the heat treatment.

Zhou [68,69] found that there was no the above corresponding relation between the heat treatment and corrosion resistance. They thought that the alloying element content change in the matrix caused by the heat treatment was main reason of corrosion resistance change.

It's obvious that there is no consistent understand in the effect reason of heat treatment on corrosion resistance of Zr-2 and Zr-4 alloys. This should be studied further.

The microstructure of zirconium alloys containing Nb is more complicated than that of Zr-4 alloys. The accumulative annealing parameter A is not applicable to zirconium alloys containing Nb[70].

Many studies approved [25,71-78] that the corrosion resistance of zirconium alloys with low Nb (< 0.6%) was not sensitive to heat treatment, however that of zirconium alloys with high Nb (> 0.6%) was sensitive. β-Zr and supersaturated Nb in the matrix are harm to the corrosion resistance. The corrosion resistance of zirconium alloys containing Nb is related to the changes of the supersaturated Nb content and precipitates during heat treatment. The mechanism of heat treatment effect on corrosion resistance of zirconium alloys containing Nb is not understood clearly.

2.3 The oxidation of zirconium alloys

The growth kinetics of oxide is obtained by the weight gain kinetics. This supposes that the oxide is remained on the sample and the oxide is even. The oxide thickness is obtained by the conversion of ZrO_2 density. 1μm thickness oxide is equal to 15 mg/dm^2 weight gain. Corrosion kinetics of different zirconium alloys can be compared by this method.

2.3.1 The oxidation kinetics of even corrosion of zirconium alloys

The weight gain kinetics of zirconium alloys is divided to two stages: pre-transition and post-transition [12,84,85]. The pre-transition characteristic is low weight gain rate, similar to cubic curve, not parabola curve expected by Wagner-Hauffe theory. Because the oxide growth controlled by diffusion happens at the crystal boundary, not in the even solid [86-88].

Many studied about the stress, texture and crystal structure of oxide film have been done [89-93]. At the beginning of corrosion, the oxide formed on the surface of metal is t-ZrO_2.

The corrosion transition happens when the oxide film thickness reaches 2～3 μm, and the corrosion rate is similar linear [12,84,85]. The linear rate increases with the thickness increasing [94]. The transition process is a mark of the formation of holes in the oxide film [83-97].

The corrosion kinetics of Zr-Sn alloys and Zr-Nb alloys are different. There is no clear rate transition in the kinetics of Zr-Nb alloys, and the change from cubic to linear is not observed [98-100].

2.3.2 The oxidation process

First the zirconium alloys with fresh surface will take an oxidation reaction: $Zr+2H_2O \rightarrow ZrO_2+2H_2$. The beginning reaction is slow and a thin, protective oxide film is formed, which further prevents the oxidation. The dense oxide consists of t-ZrO_2, which stable at high temperature. Subsequently O^{2-} in the oxide film dissolves to metal to form anion vacancies. O^{2-} diffuses from the oxide film surface and passes the oxide by vacancy mechanism to react with Zr. While the oxide growing, stresses are produced by the volume expander. The compressive stresses can't be counteracted by the tensile stresses in the metal, thus the martensite phase transformation happens and the m-ZrO_2 is formed, the film becomes loose. During the process, many small holes and cracks are formed and the corrosion is accelerated [101-103].

2.3.3 The growth theory of oxide film

Wagner theory thought that O^{2-} diffuse along the anion vacancies of oxide film and passes the oxide film to metal surface, moreover the electrons moves from the metal surface to outside, thus the oxide film grows at the metal/oxide interface. Their balance rate or the substitute rate of O^{2-} and the vacancies in the oxide film decides the corrosion rate [103]. Another theory supports O^{2-} diffusing through the crystal boundaries [105,106].

2.3.4 Corrosion mechanism

The oxide structure change leads to many cracks and holes, thus the oxide film becomes loose and loses protect. The corrosion rate increases, even the oxide film scales off [102].

There are many corrosion mechanism of zirconium alloys in LiOH water[102,107].

1. Diffusion hypothesis

After Li^+ enters the oxide film, the concentration of anion vacancy increases, which accelerates the vacancy diffusion and corrosion. There is another hypothesis, namely the re-crystallisation process is changed by Li^+ in-break, which thins the crystal and increases crystal boundaries. The short circuit diffuse channels of the anion vacancies are increased and the vacancy diffusion is accelerated [102,108].

2. Dissolving hypothesis of Cox [109]

Because c-ZrO_2 or t-ZrO_2 is preferential dissolved in LiOH to m- t-ZrO_2, thus big holes appear. These holes accelerate the corrosion rate.

3. OLi group cumbering hypothesis

Ramasubramanian [110] thought a majority of Li were absorbed in the holes of the oxide film, and the undecomposed LiOH would react with the anion vacancies on the surface of oxide film to form OLi group. The OLi moved to ZrO_2 crystal boundary to prevent the crystal growth and thin the crystal, increase the diffuse passages of anions.

4. Barrier hypothesis

Pecheur [111] proposed that there was a dense barrier at the metal/oxide interface. The thickness of this barrier increases gradually at the corrosion pre-transition until about 1μm, and the thickness decreases to 0.1μm after the transition happens. So he thought the addition of LiOH could destroy the barrier to accelerate the corrosion.

5. Phase transformation hypothesis [112]

LiOH can decrease the compressive stresses in the oxide film and lead to the transformation from t-ZrO_2 to m-ZrO_2, even the t-ZrO_2 is not formed.

2.3.5 The crystal structure of oxide film [102,113]

In inner oxide film, t-ZrO_2, c-ZrO_2, m-ZrO_2 exist. In the middle layer of oxide, vacancies et al diffuse and agglomerate and the internal stresses in the oxide film release. Sub-stable phases transform to stable m-ZrO_2 and small holes form at the crystal boundary. The holes develop to cracks. On the oxide surface, the holes are big, so the oxide on surface is m-ZrO_2 [113].

2.3.6 Oxidation of the precipitates [102]

The precipitates are incorporated into the oxide film and oxidized at a certain distance from interface. During the oxidation, the metal atoms in the precipitates will release to the metal matrix. Fe is oxidized when t-ZrO_2 transforms to m-ZrO_2. Some precipitates become non-crystalline in the oxide film. And the precipitates have a function of short circuit, this could be the starting position of nodular corrosion.

2.4 Research summary of out-pile corrosion of zirconium alloys

Now, the studies about the relationships of processing techniques, microstructure characteristic and out-pile corrosion resistance, have been done widely. The processing techniques and microstructure characteristics belong to metallurgy factors. Although the corrosion mechanism has been studied for more than half one century, there is no clear understanding for the corrosion mechanisms of mature alloys (Zr-2, Zr-4, Zr-1Nb et al). So the studies for the corrosion mechanism of the third zirconium alloy should be done deeply.

Chapter 3

Research methods

Chapter 3 : Research methods

NZ2 and NZ8 alloys, submitted to a certain heat treatment, are chosen to study the corrosion behaviours in different mediums. The effects of Nb addition and oxide microstructure on the corrosion resistance are understood by studying the corrosion weight gain, microstructure change of matrix, crystal structure of oxide film, phase content and stress in the oxide film.

3.1 The materials used in the experiments

The experimental samples are 1mm plates from NIN. The element compositions of two alloys and Zr-4 alloy (used to compare) are shown in Tab. 3-1. Zr-4 alloy belongs to Zr-Sn system and is used widely now. NZ2 and NZ8 belong to Zr-Sn-Nb system and is in the stage of studying and exploitation.

The plates are gained by following techniques flow:

Three vacuum melting-β forging-β quenching-α hot rolling (<600^{o}C)-three intermediate annealing and the 30-50% cold process after every annealing-plates (δ=1mm) and final recrystal annealing (580^{o}C/2h). The intermediate annealing parameters are shown in Tab. 3-2.

Tab. 3-1 The element compositions of two alloys (wt.%)

Alloys	Sn	Nb	Fe	Cr	O	Zr
Zr-4	1.5	-	0.2	0.1		Balance
NZ2	1.0	0.3	0.3	0.1	0.08-0.14	Balance
NZ8	1.0	1.0	0.3	-	0.08-0.14	Balance

Tab. 3-2 The intermediate annealing parameters

First time annealing	Second time annealing	Third time annealing
650ºC/2h	590ºC/2h	590ºC/3h

3.2 The autoclave experiment

The corrosion resistance of zirconium alloys to high temperature water is an important property of nuclear fuel cladding. The out-pile autoclave corrosion experiment, simulating nuclear reactor pile conditions, is a usual method of studying the corrosion behaviours. The samples are corrosion tested simultaneously in single autoclaves with test being periodically interrupted to measure specimen weight gain. Corrosion weight gain is the average value of four samples. Corrosion kinetics is determined by measuring the weight gain as a function of exposure time.

3.2.1 Corrosion conditions

Long-term corrosion testing of plates specimens (15mm×25mm×1mm) was performed in static autoclaves at 360^{o}C/18.6MPa pure water, 360^{o}C/18.6MPa lithiated water and 400 ^{o}C/10.3MPa steam. Then the samples corroded for different time were tested.

3.2.2 The instruments used in the autoclave corrosion testing

1. Autoclave: A special autoclave, cubage is 2L, compression resistance is 30MPa, and pressure meter, drain tap and the slice preventing blast are equipped.

2. Instrument controlling temperature: controllable Si electric cooker instrument controlling temperature, the controlling precision is ±1^{o}C.

3. Weighing up: the high precision balance is used, the precision is 0.01mg.

4. Testing the sample size: vernier calliper is used, the precision is 0.2mm.

3.2.3 The method indicating the corrosion degree

In this study, multiple specimens are tested simultaneously in single autoclaves with test being periodically interrupted to measure specimen weight gain. Corrosion kinetics is determined by measuring the weight gain as a function of exposure time. The corrosion weight gain is indicated by the method of measuring the weight gain of unit area. The formula is w_t=1000•(W_t-W_0)/S, W_0 is the weight of sample uncorroded (mg), W_t is the weight of sample corroded (mg), S is the area of sample (mm^2), w_t is the weight gain (mg/dm^2).

3.2.4 Preparation of samples in the autoclave experiments

1. Cutting the samples to 25×15 mm pieces.

2. Doing marks on the samples and drilling φ1.5mm holes on the samples.

3. Dipping the samples in acetone and cleaning the smarminess of the sample surface with the absorbent cotton.

4. Putting the samples in the acid to clean, the cleaning temperature is 30～50^{o}; 10%HF+45%HNO_3+45%H_2O is used to clean zirconium alloys containing Nb, and 10%HF+30%HNO_3+30%H_2SO_4+45%H_2O is used to clean zirconium alloys not containing Nb.

5. Immediately putting the samples to flowing water for at least 15 min.

6. Putting the samples to boiling water to clean at least thrice.

7. Drying the samples.

8. Weighing in by the electronic balance, the precision is 0.01 mg.

9. Measuring the size by vernier calliper.

3.3 Analysis and measurement

3.3.1 The measurement of microstructure and precipitates of the alloy samples

JEM-200CX transmission electron microscope is used to test the microstructure and the precipitates. The processing of specimen preparation is as following: thinning the specimen to 70～80 μm by machine method, then preparing φ3 mm wafer with special tool and preparing thin specimens by electrolyse polishing. EDS is used to analyze the compositions of the precipitates.

3.3.2 The measurement of crystal structure and internal stresses in the oxide film

To study the corrosion mechanism of new zirconium alloys containing Nb, a large panel of normal methods were used in this study.

1. X-ray diffraction instrument

The phase structure of material could be confirmed by analyze the peak position and intensity of X-ray diffraction; The internal stresses in the oxide film could be confirmed by the peak shift of m-ZrO_2. The grazing XRD instrument of PW3830 (Fe, $\lambda_{K\alpha}$ = 1.93637 Å) was used to test the surface structure of oxide film. The normal XRD instrument of PW3830 (Cu, $\lambda_{K\alpha}$ = 1.544426 Å) was used to test the structure of the whole oxide film and internal stresses.

2. A JY-T64000 laser Raman spectrometer in the Institute of Physics, Chinese Academy of Sciences was used to test the crystal structure of different thickness of oxide film in order to confirm the phase transformation during corrosion.

3. Neutron diffraction instrument

D1B neutron diffraction instrument of ILL in France was used to test the category and structure of precipitate.

4. Scanning electron microscope

JSM-840A scanning electron microscope of CNRS in France was used to analyze the oxide film section.

3.4 Processing of datas

Photoshop software was used to deal with the photos, XRD and Raman datas were plots by Origin software, and the data about stress analysis was dealed with by Igor software.

Chapter 4

Corrosion resistance of zirconium alloys

Chapter 4 Corrosion resistance of zirconium alloys

4.1 Introduction

The waterside corrosion resistance of zirconium alloys is an important index determining if the material can be used as nuclear fuel cladding. In the investigation of the corrosion behaviour of zirconium alloys, the autoclave testing is used to out-pile simulation study. Several water chemical conditions are used in the out-pile autoclave corrosion test:

1. 350～370^{o}C/16～19 MPa pure water, used to understand the normal corrosion regularity.

2. 350～360^{o}C/16～19 MPa LiOH or LiOH+H_3BO_3 aqueous solution, used to simulate the in-pile water chemical conditions and understand the effect of LiOH or H_3BO_3 on the corrosion behaviours of zirconium alloys.

3. 400～420^{o}C/10.3 MPa steam, used to study the even corrosion behaviours of zirconium alloys.

4. 500^{o}C/10.3 MPa steam, used to study the study the nodular corrosion behaviours of zirconium alloys.

When zirconium alloys are corroded in the high temperature water and overheating steam, the corrosion weight increasing in divided to two stages[114]: Pre-transition and post transition stages. The pre-transition corrosion characteristic is mainly the low weight increasing rate, namely the oxide film is thin. The kinetics curve of Zr-Sn alloys is close to cube, not parabola kinetics expected by the Wagner-Hauffe theory, and the kinetics curve of Zr-Nb alloys is cube or close to parabola. When the oxide film reaches to a certain thickness, the corrosion kinetic takes a linear variation (or close to linear relation) [115-128]. As the oxide film thickness reaches to 2～3 μm and the corrosion weight increasing reaches to 30～50mg/dm^2, the corrosion transition happens. Some researchers found that the post-transition kinetics curve of zirconium alloys is not simple linear relation [129-131]. So the weight curve is divided: similar parabola curve, namely pre-transition stage, gradual change stage and linear stage (Fig. 4-1) [118].

With the corrosion medium change, there are 3 kinds of kinetics transition models [132]. The first is the circle gradual change: in 300 ~ 360^{o}C water, the transition is sudden, the post-transition corrosion rate increases rapidly and then the pre-transition corrosion discipline is repeated. In this study the corrosion processes of NZ2 alloys in 360^{o}C pure water and LiOH water show the same discipline. The second is uni-directional gradual change: in higher temperature Oxygen or steam, there is no sudden kinetics transition (from cube to linear). The third is super-linear transition: the transition is from similar cube to square and then to linear. The corrosion rate does not increase during the total corrosion. In this study the corrosion processes of new zirconium alloys in 400^{o}C steam show the same discipline.

It is generally considered that the kinetics transition indicates the hole formation in the dense oxide film [114]. The transition time is different in the different composition alloys and different corrosion medium.

It is necessary to improve the corrosion resistance of zirconium alloys to meet the needs of higher using properties. The corrosion behaviours of zirconium alloys in different mediums are studied in this chapter.

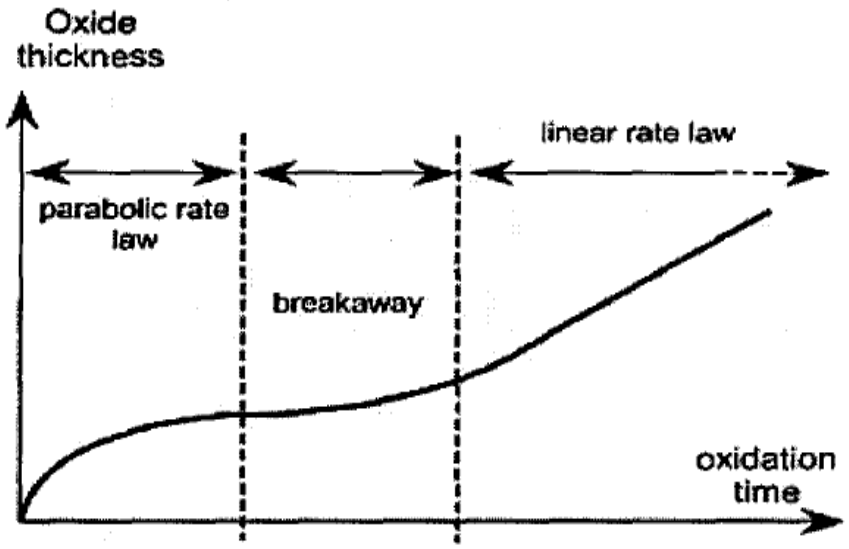

Fig.4-1 Oxidation kinetics in autoclave test for zirconium alloys

4.2 Corrosion resistance of zirconium alloys in LiOH water

The corrosion kinetics curves of NZ2, NZ8, improved Zr-4 alloys in 360^{o}C/18.6 MPa LiOH water are shown in Fig. 4-2. Zr-4 alloy samples are sensitive to the corrosion in 360^{o}C/18.6 MPa LiOH water. After the transition happens, the oxide film loses the protection and the reaction controls the corrosion process. However the corrosion resistances of NZ2 and NZ8 alloys are much better than that of Zr-4. When the new zirconium alloys are corroded for about 200 days, the weight increase is less 10% than that of Zr-4 alloys. At the beginning of corrosion, the corrosion resistances of NZ2 alloys and NZ8 alloys are similar, and the transition happens at 126 days and 98 days respectively. The corresponding oxide thicknesses at the transition points are both 2~3 μm. The post-transition corrosion rate of NZ8 alloys is higher than that of NZ2 alloys. When the alloys are corroded for more than 300 days, the weight increasing of NZ2 alloys is about 80% that of NZ8 alloys. The corrosion resistance of NZ2 alloys is the best, because of the Nb addition compared to Zr-4; Fe and Sn contents in NZ2 alloys are the same to those in NZ8 alloys, but Cr exists in NZ2 alloys and the Nb content in NZ2 alloys is lower that in NZ8. The precipitates in NZ2 alloys are cubic $Zr(Fe,Cr)_2$ and $Zr(Fe,Cr,Nb)_2$, and the precipitates in NZ8 alloys are β-Zr containing Nb. So it's concluded that Nb addition can improve the corrosion resistance of zirconium alloys in 360^{o}C LiOH water.

4.3 Corrosion resistance of zirconium alloys in 400^{o}C steam

The corrosion kinetics curves of NZ2 and NZ8 alloys in 400^{o}C/10.3 MPa steam are shown in Fig. 4-3. The pre-transition corrosion rates of both alloys are the same, and the transition time of NZ2 alloys is 42 days, that of NZ8 alloys is 70 days. The corresponding oxide thicknesses are 2~3 μm. The post-transition corrosion rate of NZ8 alloys is much higher than that of NZ2 alloys. Investigating the kinetics curve differences of zirconium alloys, we can find that the composition play an important role to improve the corrosion resistance of zirconium in 400^{o}C/10.3 MPa steam. The large quantities of β-Zr precipitates and the supersaturated Nb content in the NZ8 matrix could be the main reason of high post-transition corrosion rate, which will be discussed in next chapter. The low Nb content in NZ2 is the main reason of its good corrosion resistance. Comparing the compositions and corrosion resistances of these alloys, it's difficult to conclude the alloying element effect regulation on

corrosion resistances of zirconium alloys in 400°C/10.3 MPa steam, but it's indicated that too high Nb content is not good to improve corrosion resistance. In addition, the corrosion transition time of NZ2 alloys is shorter than that of NZ8 alloys. The small precipitates in NZ2 alloys are oxidized rapidly, which shortens the pre-transition time. The oxidation of bigger precipitates in NZ8 alloys needs longer time. Thus the appropriate size of precipitate is good to improve the corrosion resistance.

4.4 Corrosion kinetics of zirconium alloys with low Nb content in different media

The corrosion kinetics curves of NZ2 alloys in 360°C/18.6MPa pure water, 360°C/18.6 MPa lithiated water, 400°C/10.3 MPa steam are shown in Fig. 4-4. The corrosion rate of NZ2 alloys increases in the sequence of 360°C/18.6 MPa pure water, 360°C/18.6 MPa lithiated water and 400°C/10.3 MPa steam, and the transition time is 182 days, 126 days and 42 days respectively. It's indicated that the corrosion medium plays an important role to corrosion behaviour of zirconium.

4.5 Summary

The corrosion resistance of new zirconium alloys containing Nb in 360°C lithiated water is much higher than that of Zr-4 alloys, that is to say, Nb addition is good to improve the corrosion resistance of zirconium alloys. Whatever in 360°C lithiated water or in 400°C steam, the corrosion resistance of NZ8 alloys containing high Nb is less than that of NZ2 alloys with low Nb content, which is related to the precipitate particles and alloying element content in matrix. And the oxide thickness at transition point is 2~3 μm. In addition, small, well-distributed precipitates shorten the transition time of NZ2 alloys in 400°C steam, but improve the post-transition corrosion resistance of zirconium alloys. In the different mediums, the corrosion kinetics of one alloy is different.

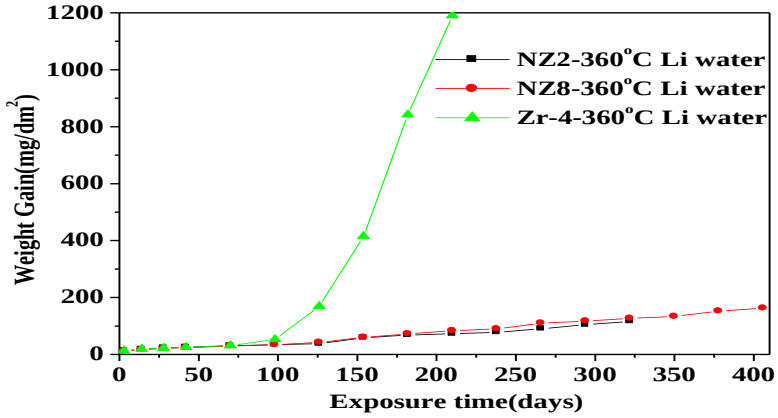

Fig.4-2 Corrosion kinetics of NZ2, NZ8 and Zr-4 alloys investigated in 360°C lithiated water

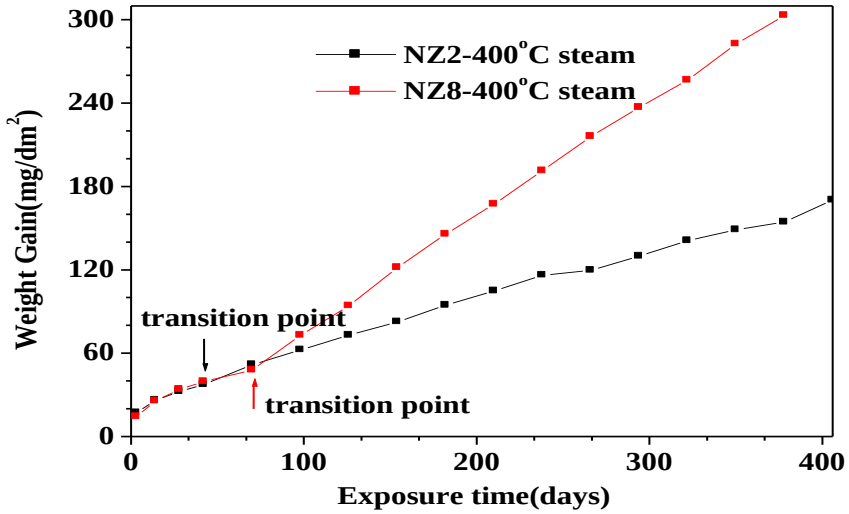

Fig.4-3 Corrosion kinetics of NZ2 and NZ8 alloys investigated in 400°C steam

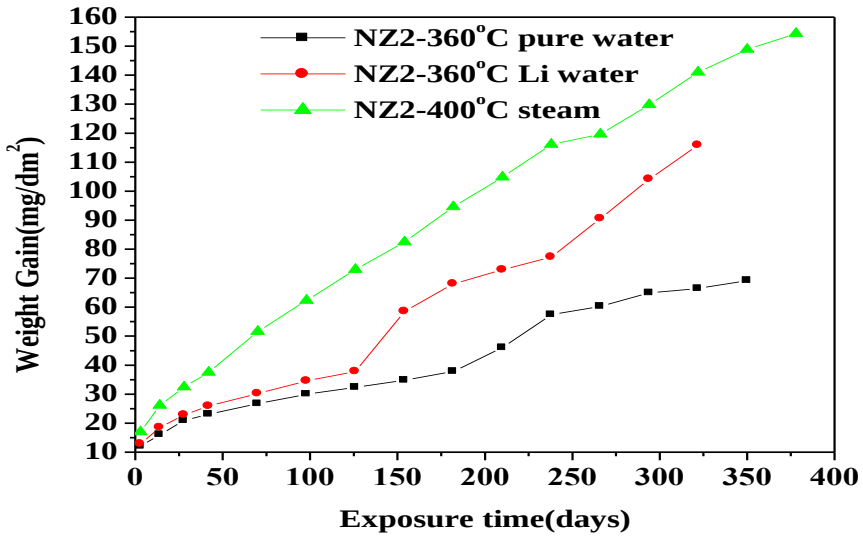

Fig.4-4 Corrosion kinetics of NZ2 alloys investigated in different media

Chapter 5

Relationships between the matrix microstructure and the corrosion resistance of new zirconium alloys

Chapter 5 Relationships between the matrix microstructure and the corrosion resistance of new zirconium alloys

5.1 The matrix microstructure of zirconium alloys

TEM images of NZ2 alloys matrix is shown in Fig. 5-1(a), (b). The precipitates are well-distributed and the amount of the precipitates is small, the average size is about 50 nm. The EDS analysis shows that there are two kinds of precipitates, cubic $Zr(Fe,Cr)_2$ and $Zr(Fe,Cr,Nb)_2$ (Fig. 5-1(c), (d)). Because of the low Nb content in NZ2 alloys and the formation of the precipitates containing Nb, the Nb content in NZ2 matrix is lower than the solubility. Fig. 5-2 shows the microstructure of NZ8 alloys, the amount of the precipitates is much more than that in NZ2 alloys and the average size of the precipitates is bigger, about 100 nm. The EDS analysis shows that there is one kind of β-Zr precipitate containing Nb in NZ8 alloys. Because the Nb content in NZ8 alloys is high, however the Nb content in the precipitates is low, the Nb content in NZ8 matrix is higher than the solubility. Sn is not observed in the precipitates of both alloys, so Sn exists in matrix.

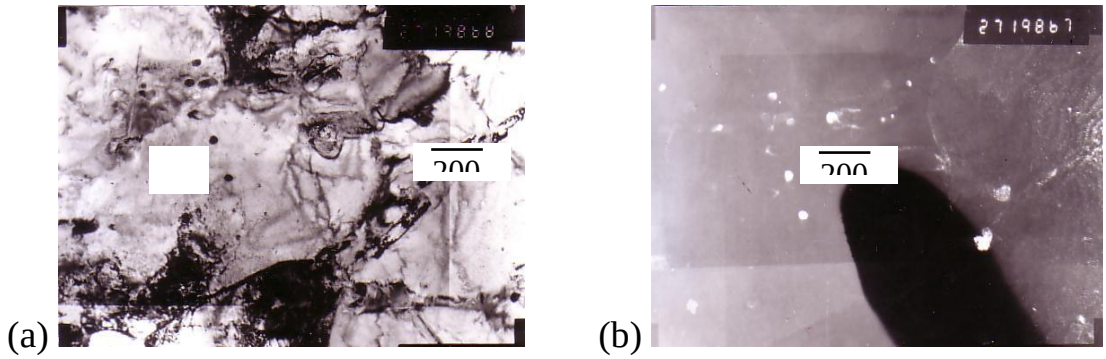

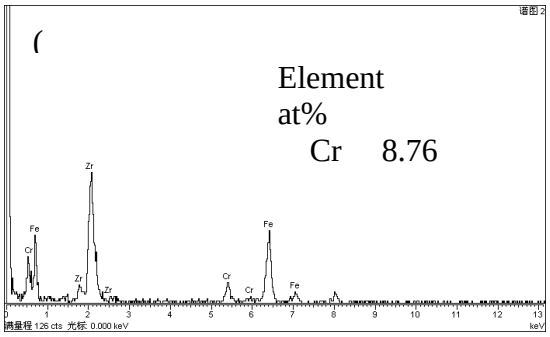

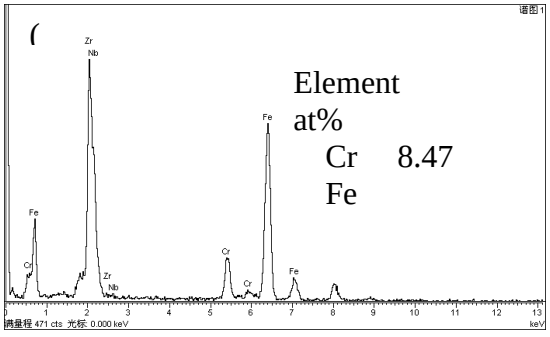

Fig.5-1 TEM images of NZ2 alloys matrix and the EDS result of the precipitates（b） dark image (c) and (d) microanalyses

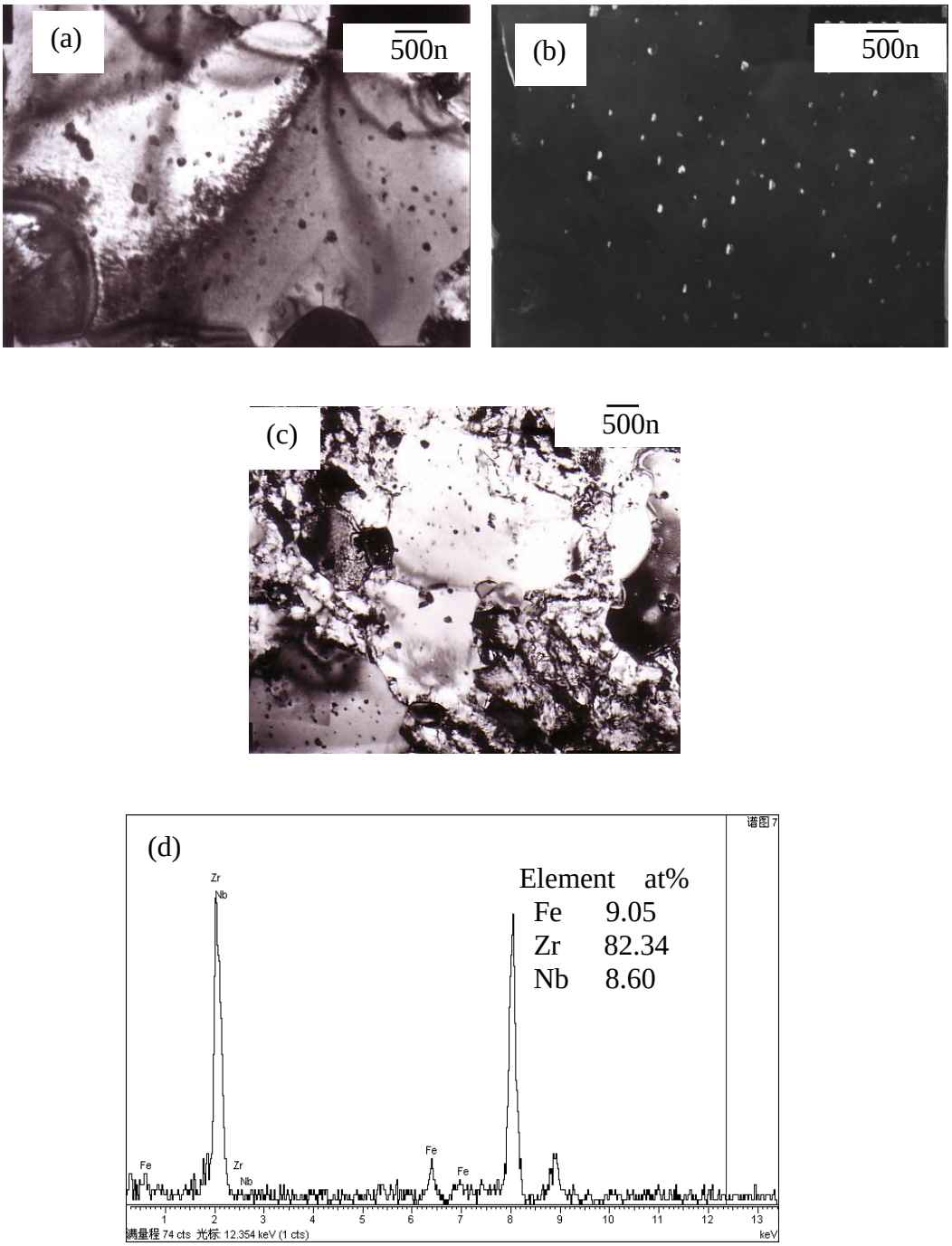

Fig.5-2 TEM images of NZ8 alloys matrix and the EDS result of the precipitates (b) dark image corresponding to (a)

Fig. 5-3 and 5-4 show the neutron diffraction patterns of both alloys. It is observed that there is the C14 type $Zr(Fe,Cr)_2$ precipitates in NZ2 alloys, but there is no this precipitate in NZ8 alloys. This is consistent with the TEM results.

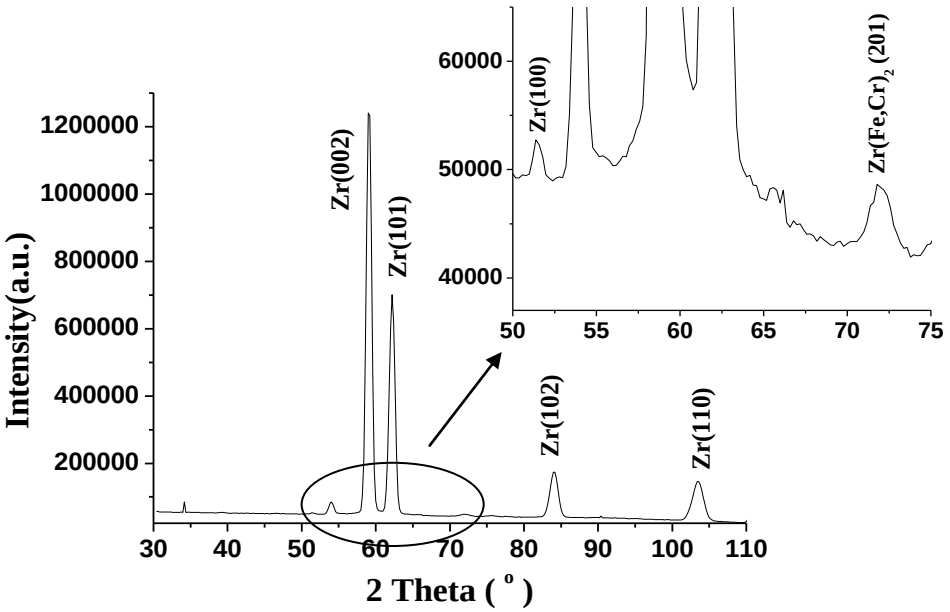

Fig.5-3 Neutron diffraction pattern of NZ2 alloys matrix

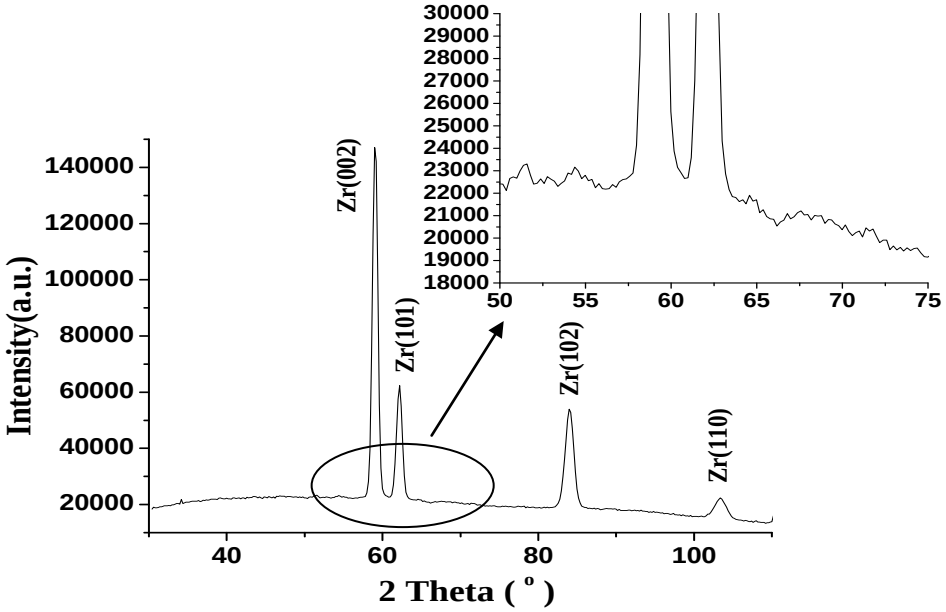

Fig.5-4 Neutron diffraction pattern of NZ8 alloy matrix

5.2 Matrix microstructure effect on the corrosion resistance of zirconium alloys

It is well known that the corrosion resistance of zirconium alloys is closely related with the alloying element content in matrix and the precipitate characteristics. The oxidation rate of precipitates is faster than that of matrix. So the precipitates are incorporated into the oxide layer and then undergo a chemical change starting at a particular distance from the metal/oxide interface [133]. The crystal structure of oxide film is affected by the delay oxidation of the precipitates.

In this study, the corrosion resistance of NZ2 alloys is better than that of NZ8 alloys whatever in 360°C lithiated water or 400°C steam. In NZ2 alloys, Fe and Cr atoms exist

mostly in the precipitates, but Sn completely dissolves in the matrix, Nb exists in the matrix and the precipitates. In NZ8 alloys, Sn completely dissolves in the matrix, a little Nb exists in β-Zr precipitates and a great deal of Nb supersaturates in the matrix. During the oxidation, the matrix of zirconium alloys is oxidized first and then the precipitates incorporated in the oxide film are oxidized.

During the oxidation of the matrix, a great deal of Sn and Nb atoms dissolved in the matrix are redistributed [135]. In the autoclave the stabilized oxides of Sn and Nb are SnO and Nb_2O_5. The oxide of Nb needs more oxygen, which means that the volume fraction of SnO is lower than that of Nb_2O_5 when the same content Sn and Nb are oxidized. The Nb and Sn atoms are distributed at the crystal boundary, and when the oxygen pressure is high enough, Nb and Sn will be oxidized. The delayed oxidation of alloying elements accelerate the formation of cracks in the oxide film, thus the corrosion rate increases because of the increasing of diffusing passes of the oxygen. This effect is very obvious in NZ8 alloys containing high Nb, however it's weak in NZ2 alloys. Because Nb content in NZ2 matrix is less than the solid solution limit and a great deal of Nb atoms exist in the precipitates. However, in NZ8 alloys, the oxidation of supersaturated Nb in the matrix causes to great volume expander, which promotes the stress accumulation in the oxide film and the transformation from t-ZrO_2 to m-ZrO_2. That is to say, the supersaturated Nb in NZ8 matrix deteriorate the corrosion resistance. In addition, the oxidations of Zr matrix and alloying elements dissolved produce the compressive stresses in the oxide film. The alloying element effect on corrosion resistance is a balance process of the compressive stress production and the crack formation caused by the stress accumulation.

Later the incorporated precipitates are oxidized, the precipitate is another important factor affecting the corrosion resistance of zirconium alloys. The oxidation rates of alloying elements in the precipitates are digressive in the sequence of Fe, Cr, Nb [136,137]. In the initial stage of the precipitate oxidation, Fe and Cr diffuse to the oxide film one after the other and are oxidized gradually, which enhances the compressive stresses in the oxide film. When the stress exceeds a certain value, t-ZrO_2 transforms to m-ZrO_2. With the oxide processing, Nb in the precipitates diffuses to the around oxide films and is oxidized. If the oxygen pressure is not high enough, Nb will be oxidized to NbO or Nb_2O_3 first, which increases the vacancy concentration. When the vacancy concentration is high enough to form the vacancy cluster along a certain direction, t-ZrO_2 will first change into c- ZrO_2 to minimize the system energy [138]. In fact, the stablest oxide of Nb is Nb_2O_5, so NbO or Nb_2O_3 will transform to Nb_2O_5, which reduces the vacancies in the oxide film. C-ZrO_2 transforms to m-ZrO_2. At the same time, the formation of Nb_2O_5 makes the local volume expand more, which promotes the produce of cracks and leads to corrosion acceleration [139]. The oxidation rate of β-Zr precipitates in NZ8 alloys is faster than that of $Zr(Fe,Cr)_2$ and $Zr(Fe,Cr,Nb)_2$ precipitates in NZ2 alloys, and the oxidation of β-Zr precipitates accelerates the transformation from t-ZrO_2 to m-ZrO_2[140], thus accelerates the corrosion rate of NZ8 alloys.

The volume fraction of the precipitates is another important factor affecting the corrosion resistance[141]. After the great deal of precipitates in NZ8 alloys are oxidized, the additional stresses are produced in the oxide film, which increases the internal volume expander attending by the formation of cracks, thereby the corrosion rate is accelerated. So considering whatever the precipitate category, volume fraction or Nb content in the matrix, we can explain the reason of higher corrosion rate of NZ8 alloys.

In addition, the precipitates of NZ2 alloys are small. These small precipitates shorten the pre-transition time of corrosion. However, the oxidation of big precipitates of NZ8 alloys needs longer time, therefore the pre-transition time is longer.

5.3 Summary of the chapter

The corrosion resistance of new zirconium alloys is closely related with the Nb content in the matrix and the supersaturation degree. The oxidation of supersaturated Nb in NZ8 alloys makes the oxide volume expand seriously, even makes the oxide film break, which promotes the transformation from t-ZrO_2 to m-ZrO_2. The Nb content in NZ2 matrix is lower than the equilibrium solution limit. So the post-transition corrosion rate of NZ8 alloys is much higher than that of NZ2 alloys. At the same time, the corrosion resistance of zirconium alloys is closely related with the precipitate category and oxidation characteristic. The oxidation rate of β-Zr precipitates in NZ8 alloys is faster than that of $Zr(Fe,Cr)_2$ and $Zr(Fe,Cr,Nb)_2$ precipitates in NZ2 alloys, and the oxidation of β-Zr precipitates accelerates the transformation from t-ZrO_2 to m-ZrO_2, thus accelerates the corrosion rate of NZ8 alloys. In addition, the volume fraction of the precipitates is another important factor affecting the corrosion resistance. After the great deal of precipitates in NZ8 alloys are oxidized, the additional stresses are produced in the oxide film, which increases the local volume expander attending by the crack formation, thereby the corrosion rate is accelerated. So considering whatever the precipitate category, volume fraction or Nb content in the matrix, we can explain the reason of higher corrosion rate of NZ8 alloys. The small precipitates in NZ2 alloys shorten the pre-transition time of corrosion in 400^{o}C steam.

Chapter 6

The oxide film crystal structure effects on the corrosion resistance

Chapter 6 The oxide film crystal structure effects on the corrosion resistance

6.1 Introduction

When zirconium alloys are corroded in high temperature and pressure water (or steam-gas), the oxide film form gradually at the oxide/metal interface[142]. The O^{2-} has to pass the oxide film to reach the oxide/metal interface. So the oxide film microstructure and the evolvement process during the corrosion will directly affect corrosion resistance. In addition, because the ratio given by Pilling and Bedworth is 1.56 for the zirconia/zirconium system, the oxide films are going to create a high level of stress due to the difference in volume between the oxide and the metal when the zirconium alloys are oxidized. This will give compressive stresses in the oxide and tensile stresses in the underlying metal. There are many defects in the oxide films under the high compressive stresses. These defects make the stresses relax partially. However the defects in the oxide gradually evolve under the stresses and temperature. This is an important reason of the evolvement of the oxide microstructure during the corrosion [143]. Another important factor affecting the oxide microstructure evolvement is the precipitates. Generally, the oxidation rate of the precipitates is slower that of the matrix. When the matrix oxidation occurs, the precipitates are not oxidized at the same time as the surrounding metal. They are incorporated in the oxide and are going to be progressively oxidized. This will have an effect on the local stress distribution in the oxide films. So this is a point worth to research. In this chapter the oxide film microstructure of NZ2 and NZ8 alloys, corroded in 360^{o}C lithiated and 400^{o}C steam, is studied to provide good information to corrosion mechanism study.

6.2 The crystal structure of NZ2 alloy oxide films

Fig. 6-1 and 6-2 show grazing incidence XRD patterns of oxide film surface for NZ2 alloy exposed to 360°C lithiated water and 400°C steam during 3 days, respectively. According to Fig, 6-3, the thicknesses measured, correspondingly to 0.2°, 0.3°, 0.5° and 1.0°, are 0.02 nm, 0.03 nm, 43.18 nm and 143.48 nm respectively. It's clear that the intensity of T(101) Bragg peak for t-ZrO_2 increases from the outside to the inside of oxide film. Besides, the t-ZrO_2 content in the oxide layer was found larger when processed in litiated water at 360°C than in steam at 400°C, for a common duration of 3 days. Fig. 6-4 shows the grazing incidence XRD patterns of oxide film surface of NZ2 alloy exposed to 360°C lithiated water for 3 days (curve A), 42 days(curve B) and 182 days (curve C) respectively. The grazing incidence angle is 1.0° and the probed thickness of oxide film is 143.48 nm. In curve A corresponding to the 3 days exposure, the intensity of the T(101) Bragg peak for t-ZrO_2 is higher than that of M(111) one corresponding to m-ZrO_2 but it's contrary in curve B and C corresponding to 42 days and 182 days exposure. This means that the t-ZrO_2 content in the oxide layer decreases whereas the content of m-ZrO_2 increases versus the duration of corrosion process, i.e. the t-ZrO_2 transforms to m-ZrO_2. Fig. 6-5 shows the grazing incidence XRD pattern of oxide surface for NZ2 alloy exposed to 400°C steam for 3 days 42 days and 70 days. This result is consistent result with Fig. 6-4, namely, t-ZrO_2 transforms to m-ZrO_2 with the prolongation of corrosion time.

From the reported grazing incidence XRD analyses, the outside oxide layer of corroded NZ2 alloy was found to consist mostly of m-ZrO_2, including a small amount of t-ZrO_2. With the corrosion process, t-ZrO_2 transforms to m--ZrO_2. The higher t-ZrO_2 the content is, the better the corrosion resistance is.

Fig. 6-6 shows the normal XRD patterns of the oxide film of NZ2 alloy exposed to 360°C lithiated water for different times. It is worth to note that the intensity of M(002) Bragg peak increases and that of T(002) one decreases with the corrosion process. T-ZrO_2 changes to m-ZrO_2. This is consistent with the results of grazing incidence angle XRD. The total integrated intensities I(hkl) of the M(-111), M(111) and T(101) were used to determine the t-ZrO_2 volume fraction with respect to the total volume of zirconia using the Garvie-Nicholson formula[144]:

$$f_{\mathrm{T}} = \frac{I_{\mathrm{T}}(101)}{I_{\mathrm{T}}(101) + I_{\mathrm{M}}(111) + I_{\mathrm{M}}(-111)}$$

The result of calculation as shown in Fig. 6-8, validates the above conclusions. However, the formula is likely biased because of the strong texture in the oxide film. So a better determination of the relative proportion of the t-ZrO_2 and m-ZrO_2 phases needs additional experiment and analysis, e.g. texture determination. The present analysis is only a guide to appreciate the main impact of the corrosion time on the oxide layer transformation.

However, it is worth to note that in Fig. 6-6, trace 3 corresponding to (200) diffraction of c-ZrO_2 phase appears when the corrosion time reaches 98 days and the oxide film thickness is 2.3μm. Then the intensity of the (200) Bragg peak increases obviously with the corrosion time (traces 4, 5, 6, 7), which corresponds to increased amount of c-ZrO_2 produced in oxide layer. Besides, from the grazing incidence XRD patterns it appears clearly that there is no c-ZrO_2 on the surface of oxide. Because the c-ZrO_2 exists only inside the oxide film, this is consistent with the result of Li [146]. C-ZrO_2 nucleates during the transformation from t-ZrO_2 to m-ZrO_2. We infer two kinds of transformations occur during corrosion, from tetragonal to monoclinic and from tetragonal to cubic, then to monoclinic phase. Also the existence of c-ZrO_2 relates to the addition of Nb. The stabilization mechanisms of t-ZrO_2 and c-ZrO_2 will be discussed in chapter 8.

Fig.6-7 shows the same result during the oxidation of NZ2 at 400°C in steam. The t-ZrO_2 transforms to m-ZrO_2 versus of the prolongation of the corrosion time. It is worth to note that the c-ZrO_2 is detected in oxide film when the corrosion time is for 14 days (curve 1). Then thickness of the oxide film is 2.1 μm. Further the content of c-ZrO_2 in the film clearly increases for longer time of oxidation (traces 2, 3, 4, 5, 6, 7). Thus, the c-ZrO_2 is a transition phase appearing between the t-ZrO_2 and the m-ZrO_2.

Fig. 6-8 shows the relationship between the content of t-ZrO_2 in oxide films and corrosion time of NZ2 alloy corroded at 400°C and corroded at 360°C in lithuated water. In this figure the variation of thickness of the t-ZrO_2 layer is presented in relative scale, reference to the total amount of formed oxide. It is shown that the relative value of t-ZrO_2 generated in lithiated water remains more than twice that is observed under steam conditions. Moreover, the difference of the temperature, 360 to 400°C, can be considered as an additional parameter favouring less proportion of t-ZrO_2 layers in the second experiment. The time variations of the relative proportion of t-ZrO_2 in both conditions (360°C lithiated water; 400°C steam) fit fairly well with experimental A.exp(-αx) law. Interestingly, it is worth to note that the α get the same value of -33.10^{-5}. The rate of transformation t-ZrO_2 is the same in both experiments. As a result of initial conditions, under lithiated water at 360°C, the thickness of t-ZrO_2 layer is much larger than at 400°C in steam. The c-ZrO_2 phase appears in oxide films when the corrosion transformation concerns with Nb-oxidation process, c-ZrO_2 being an intermediate state between t-ZrO_2 and m-ZrO_2 forms. Since, the protective ZrO_2 layer is found thicker under lithiated water at 360°C, the formation of c-ZrO_2 that we assume correlated with the oxidation of Nb-phase, is effectively more accentuated in steam 400°C.

From the normal XRD patterns, it appears that the relative content in t-ZrO_2 within the oxide film diminishes reference to the amount of m-ZrO_2, which continuously increases with

the duration of corrosion process, where t-ZrO_2 transforms to m-ZrO_2. C-ZrO_2 is a transition phase from t-ZrO_2 to m-ZrO_2 transformation.

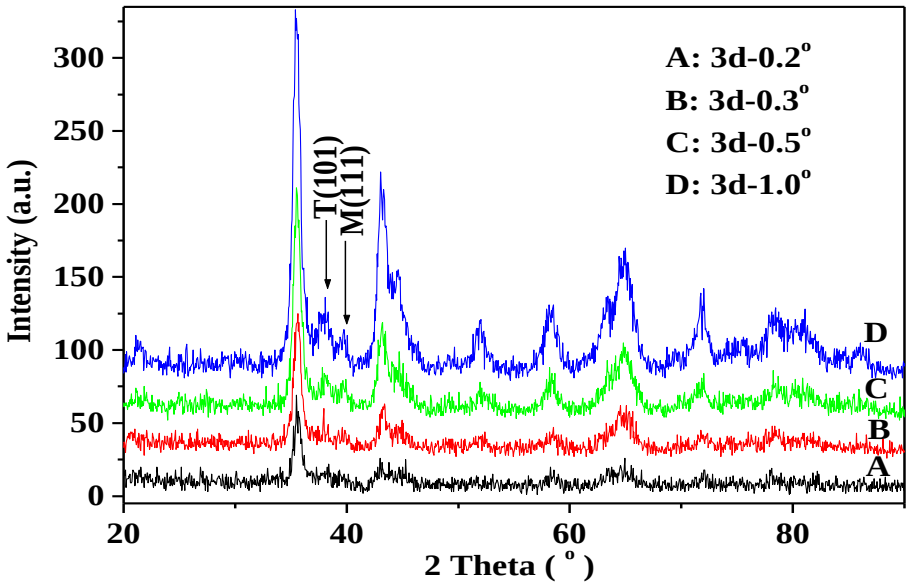

Fig. 6-1 Grazing incidence XRD patterns of the oxide film surface of NZ2 alloy exposed to 360°C lithiated water for 3d

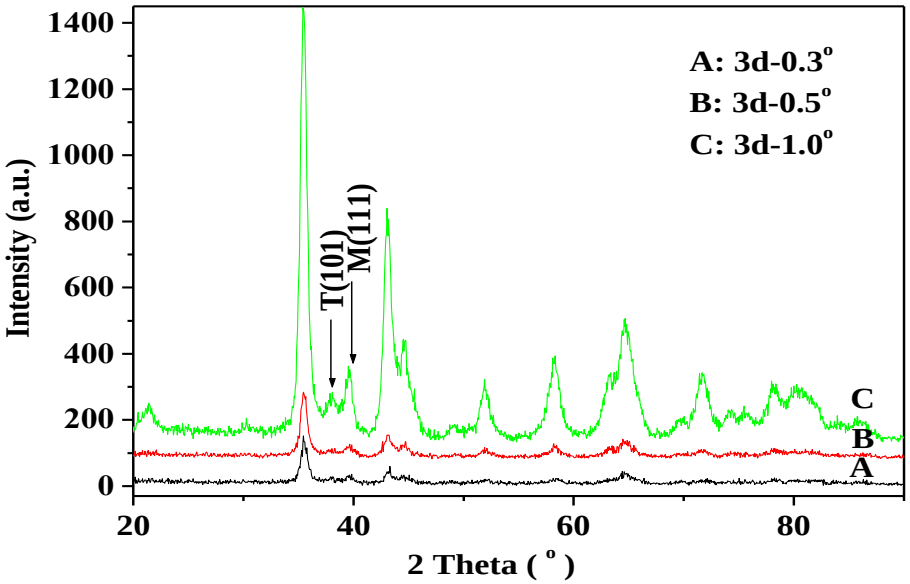

Fig. 6-2 Grazing incidence XRD patterns of oxide film surface of NZ2 alloy exposed to 400°C steam for 3days

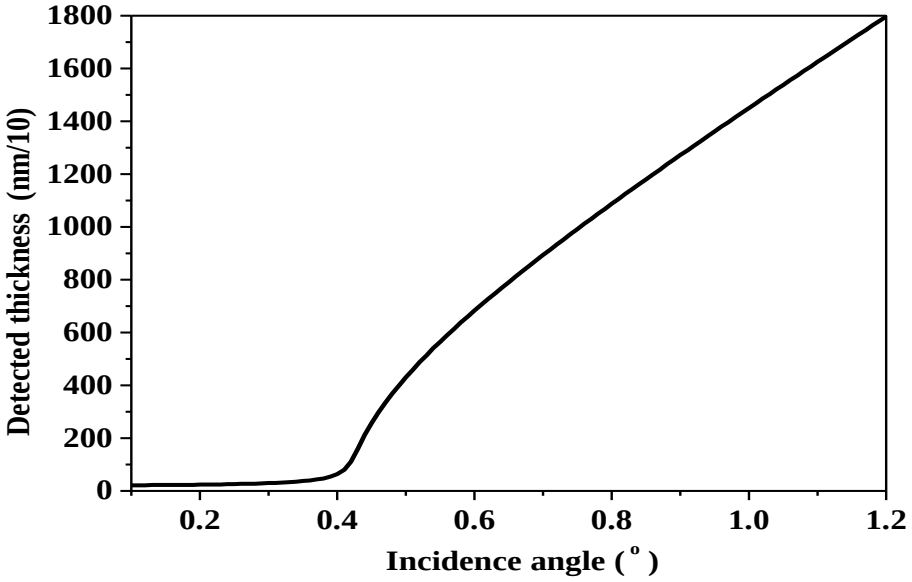

Fig. 6-3 Probed thickness of oxide films versus incidence angles

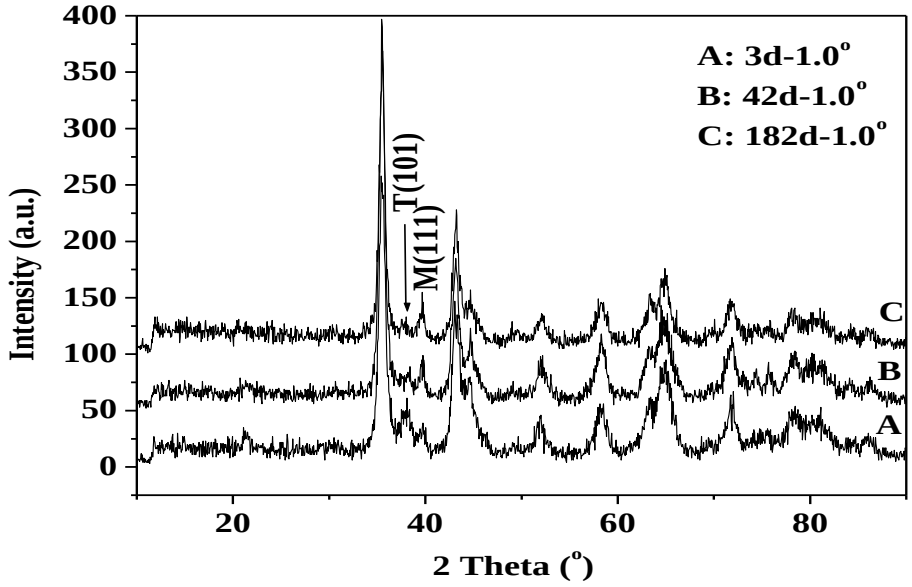

Fig. 6-4 Grazing angle XRD spectrum of oxide film surfaces of NZ2 alloy exposed to 360°C lithiated water for different times

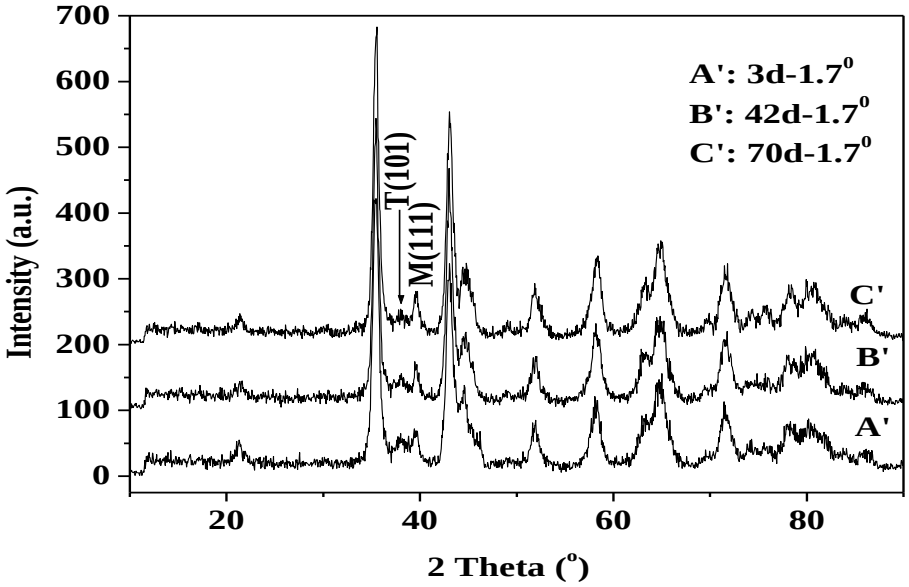

Fig. 6-5 Grazing angle XRD spectrum of oxide film surfaces of NZ2 alloy exposed to 400°C steam for different times

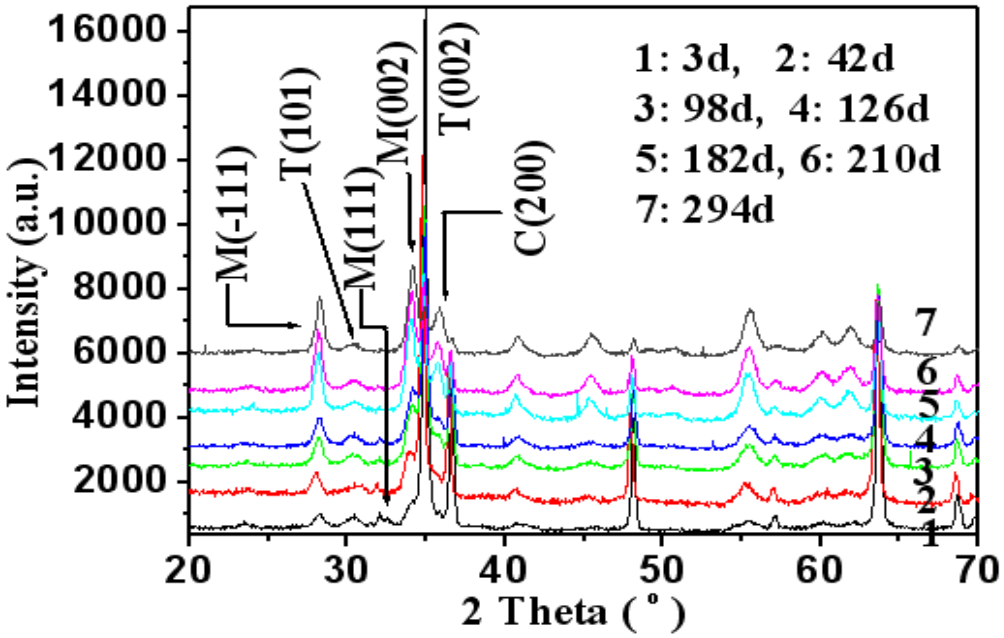

Fig. 6-6 Normal XRD spectrum of NZ2 oxide films exposed to 360°C lithiated water for different times

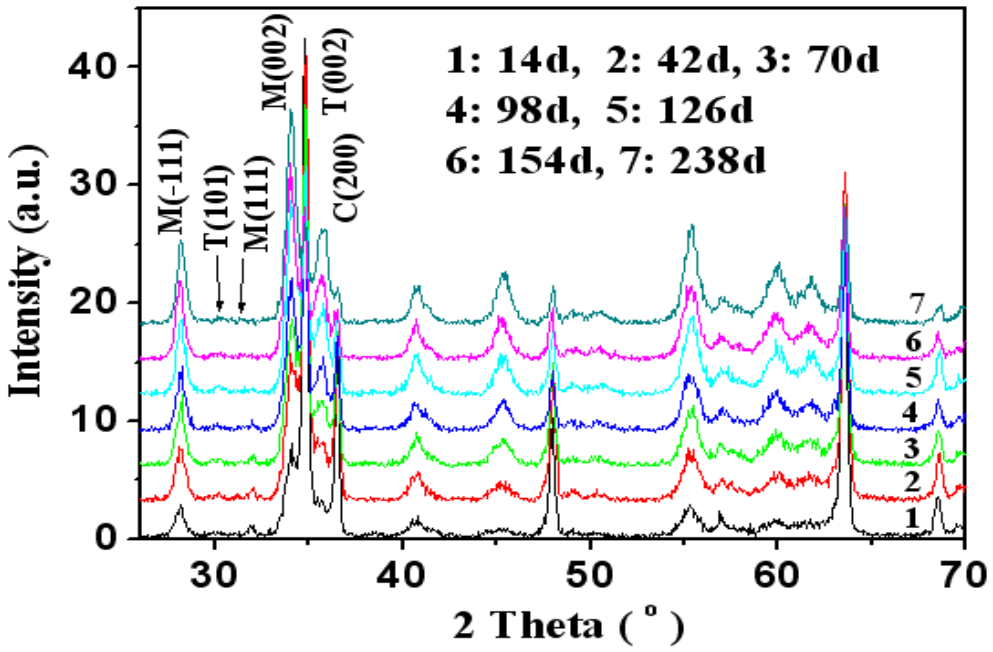

Fig. 6-7 Normal XRD patterns of NZ2 oxide films exposed to 400°C steam for different times

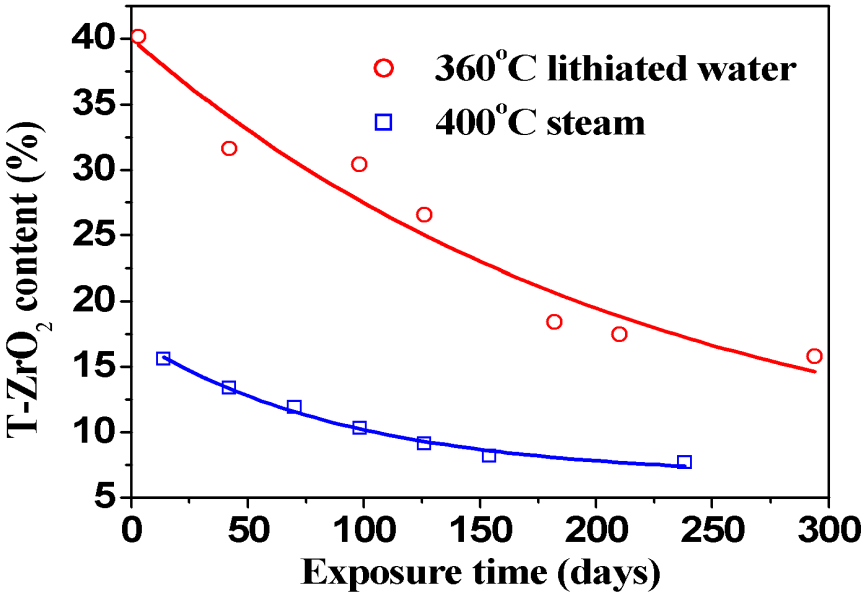

Fig. 6-8 Relation of corrosion time and t-ZrO_2 content in NZ2 oxide films corroded in 360°C lithiated water and 400°C steam

Fig. 6-9 shows the Raman spectra of oxide film for NZ2 alloy exposed to 360°C lithiated water for 14 days, 42 days and 70 days (pre-transition samples). For each spectrum, the peak positions, intensities (relative to the more intense monoclinic peak at about 177.6 cm^{-1}), and shifts (the shift is defined here as the difference between the actual peak position and the position of the equivalent peak on powders which is showed in Tab. 6-1 [148]) are presented in

Tab. 6-2. It is clear that the peak at about 280 cm^{-1} and 440 cm^{-1} are not found on powders and become weaker when increasing the oxidation time. All the other peaks belong to m-ZrO_2. However, the small shifts are observed between the positions of m-ZrO_2 peaks in the powder and in the film, and the maximal shift is 4.3 cm^{-1}. The peaks at about 280 cm^{-1} and 440 cm^{-1} are caused by the shift of the 267.1 cm^{-1} and 456 cm^{-1} peaks of t-ZrO_2, and the shift reason will be discussed in this paper. The shifts of 267.1 cm^{-1} and 456 cm^{-1} peaks are more than 10 cm^{-1}. First, it's considered that the shift is caused by compressive stress in oxide film [148]. However, for an isotropic pressure, the shift of the most characteristic t-ZrO_2 peak (267.1 cm^{-1}) should be about 1.0 $cm^{-1}GPa^{-1}$. This would imply compressive stress of more than 10 GPa, that is far greater than the mean stress (1-3 GPa). In addition, the stress should affect also the m-ZrO_2 peaks in the same manner. The maximal peak shift of m-ZrO_2 is 4.3cm^{-1} in this experiment. So it's determined that the compressive stress is not the only factor of the peak shifts. Secondly, the chemical shifts caused by alloying elements are considered. The alloying elements are precipitated in the metal matrix. During the oxidation of NZ2 alloy, the precipitates oxidize and alloying elements will dissolve in the surrounding oxide, which results in the peak shifts of ZrO_2. Finally, we assumed that the shifted peak should be attributed to a distorted t-ZrO_2 phase, with atom positions in the cell and lattice space different from that in powder. In this structure, the displacement of the oxygen atom from its position in the cubic phase is greater than that in t-ZrO_2 powder. The displacement of the oxygen atom also causes to the Raman peak shifts. That is to say, compressive stress, chemical factor and the deviation of lattice space are the reasons of Raman peak shifts. The result is consistent with the study of Pierre [149].

Fig. 6-10 shows the Raman spectra of oxide film for NZ2 alloy exposed to 400^{o}C steam for 14 days, 42 days and 70 days. The same result is obtained that the t-ZrO_2 peak at about 280 cm^{-1} and 440 cm^{-1} become weaker when increasing the oxidation time. When the corrosion time reaches 42 days, the peak at 440 cm^{-1} disappears. And the peak at 280 cm^{-1} also disappears at 70 days corrosion time. The t-ZrO_2 content in the oxide film of NZ2 alloy corroded in 360^{o}C lithiated water is higher than that in 400^{o}C steam. The total integrated intensities I(hkl) of the t-ZrO_2 peak at 280 cm^{-1} and the m-ZrO_2 peaks at about 179 cm^{-1}, 189cm^{-1}, were used to determine the t-ZrO_2 volume fraction with respect to the total volume of ZrO_2 by the Godlewski's formula [150]:

$$f_T = \frac{I_T(280)}{I_T(280) + I_M(179) + I_M(189)}$$

The result of calculation as shown in Tab. 6-3, confirms the above conclusions. Namely, the t-ZrO_2 content is decreasing and it is transforming to m-ZrO_2. So we think that the lower the t-ZrO_2 content in oxide film is, the higher the corrosion rate is. This is consistent with the XRD results and other's studies [151-160]. Here, the formula is likely biased, because it was established on stabilized t-ZrO_2, with peaks at 264 cm^{-1} instead of 280 cm^{-1} and the calculation results are different those by XRD method. The present analysis is only a guide to appreciate the main impact of the corrosion time on the oxide layer transformation.

Fig. 6-11 shows the Raman spectra of oxide film at different distances from the surface, the oxide film was gained by exposing NZ2 alloy to 360^{o}C lithiated water for 70 days. It is observed that the phase structure and content at different distances from the surface are different. From the surface to metal/oxide interface, the t-ZrO_2 peak intensity is increasing gradually, and the t-ZrO_2 peak intensity is the highest at the oxide/metal interface. This is consistent with the simulation results of P. Barberis [161]. Fig. 6-12 shows the Raman spectra of oxide film at different distances from the surface, the oxide film was gained by exposing NZ2 alloy to 400^{o}C steam for 70d. It is shown that there is only a few t-ZrO_2 at the

oxide/metal interface, there is no t-ZrO_2 on the surface of oxide film. The relative intensity of t-ZrO_2 peak in this medium is much lower than that in 360°C lithiated water, and the peak at about 440 cm^{-1} is not observed here. The t-ZrO_2 content at different thickness of oxide film in Fig. 6-11 and Fig. 6-12 was calculated by the same formula, which validates the above results. That's to say, there is high proportion t-ZrO_2 at the oxide film/metal interface. With the corrosion process, the oxide film/metal interface advances, and the t-ZrO_2 formed previously transforms to m-ZrO_2, which leads to the decreasing of t-ZrO_2 away from the interface. The t-ZrO_2 content at the oxide/metal interface of the NZ2 sample exposed in 360°C lithiated water for 70 days is 28.5%, higher than that (4.3%) in 400°C steam for 70 days. So the higher t-ZrO_2 content is, the corrosion resistance is better.

Fig. 6-13 and Fig. 6-14 show SEM images of oxide sections of NZ2 alloy exposed to 360°C lithiated water and 400°C steam for 3 days. It is clear that the oxide is intact when the alloy is corroded for 3 days and there is no crack. When the corrosion time reaches 126 days (transition point), there are some cracks in the oxide films. This indicates that the corrosion rate increasing is related to the defect evolvement in the oxide. The micro-cracks and holes in the oxide destroy the stabilization of the oxide film and accelerate the oxide growth. However the oxide growth also affects the production and development of defects. Vacancies and holes mainly are caused by the volume expander of zirconium matrix oxidation, but micro-cracks mainly are produced by the phase transformation from t-ZrO_2 to m-ZrO_2 and the stress release.

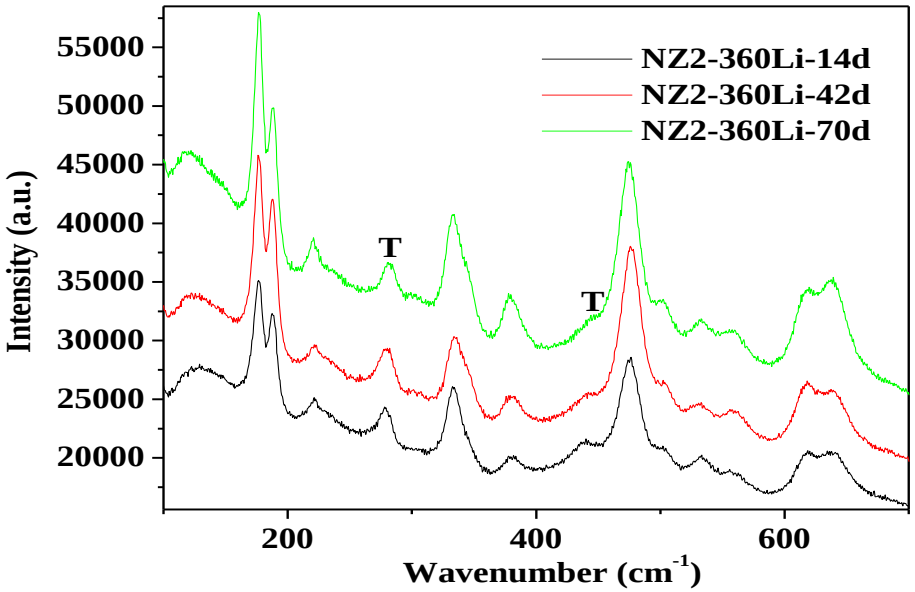

Fig. 6-9 Raman spectra of NZ2 oxide films exposed to 360°C lithiated water for 14, 42 and 70 days

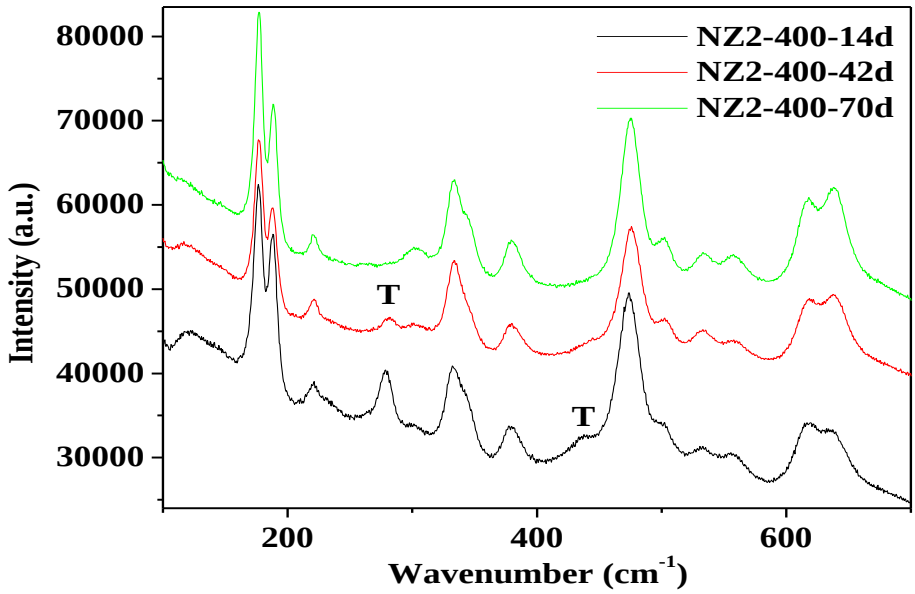

.

Fig. 6-10 Raman spectra of NZ2 oxide films exposed to 400°C steam water for 14, 42 and 70 days

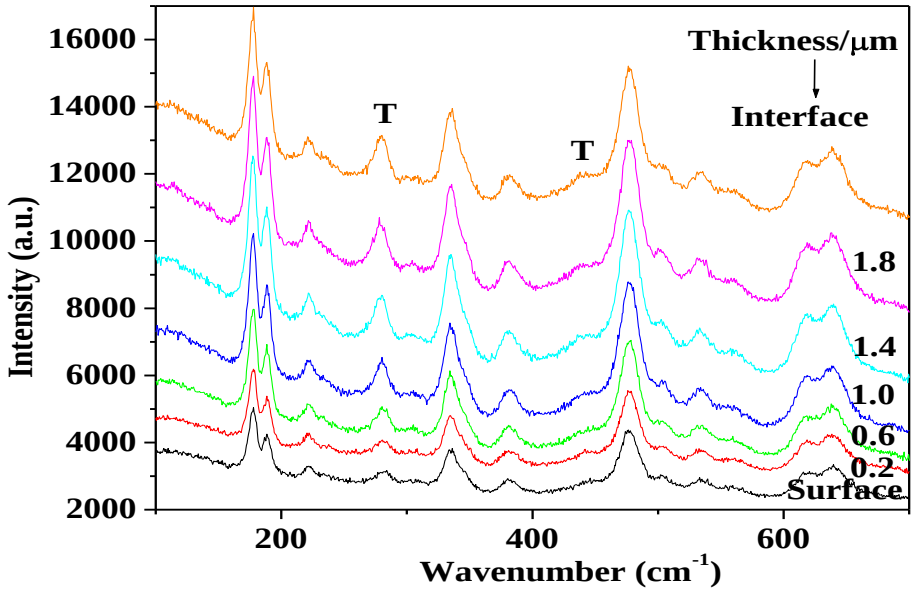

Fig. 6-11 Raman spectra of oxide films at difference distances from surface, which was gained by exposing NZ2 alloy to 360°C lithiated water for 70 days

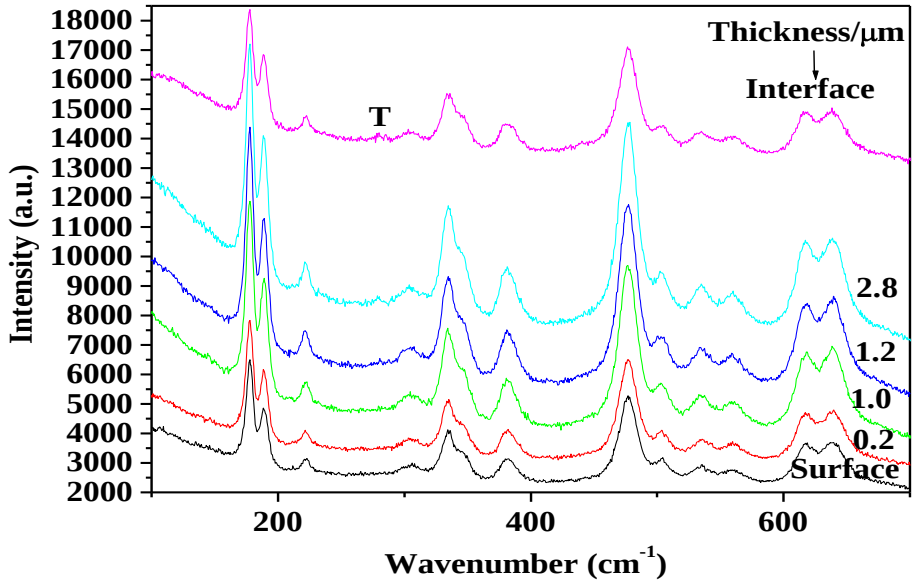

Fig. 6-12 Raman spectra of oxide films at the difference distances from surface, which was gained by exposing NZ2 alloy to 400°C steam for 70 days

Tab.6-1: Raman spectra peak positions of pure t-ZrO_2 and m-ZrO_2 powder [148]

Monoclinic	Tetragonal
145.9	
158.0	
177.4	
189.5	
221.4	
	267.1
306.0	
	315.1
332.5	
346.6	
381.1	
	456
474.6	
500.2	
537.1	
557.9	
	607.1
615.2	
637.6	
	644.5

Tab. 6-2: Peak positions, intensities (relative to the most intense 177.6 cm^{-1}), and shift of the Raman peaks of NZ2 oxide films exposed in 360°C lithiated water for 14, 42 and 70d

14d			42d			70d			Attribution
position (cm^{-1})	relative intensity	shift (cm^{-1})	position (cm^{-1})	relative intensity	shift (cm^{-1})	position (cm^{-1})	relative intensity	shift (cm^{-1})	
177.6	100	-0.2	177.6	100	-0.2	177.6	100	-0.2	M
187.4	77.6	2.1	187.4	78.8	2.1	187.4	63.4	2.1	M
221.0	22.4	0.4	221.0	9.7	0.4	221.0	17.4	0.4	M
278.1	**28.5**	**-11**	**278.1**	**19.9**	**-11**	**278.1**	**16.9**	**-11**	**T**
334.0	56.7	-1.5	334.0	36.4	-1.5	334.0	47.0	-1.5	M
379.9	15.6	1.2	379.9	13.3	1.2	379.9	20.0	1.2	M
439.1	**31.0**	**16.9**	**439.1**	**18.8**	**16.9**	**439.1**	**15.5**	**16.9**	**T**
476.9	71.5	-2.3	476.9	97.5	-2.3	476.9	85.9	-2.3	M
503.8	31.0	-3.6	503.8	29.0	-3.6	503.8	28.5	-3.6	M
532.9	25.9	4.2	532.9	18.8	4.2	532.9	21.1	4.2	M
556.3	15.4	1.6	556.3	16.9	1.6	556.3	18.5	1.6	M
619.0	34.3	-3.8	619.0	36.4	-3.8	619.0	41.0	-3.8	M
637.9	36.1	-0.3	637.9	32.7	-0.3	637.9	46.5	-0.3	M

Tab. 6-3: Relation of corrosion time and t-ZrO_2 content in NZ2 oxide films corroded in 360°C lithiated water and 400 °C steam

Corrosion time	T-ZrO_2 content (%)	
(days)	360 °C lithiated water	400 °C steam
14	17.8	18.0
42	17.5	6.2
70	13.7	—

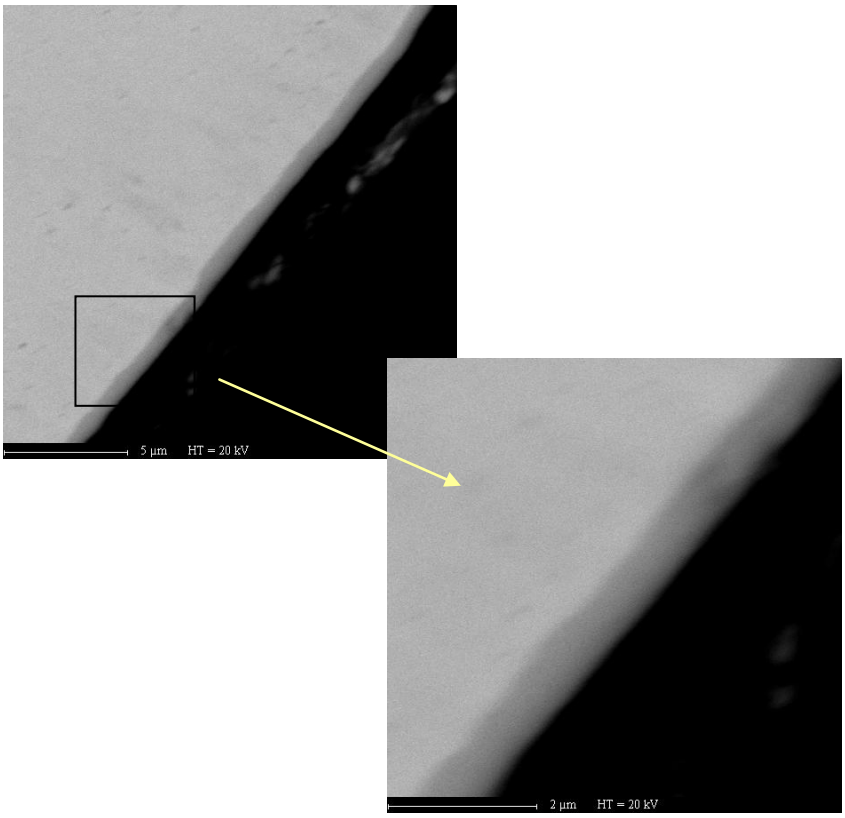

Fig. 6-13 SEM image of NZ2 oxide films exposed to 360^{o}C lithiated water for 3 days

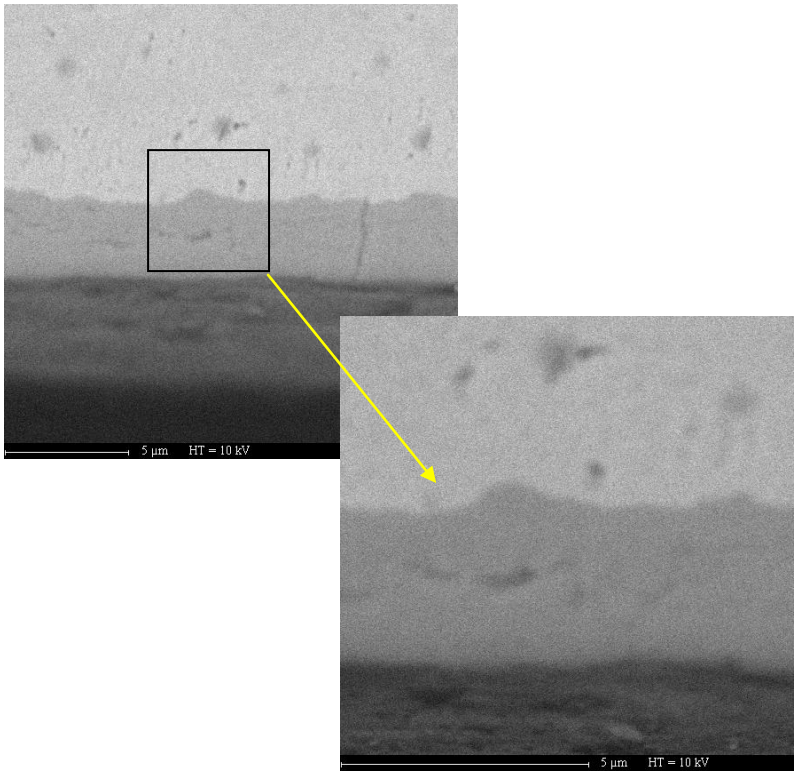

Fig. 6-14 SEM image of NZ2 oxide films exposed to 360 ^{o}C lithiated water for 126 days

6.3 The crystal structure of NZ8 alloy oxide films

Fig. 6-15 shows the normal XRD patterns of the oxide films of NZ8 alloy exposed to 360^{o}C lithiated water for 14 days and 98 days. It is clear that the intensity of M(002) Bragg peak increases and that of T(002) one decreases with the corrosion process. t-ZrO_2 changes to m-ZrO_2. This is consistent with the results of NZ2 alloys.

In Fig. 6-15, trace 2 corresponding to (200) diffraction of c-ZrO_2 phase appears when the corrosion time reaches 98 days and the oxide film thickness is 2.2 μm. This indicates that c-ZrO_2 nucleates before the corrosion transition (126 days) happens.

Fig. 6-16 shows the normal XRD patterns of the oxide films of NZ8 alloy exposed to 400^{o}C steam for 42 days and 70 days. This result is consistent with the above results. With the corrosion process, t-ZrO_2 changes to m-ZrO_2.

In Fig. 6-16, when the corrosion time reaches 42 days and the oxide films thickness is 2.6μm, a weak (200) peak of c-ZrO_2 appears (curve 1). c-ZrO_2 nucleates before the corrosion transition (70 days) happens. With the corrosion time prolongation, the c(200) peak intensity is obviously enhanced. Namely the content of c-ZrO_2 in the post-transition oxide films increases.

Fig. 6-17 shows the Raman spectra of oxide films for NZ8 alloy exposed to 360^{o}C lithiated water for 14 days and 98 days. For each spectrum, the peak positions, intensities, and shifts are presented in Tab. 6-4. It's clear that the peak at about 280 cm^{-1} is not found on powders and becomes weaker when increasing the oxidation time. All the other peaks belong to m-ZrO_2. However, the small shifts are observed between the positions of m-ZrO_2 peaks in the powder and in the film. The peak at about 280 cm^{-1} is caused by the shift of the 267.1 cm^{-1} peak of t-ZrO_2, and the shifts of 267.1 cm^{-1} peak is more than 10 cm^{-1}. The compressive stress, chemical factor and the deviation of lattice space are the reasons of Raman peak shifts. The result is consistent with the study of NZ2 alloy.

Fig. 6-18 shows the Raman spectra of oxide films for NZ2 alloy exposed to 400^{o}C steam for 42 days and 70 days. The same result is obtained that the t-ZrO_2 peak at about 280 cm^{-1} becomes weaker when increasing the oxidation time. When the corrosion time reaches 70 days, the peak at 280 cm^{-1} disappears. The t-ZrO_2 content in the oxide films of NZ8 alloy corroded in 360^{o}C lithiated water is higher than that in 400^{o}C steam. The t-ZrO_2 volume fraction with respect to the total volume of ZrO_2 is determined by the formula 6-2. The result of calculation as shown in Tab. 6-5, confirms the above conclusions. Namely, the t-ZrO_2 content is decreasing and it is transforming to m-ZrO_2. The lower the t-ZrO_2 content in oxide film is, the higher the corrosion rate is.

Fig. 6-19 shows the Raman spectra of oxide films at different distances from the surface, the oxide films were gained by exposing NZ8 alloy to 360^{o}C lithiated water for 98 days. It is observed that the phase structure and content at different distances from the surface are different. From the surface to metal/oxide interface, the t-ZrO_2 peak intensity is increasing gradually, and the t-ZrO_2 peak intensity is the highest at the oxide/metal interface. The t-ZrO_2 content at different thickness of oxide films in Fig. 6-19 is calculated by 6-2 formula, and the calculation result is shown in Fig. 6-21, which validates the above results.

Fig. 6-20 shows the Raman spectra of oxide films at different distances from the surface, the oxide films were gained by exposing NZ8 alloys to 400^{o}C steam for 70 days. This shows the same result. However the t-ZrO_2 characteristic peak intensity in this medium is much lower than that in 360^{o}C lithiated water, and the t-ZrO_2 characteristic peak does not appear at the surface in this medium.

Comparing the results of NZ2 and NZ8, we find that the t-ZrO_2 content of NZ2 alloys oxide film is higher that of NZ8 alloy oxide films in the same corrosion medium. So the corrosion resistance is improved by increasing the t-ZrO_2 content in the oxide films.

6.4 Summary of the chapter

The oxide films of new zirconium alloys mainly consist of m-ZrO_2 and some distorted t-ZrO_2. c-ZrO_2 appears when the oxide films thickness reaches about 2 μm, and the amount of c-ZrO_2 in the post-transition oxide films is obviously increased. During the corrosion, there two kinds of phase transformations, t-ZrO_2 $\longrightarrow$ m-ZrO_2, and t-ZrO_2 $\longrightarrow$ c-ZrO_2 $\longrightarrow$ m-ZrO_2. The c-ZrO_2 is a transition phase. With the corrosion process, the t-ZrO_2 content decreases gradually, which is not related the kinetics transition. That is to say, there is no sudden decreasing of t-ZrO_2 content at the transition point. In the whole oxide films, the phase structure and content at different distances from the surface are different. From the surface to metal/oxide interface, the t-ZrO_2 content is increasing gradually, and the t-ZrO_2 content is the highest at the oxide/metal interface. The t-ZrO_2 is mainly stabilized by the oxygen vacancies and compressive stresses caused by the oxidation of Zr matrix and the precipitates. The t-ZrO_2 transformation is a main factor deciding the corrosion resistance. The higher t-ZrO_2 content is, the better corrosion resistance is.

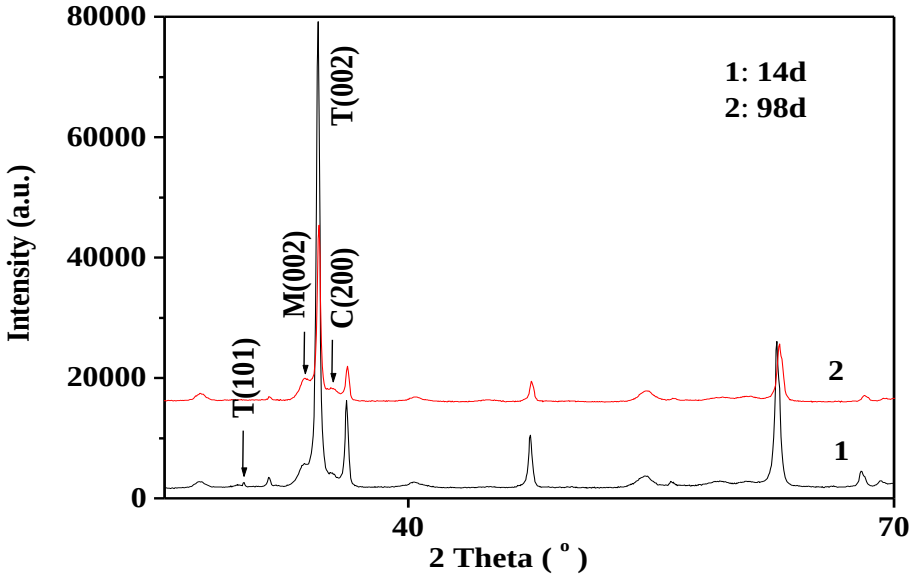

Fig. 6-15 XRD patterns of NZ8 oxide films exposed to 360°C lithiated water for different times

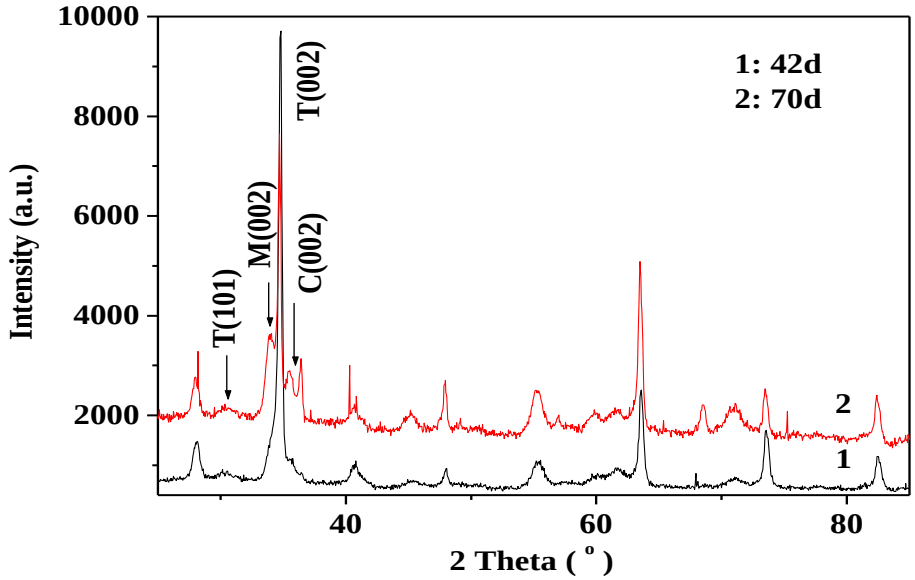

Fig. 6-16 XRD patterns of NZ8 oxide films exposed to 400°C steam for different times

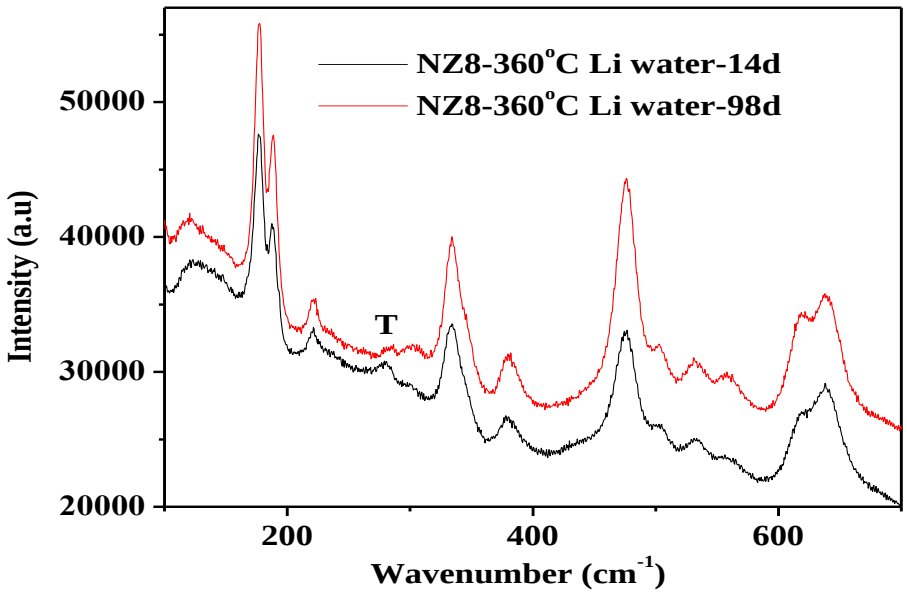

Fig. 6-17 Raman spectra of NZ8 oxide films exposed to 360°C lithiated water for 14 and 98 days

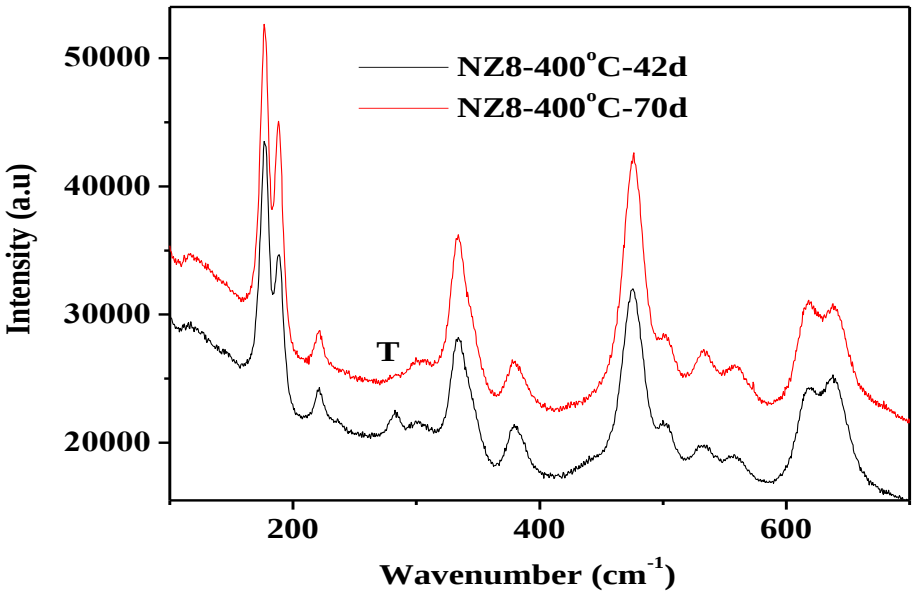

Fig. 6-18 Raman spectra of NZ2 oxide films exposed to 400 °C steam water for 42 and 70 days

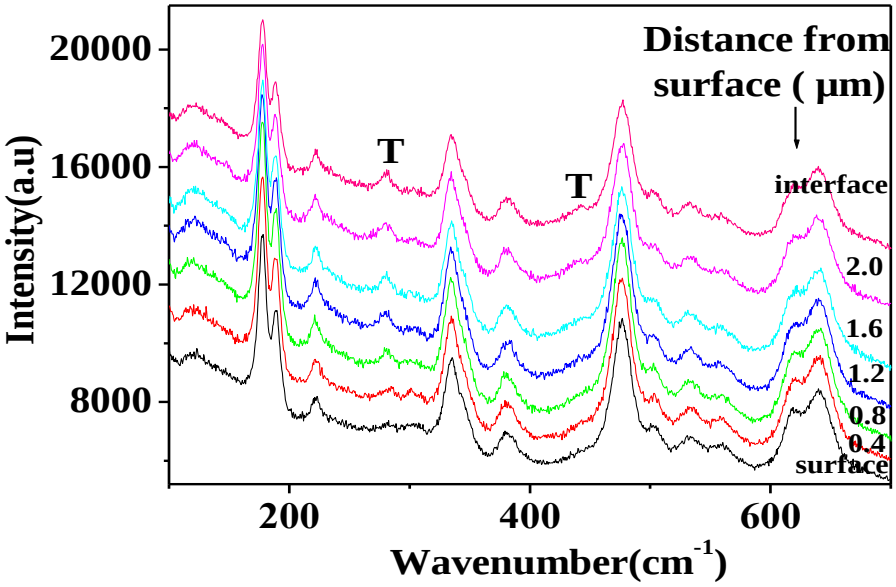

Fig. 6-19 Raman spectra of oxide films at different distances from the surface, the oxide films were gained by exposing NZ8 alloys to 360°C lithiated water for 98 days

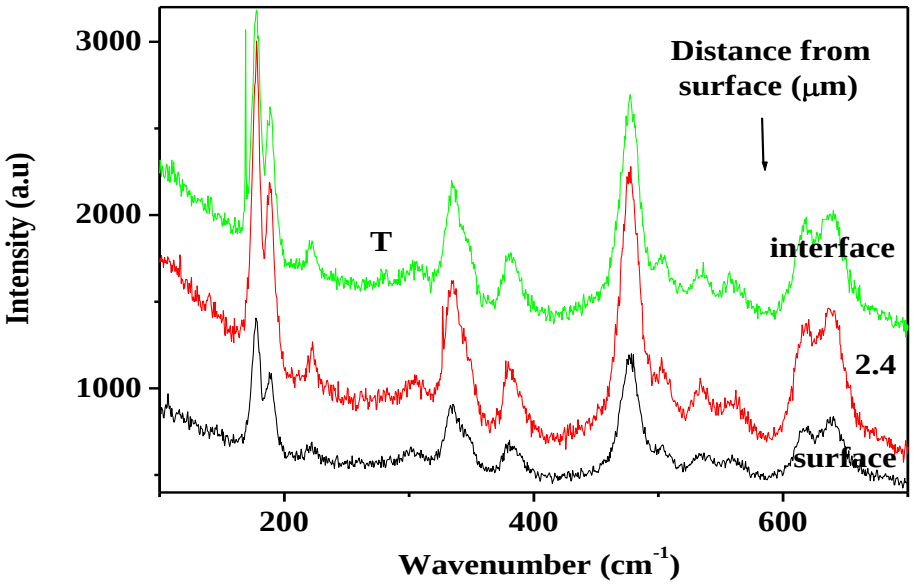

Fig. 6-20 Raman spectra of oxide films at different distances from the surface, the oxide films were gained by exposing NZ8 alloy to 400°C steam for 70 days

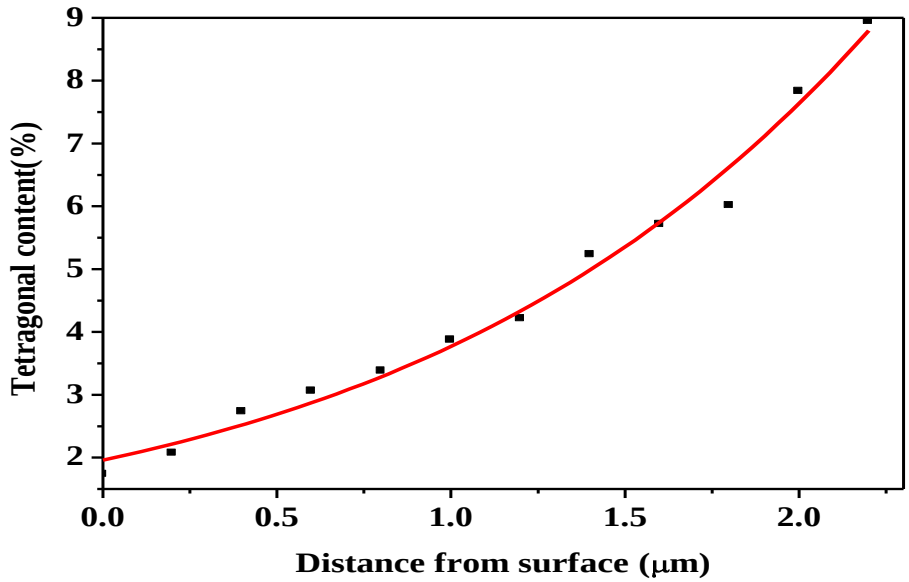

Fig.6-21 The t-ZrO_2 content at different thickness of NZ8 oxide films exposed to 360°C lithiated water for 98 days

Tab. 6-4: Peak positions, intensities (relative to the most intense 177.6 cm^{-1}), and shifts of the Raman peaks of NZ8 oxide films exposed in 360 ^{o}C lithiated water for 14 and 98 days

14d			98d			
position (cm^{-1})	relative intensity	shift (cm^{-1})	position (cm^{-1})	relative intensity	shift (cm^{-1})	Attribution
177.6	100	-0.2	177.6	100	-0.2	M
188.2	58.4	1.3	188.2	64.5	1.3	M
221.3	16.2	0.1	222.6	14.5	-1.2	M
279.1	**15.6**	**-12**	**283.9**	**6.7**	**-16.6**	**T**
303.0	10.8	3.0	302.8	9.0	3.2	M
334.8	49.4	-2.3	334.8	54.3	-2.3	M
379.6	15.5	1.5	380.7	15.7	0.4	M
475.3	66.8	-0.7	476.3	86.9	-1.7	M
503.6	22.3	-3.4	503.6	25.5	-3.4	M
532.8	18.1	4.3	532.8	20.4	4.3	M
557.9	10.9	0.0	557.9	16.5	0.0	M
618.2	38.5	-3.0	619.2	41.0	-4.0	M
639.2	54.8	-1.6	638.2	48.0	-0.6	M

Tab. 6-5: Relation of corrosion time and t-ZrO_2 content in NZ8 oxide films corroded in 360^{o}C lithiated water and 400^{o}C steam

Corrosion Conditions	Corrosion time (days)	T-ZrO_2 content (%)
360^{o}C Li-water	14	9.11
	98	3.43
400^{o}C steam	42	6.11
	70	0.89

Chapter 7

Relationships between residual stresses and crystal structure of oxide films and corrosion resistance

Chapter 7 Relationships between residual stresses, crystal structure of oxide films and corrosion resistance

7.1 Introduction

Corrosion testing results of zirconium alloys indicate that the stresses change with the corrosion when the oxide films growth. The stresses are mainly derived from the volume change of metal and oxide, the phase transformation from t-ZrO_2 to m-ZrO_2, the oxidation of the precipitates et al. During the oxidation of zirconium alloys, there are high compressive stresses in the oxide films and tensile stresses in the metal [162]. With the corrosion process, t-ZrO_2 transforms to m-ZrO_2. Because the crystal lattice constants t-ZrO_2 and m-ZrO_2 are different, there are large phase stresses during the transformation. The oxidation of zirconium alloy happens at the oxide/metal interface. A new oxide film forms gradually at the oxide/metal interface, and the phase transformation also continues. The stresses caused by the form of new ZrO_2 and phase transformation will affect the stabilization of the oxide films, and change the diffusing coefficient. Thus the corrosion kinetics is changed [163,164].

Many works [165-170] confirmed that the high compressive stresses, resulting from high Pilling-Bedworth ratio of ZrO_2/Zr, exist in the oxide films of zirconium alloys. The corrosion rate of zirconium alloys is closely related to the value and the distribution of the compressive stresses. These compressive stresses favour the formation of the t-ZrO_2 phase at room temperature and pull off the corrosion transition, improve the corrosion resistance. However, some studies also yielded rather controversial results [175,176]. Whatever, the compressive residual stresses are closely related to the corrosion kinetics and the microstructure of the growing oxide, and influence the corrosion mechanism [11,12]. Therefore, it is crucial to characterize as accurately as possible the residual stress state and the microstructure(specifically the t-ZrO_2 fraction) of the oxide films formed on zirconium based alloys to better understand the eventual relationship between oxide phases, oxidation kinetics and stresses, confirm the corrosion mechanism. In this paper, the compressive stresses of the oxide films were investigated using x-ray diffraction techniques.

7.2 Principles

The interatomic distance of reflecting plane *d* is invariable for a certain material. When X-ray enters the lattice, there is crystal diffraction. There is a certain relation between the diffraction angle θ and crystal plane distance *d*. When the stress makes *d* change, θ also changes. The stress is calculated according to crystal plane distance *d* change measured by X-ray diffraction. This is the stress measurement method. The principle of X-ray diffraction is shown in Fig. 7-1.

X-ray can probe to certain region in materials and form certain intensity distribution. According to the change of intensity distribution, the diffraction angle θ shift, caused by the crystal lattice strain under stress, can be recorded. This can be described by the Bragg formula:

$$2d\sin\theta = n\lambda \qquad (7\text{-}1)$$

The differential form is

$$\frac{\Delta d}{d} = -ctg\theta \cdot \Delta\theta \qquad (7\text{-}2)$$

So the plane distance *d* change can be expressed by the $\Delta\theta$.

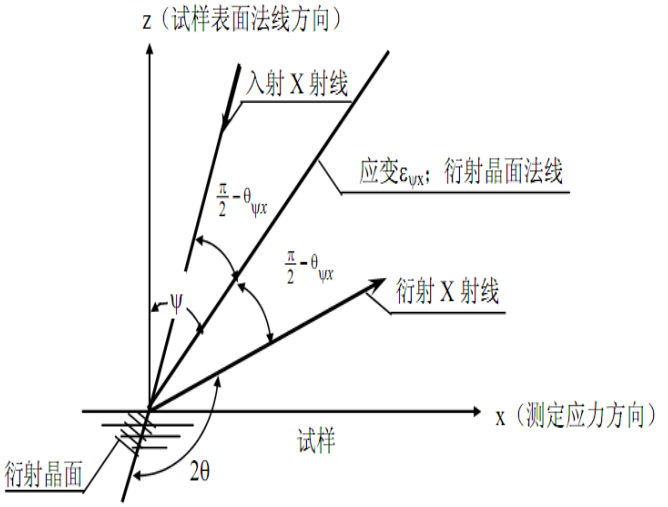

Fig. 7-1 Principle of X-ray diffraction

For the multi-crystal material, there are many crystals in the area probed by X-ray, and the tropism of every crystal is inordinate. So when X-ray enters the crystal, many crystals take part in the diffraction.

If the sample is under the external force or residual stress, the （*hkl*） plane strain in the crystals distributed in different directions is not the same. So when X-ray enters the sample in different angles of incidence ψ, we can measure the change rule of 2θ with ψ.

The basic formula used to test stress by X-ray method is

$$\sigma_x = K \cdot M \qquad (7\text{-}3)$$

in the formula 7-3

$$K = -\frac{E}{2(1+\mu)} \cdot \frac{\pi}{180} \cdot ctg\theta_o \qquad (7\text{-}4)$$

K is the stress testing constant, indicating the mechanics property of material; σ_x is the stress along X direction; M is stress testing factor, namely the change rate 2θ with ψ.

$$M = \frac{\partial(2\theta_{\psi x})}{\partial(\sin^2\psi)} \qquad (7\text{-}5)$$

In fact, the testing stress is a process calculating the *M* value. Obviously, σ_x is a vector, so we can confirm the value and direction by at least two points. In other words, the line indicating *M* must be plot by at least two points. So more two angles of incidence are chose during the testing to get the $2\theta_{\psi x}$ corresponding to different angles of incidence. Thus $2\theta_{\psi x}$-$\sin^2\psi$ line can be plot. According to the slop *M* of $2\theta_{\psi x}$-$\sin^2\psi$ line, the σ_x can be calculated.

7.3 Experimental methods

To determine the residual stress state in the sample by X-ray diffraction, the specimen must be rotated along two axes. One rotation is characterized by the title angle ψ between the normal to the specimens surface P_3 and the normal L_3 to the diffracting planes of spacing d_{hkl}, which is parallel to the diffraction vector Q. This title can be accomplished by a rotation about an axis L_2 lying on the specimen surface and perpendicular to the diffraction plane, defined by the incident and the diffracted beams k_0 and k_1, respectively, i.e. using the Ω-diffractometer (Fig.7-2). It can also be achieved by a rotation about an axis lying on the specimen surface and belonging to the diffraction plane, but perpendicular to the diffraction vector Q, i.e. using the ψ-diffractometer (Fig.7-3). The second rotation is characterised by the azimuth angle Φ and is executed about an axis parallel to the specimen normal P_3.

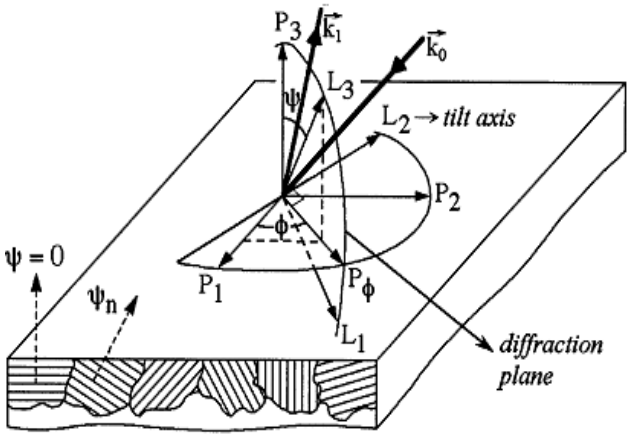

Fig. 7-2 Ω-diffractometer

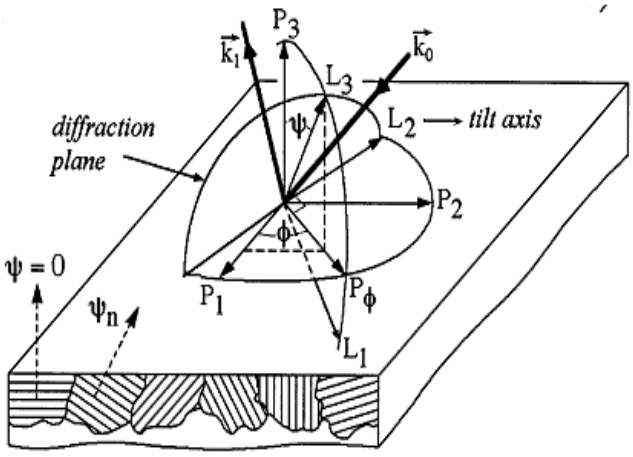

Fig. 7-3 ψ-diffractometer

In this thesis, the residual stresses in the oxide films of the samples, oxidized in 360°C lithiated water and 400°C steam, have been determined on the $(\bar{1}04)_m$ planes of the m-ZrO_2 (corresponding to a $2\theta_0$ angular position = 71.226^0 for Cu $_{K\alpha}$ radiation) as usually reported [179,180]. The stress state of the phase is different from that of t-ZrO_2 and the value measured must be different from the average stress. The mean residual stress determination by XRD method uses the lattice parameters as local strain gauges.

Microstrains are given by the relation:

$$\varepsilon = (\frac{d-d_0}{d_0})_{hkl} = -\frac{1}{2}\cot g\theta_0 * (2\theta - 2\theta_0) \qquad (7\text{-}6)$$

where d_0 is the stress free interatomic distance of the *(hkl)* reflecting planes, θ_0 is the stress free Bragg peak position.

By diffraction, the strains of the lattice are measured and the elastic stresses are determined by the continuous mechanics analysis. In standard procedures, the material is considered to be homogeneous and isotropic. Lattice strains are assumed to be homogeneous in analyzed diffracting volume [181].

The distances between atomic planes vary as a function of ψ if there are some macroscopic stresses in the material. By the ‹sin^{2}ψ› method, the diffraction peak shift can be described as follows:

$$2\theta = 2\theta_0 - (\frac{1}{2}S_2)\frac{360}{\pi}\tan\theta_0[\sigma_{11}\sin^2\psi + \sigma_{13}\sin(2\psi)] - (S_1)\frac{360}{\pi}\tan\theta_0[\sigma_{11}+\sigma_{22}] \qquad (7\text{-}7)$$

where 1/2 S_2 and S_1 represent the elastic constants defined for an isotropic material by $\frac{1}{2}S_2 = \frac{1+\nu}{E}$ and $S_1 = \frac{-\nu}{E}$, σ_{ij} is the average stress intensity.

For the oxide film of NZ2 alloy, the stresses are thought to be biaxial state ($\sigma_{11}=\sigma_{22}$, $\sigma_{13}=0$). We can get the formula from above two relations:

$$d = (\frac{1+\nu}{E})d_0\sigma_{11}\sin^2\psi - \frac{2\nu}{E}\sigma_{11}d_0 + d_0 \qquad (7\text{-}8)$$

So σ_{11} is deduced from the slope p of the d-sin$^2\psi$ line:

$$p = (\frac{1+\nu}{E})d_0\sigma_{11}, \text{ (E=281 GPa and } \nu\text{=0.29 [182])}$$

In the case of crystal anisotropy, the elastic strains are linear fuction of the stresses through the stiffness tensor and are expressed by the relation :

$$\varepsilon_{kl} = S_{ijkl}\sigma_{kl} \qquad (7\text{-}9)$$

where ε_{kl} are the components of the elastic strain tensor and S_{ijkl} are the compliance coefficients.

The growth of zirconia films of zirconium alloys leads usually to a fibre texture, which was observed to remain constant with the oxide thickness [183-185]. In that case, an orthotropic elastic model would be a more appropriate description [183] and the precise knowledge of the S_{ijkl} is necessary for stress determination from strain measurements. The existing models [186,187] have been developed for the cubic of hexagonal structures but they are not appropriate for monoclinic crystal. Moreover, stress gradients could be expected and are not take into account in the equations presented. All these considerations show that what is determined is

not homogeneous bulk stresses but rather average 'pseudo-stresses', whose absolute values are questionable, but whose evolution can be considered though cautiously.

7.4 Experimental conditions and data processing

The residual stresses in the oxide films of the samples have been determined on the m-ZrO_2. Indeed, measurements were made at the rather low angle of 71.226^0 for the $(\bar{1}04)_m$ peak to have a high enough diffracted intensity. In addition, this peak is close to two peaks of the Zr matrix: （201）and (004) and is rather broad, due to the very fine grain size [188,189]. Therefore, a careful procedure is required for peak fitting and extraction. These three overlapping components were extracted using the following manual procedure.

Data processing was performed with the Igor software using the three following steps: (1). On each signal, the background noise is subtracted by linear interpolation from its value outside the peaks. (2) In order to improve signal-to-noise ratio, a Fourier Transformation Filter procedure is performed. (3) As clearly observed, three Gaussian peaks are assumed to be present for profile fitting, with a free position of each of them. Each spectrum has been processed individually. Error bars displayed on the curves are taking into account all the experimental errors and uncertainties in the fitting procedures. Then, the $(\bar{1}04)_m$ peak is obtained and the corresponding $d = f(\sin^2\psi)$ plots are drawn. The d vs ψ plots appear to be linear. The stresses are directly linked to the slopes of these lines.

7.5 Experimental results

The $d=f(\sin^2\psi)$ plots for samples are analyzed and some of them are displayed in Fig. 7-4 and 7-5, in which the corresponding thickness, slope and the stress are indicated. The slopes of the d vs ψ plots, Weight gain, exposure time, thickness of the oxide films and compressive stresses, obtained from all the samples in both mediums, are shown in Tab.7-1. The slopes of these lines change with the corrosion time and the thickness of oxide film, which means that the residual stresses change also. The relationship of the oxide film thickness and the residual stress are shown in Fig. 7-6. Negative values of the stress point to the compressive residual stresses in the oxide layers formed in both mediums. The compressive stresses seem to increase with thickness and they reach the maximum when the thickness is about 2.0μm for 360°C lithiated water and 2.2μm for 400°C steam. Afterwards, they decrease significantly and the stresses of the post-transition samples become steady. Comparing the stress values of the samples corroded in both mediums, the average compressive stresses of the samples in 360°C lithiated water are higher than those in 400°C steam. On the whole, the mean stress in the oxide films of NZ2 alloy is 1.5-3.8GPa and this is similar to what has been reported in earlier experiments [190,191]]. The corrosion transition seems associated with a sudden stress release. In fact, the oxide films formed on NZ2 alloy are textured strongly. The stresses measured on the $(\bar{1}04)$ planes of the m-ZrO_2 are not exact measurements of the average stress tensor components in the oxide layers. However, the stress quantities could be used quantitatively to analyse the relation between the stress state, phase fraction and corrosion kinetics.

7.6 Analysis and discussion

The main aspects that could be discussed are related to the oxide films microstructure and behaviour, the relations between phases, stress changes and oxidation kinetics.

Concerning the relation between the t-ZrO_2 content and corrosion kinetics, it is clear that the average t-ZrO_2 content decreases continuously and smoothly, independent of the

kinetic transitions in both mediums, as the oxidation proceeded. It means that there is no sharp or sudden evolution throughout the bulk of the oxide film. Comparing the corrosion kinetics in both media, the higher t-ZrO_2 content is expected to improve the corrosion resistance as this phase is compact and protective.

With to regard to the relation between the compressive stresses and corrosion kinetics, a few comments could be made: The presented experimental results suggest that the compressive stresses increase at the beginning of oxidation. The compressive stresses in the oxide films exceed the critical value and the stress relaxation occurs when the oxide film thickness reaches a certain value (about 2 μm). This relaxation induces some cracks and porosities in the oxide layers. The cracks and porosities degrade the protective properties of the oxide and accelerate further attack, corresponding to the kinetics transition. The compressive stresses are very low in the samples of post-transition (about 1.9 GPa for the samples in 360°C lithiated water and 1.6 GPa for the samples in 400°C steam). Therefore, the transition seems associated with a sudden stress release. Also, the higher compressive stresses in the samples in 360°C lithiated water are corresponding to the better corrosion resistance.

With respect to the relation between the t-ZrO_2 content and compressive stress, it is found that the higher t-ZrO_2 content is corresponding to the higher compressive stress as a whole. During the corrosion, zirconia is less dense than zirconium and induces high compressive stresses in the oxide due to the high Pilling-Bedworth ratio of the Zr/ZrO_2 system (1.56) [178,191,192]. The compressive stresses in the oxide play an important role for the t-ZrO_2 stability. The t-ZrO_2 is located in compact oxide scale near the metal/oxide interface where the compressive stresses are higher [193]. However, the results in this paper show that there is no complete consistency between the changing regulations of t-ZrO_2 content and the compressive stresses. On the one hand, having in mind the fact that the t-ZrO_2 is not uniformly distributed, and that higher t-ZrO_2 content exist near the metal/oxide interface as shown also in the grazing XRD results. Therefore, local sharp decrease at the metal/oxide interface for thick oxide layers is not excluded. On the other hand, the stresses measured in this study are considered to be the macroscopic compressive stresses. In fact, it is inevitable that there are some areas with high local stress concentration in the oxide films. So it is not enough to only consider the macroscopic compressive stresses for explaining the experiment results. The local stresses may play an important role in stabilizing the t-ZrO_2. Some experimental results showed that the t-ZrO_2 crystallites suffered from large compressive stresses, compared with the m-ZrO_2, which provided clear evidence that the stresses were not uniformly distributed in oxide films and there were some regions with local stress concentration [193]. These local compressive stresses would come from several sources.

Firstly, the decrease of the macroscopic compressive stresses may induce a part of t-ZrO_2 transform to m-ZrO_2. Since this transformation is accompanied by volume dilatation and shear strain and the regions near the transformed crystallites will certainly produce local stress concentration. The t-ZrO_2 crystallites near the transformed ones will undergo the local compressive stresses.

Secondly, during the corrosion, the precipitates containing Fe, Cr, Nb might not be oxidized at the early stage of corrosion because of the different oxidation rates between the matrix and the precipitates. Accordingly the un-oxidized precipitates are first incorporated in the interfacial oxide and oxidized gradually. The oxidation of precipitates will lead to the generation of high local stresses field around the oxidized precipitates. These local compressive stresses may also make some t-ZrO_2 crystallites around the oxidized precipitates more stable.

Thirdly, when zirconia crystallites grow on the surface of metal substrate, the orientation of oxide crystallites must match with the lattice of metal substrate as much as possible. However, it is unlikely that all crystallite orientations are the same to the metal substrate. The high local stress concentrations would be produced in some regions in which the zirconia

crystallites do not match well with the metal substrate. Therefore, a part of t-ZrO_2 may be stabilized by the local stresses.

In addition, solid solution components could have an effect on the stability of the t-ZrO_2. For instance the valence state in the zirconia of the additional elements is expected to be different. This would affect the charged point defect density and, thus, the stability of the different phases of the zirconia. It is also likely that the lower grain size or higher oxygen vacancy concentration at the metal/oxide interface favours the t-ZrO_2. These are still a matter of discussion although it's known to be of high importance.

As discussed above, the corrosion resistance of zirconium alloy is sensitive to many factors, such as microstructure, composition of the oxide films and the stresses. The complexity of the system indicates that several of these factors co-operate to achieve the specific properties and it is impossible to decide which of the factors dominates.

Tab. 7-1 Weight gain, exposure time, thickness of the NZ2 oxide films, the d vs ψ plot slopes and compressive stresses in the oxide films

Corrosion conditions	Exposure time (days)	Weight gain (mg//dm^2)	Oxide films thickness (μm)	d vs ψ plot slope	Stress σ (GPa)
360°C lithiated water	3	12.88	0.9		
	14	18.50	1.2	-0.01318	-2.2
	28	22.85	1.5	-0.01879	-3.1
	42	25.92	1.7	-0.01695	-2.8
	70	30.20	2.0	-0.02284	-3.8
	98	34.53	2.3	-0.01491	-2.5
	126	37.85	2.5	-0.01483	-2.4
	154	58.56	3.9	-0.01113	-1.8
	182	68.08	4.5		
	210	72.90	4.9	-0.01011	-1.7
	238	77.28	5.2	-0.01171	-1.9
	266	90.00	6.0	-0.01093	-1.8
	294	104.15	6.9	-0.01022	-1.7
400°C steam	3	17.00	1.1	-0.01195	-2.0
	14	26.14	1.7	-0.01521	-2.5
	28	32.42	2.2	-0.01740	-2.9
	42	37.47	2.5	-0.01303	-2.1
	70	51.63	3.4		
	98	62.32	4.2	-0.00859	-1.4
	126	72.97	4.9		
	154	82.47	5.5	-0.00981	-1.6
	238	116.14	7.7	-0.00980	-1.6
	266	119.65	8.0	-0.00929	-1.5

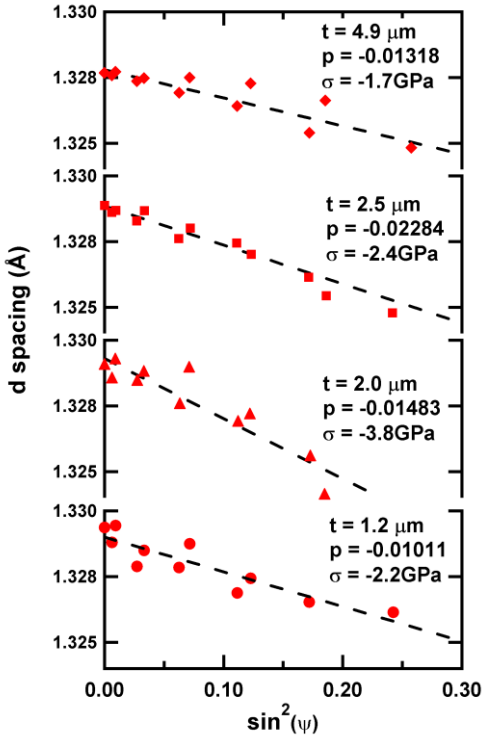

Fig. 7-4 $d=f(\sin^2\psi)$ plots of samples corroded in 360°C lithiated water for 14, 70, 126 and 210 days

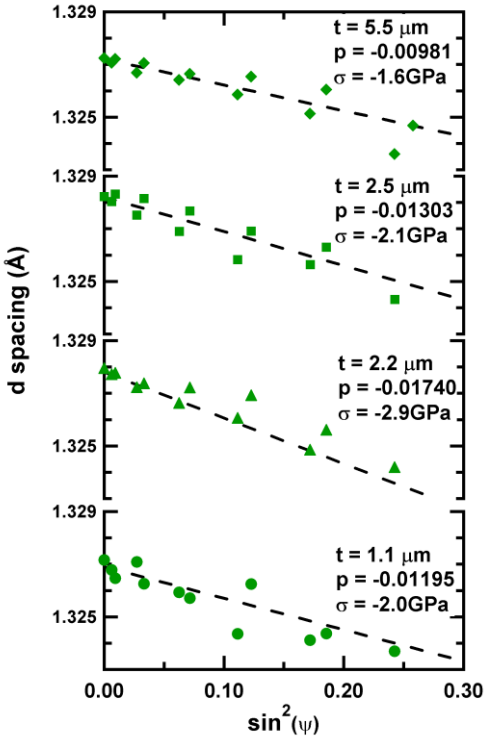

Fig. 7-5 $d=f(\sin^2\psi)$ plots of samples corroded in 400°C steam for 3, 28, 42 and 154 days

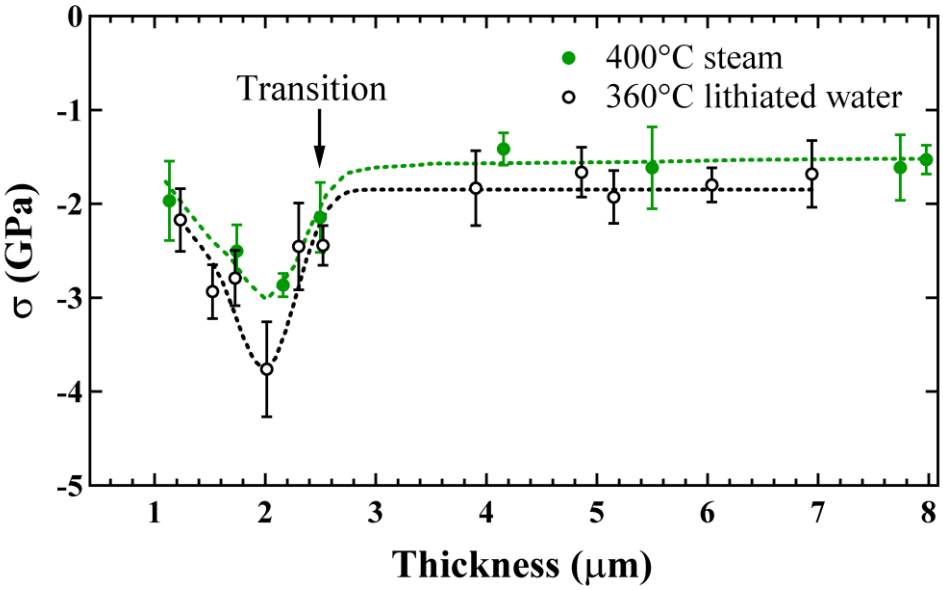

Fig. 7-6 Relationship of the oxide film thickness and compressive stresses in NZ2 oxide films corroded at 360°C lithiated water and at 400°C in steam

7.7 Summary of the chapter

NZ2 alloys have been oxidized in 360°C lithiated water and 400°C steam. The macroscopic stresses and the t-ZrO_2 content in the oxide films have been analyzed by XRD. The following points have been shown:

(1) High compressive stresses are found in the oxide layers. The corrosion transition is associated with a sudden release of the macroscopic compressive stresses in the oxide films.

(2) The samples in 360°C lithiated water present lower corrosion kinetics than that in 400°C steam, with higher t-ZrO_2 content and higher compressive stresses. The t-ZrO_2 is therefore mainly stabilized by the macroscopic compressive stresses. In addition, the local stresses in the oxide films, small grain size and oxygen vacancies play an important role in the t-ZrO_2 stabilization.

Chapter 8

Investigation of corrosion mechanisms of new zirconium alloys containing niobium

Chapter 8 Investigation of corrosion mechanisms of new zirconium alloys containing niobium

8.1 The stabilization mechanisms of t-ZrO_2 and c-ZrO_2

8.1.1 The stabilization mechanisms of oxygen vacancy

Pure zirconia is monoclinic (m-ZrO_2) at room temperature (space group $P2_1/c$) [195,196]; upon increase of the temperature the material transforms to tetragonal (t-ZrO_2) and then to cubic (c-ZrO_2) fluorite structure (space group $P4_2/nmc$ and $Fm3m$, respectively) [197-200]. These phase transitions induce large volume changes and make the pure material unsuitable. The addition of lower-valence oxides like CaO, MgO or Y_2O_3 disfavour the m-ZrO_2, stabilizing more symmetric structures with c-ZrO_2 and t-ZrO_2 [201]. On increasing dopant concentration, the material transforms to a tetragonal (t*-ZrO_2) form, called partially stabilized, and then to a cubic (c*-ZrO_2) form, called fully stabilized. The amount of doping needed for stabilization is quite substantial [202-204], and the electrostatic neutrality of this rather ionic material is maintained by oxygen vacancies.

The simultaneous presence of dopant cations and oxygen vacancies in large concentration means that the local atomic environments in the stabilized material are very different from the corresponding stoichiometric (t-ZrO_2 and c-ZrO_2) phases. Despite the analogy in the sequences m-t-c and m*-t*-c*, there is no clear picture of the microscopic mechanisms of stabilization to parallel our understanding of the pure material: the most relevant issue concerns the respective roles of impurity cations and of oxygen vacancies [205].

Some researchers studied the stabilization mechanism by means of a self-consistent tight-binding model, which was parameterized on the electronic and structural properties of pure zirconia [206,207]. The method was used to calculate the temperature evolution of the free energy surfaces governing the c-t phase transition, which was then described within the Landau theory of phase transformation [208]. These results are the starting point for the present approach to the stabilization mechanism, which is based on the qualitative analogy between isothermal and isoconcentration lines in the high-temperature region of the ZrO_2-Y_2O_3 phase-diagram. At fixed concentration, higher temperature destabilize the tetragonal phases t and t*, favouring the cubic ones c and c*. Similarly, at fixed temperature, higher amounts of impurities stabilize the cubic phases. The analysis of Li and co-workers [209-214] suggests that the dopant cations do not take an active part in the stabilization mechanism, which is dominated by the crystal distortions around oxygen vacancies. So the role of the oxygen vacancies in the stabilization of the c* and t* is studied.

As a preliminary step towards the modelling of stabilized zirconia, the structural and electronic properties of a model crystal structure containing an isolated oxygen vacancy are first addressed[215]. A cubic 96-sites supercell of 95 atoms in the fluorite structure containing one vacant oxygen lattice site is defined as V_1. The vacancy is in the +2 charge state. In the real material, the charge of the $V^{\cdot\cdot}_O$ defect is compensated by the dopant substitutional cations. The cell is electrostatically neutral.

All the atoms are in the centro-symmetric fluorite positions, this is defined as un-relaxed structure, and the crystal structure resulting from the static optimization of the atomic coordinates is defined as relaxed structure.

As the crystal is allowed to relax the Zr atoms nearest neighbour to the vacancy radially shifted outward along [111] directions, and the first shell of anions around the vacancy contract inward along [100] directions. This relaxation pattern is driven by the electrostatics and is shown in Fig. 8-1.

The study of the stabilization mechanism is based of static and dynamic simulations of two 96-site super-cells which were chosen as representative systems. The first one, denoted as

V_1, contains one vacancy. This system corresponds to the stability of the t* phase. Similarly, the second supercell V_4 contains 4 vacancies and corresponds to the stability of the c* phase.

The static minimization of the V_1 super-cell has already been described. Further analysis of the structure reveals that the atomic configuration (Fig. 8-1) is metastable. By perturbing the relaxed configuration, a secondary structural modification further lowers the total energy of the cell, similar to the tetragonal distortion of the oxygen sublattice in pure stoichiometric c-ZrO_2.

According to the energy surface governing the c-t relationship [208], the internal tetragonal distortion of the oxygen sublattice drives the external tetragonal distortion of the unit-cell. As a consequence, the relaxed configuration is expected to further minimize by a non unitary c/a ratio. Indeed, allowing the tetragonality of the cell to adjust, the minimum energy is obtained for c/a=1.02. The corresponding equilibrium structure is shown in Fig. 8-2. The anions and cations are represented with light and dark circles, respectively, and the arrows point to the oxygen column containing the vacancy, which is behind the first visible oxygen ion. The projection on the x-y plane shows the same pattern obtained with the static minimization. The nearest neighbour cations move away from the vacancy and the nearest neighbour anions contract inward. The right panel shows the projection along the x-z plane: the tetragonal distortion of the oxygen sublattice is very clear.

The c* phase was modelled by distributing four vacancies in the super-cell. In this configuration, the four vacancies were aligned along the [111] direction to form a vacancy cluster. The static relaxation was started with all the atoms in the fluoritic centro-symmetric positions. In this case, only one structural modification was observed. The system evolved towards the atomic configuration shown in Fig. 8-3. The local distortions around the vacancies lock the c* crystal in a distorted configuration, suppressing the tetragonal distortion of the oxygen sublattice. The local atomic environment is very different from that of the fluorite structure: 14 cations out of 32 are 7-fold coordinated and the majority of the oxygen ions are not in centro-symmetric positions. The minimum energy is obtained for a perfect cubic super-cell.

When the results described in the previous section are considered in the context of the c-t phase transition in pure zirconia [207], they also provide insight on how the structural distortions around the oxygen vacancies affect the relative stability of the tetragonal and cubic phases. In conclusion, partially and fully stabilized zirconias were modelled by introducing, respectively, one and four vacancies in a 96-site cubic super-cell (V_1 and V_4, respectively).

The analysis of the V_1 and V_4 equilibrium crystal structures suggests a possible explanation of the stabilization mechanism. When the concentration of vacancies is low, as in the V_1 super-cell, a relatively large volume of crystal is le left in the fluorite structure, and it undergoes the tetragonal distortion just as the stoichiometric material in the c-phase would. Because this distortion involves the coordinated motion of all the oxygen atoms, also the atoms neighbouring the defects are dragged along the tetragonal distortion of the oxygen sublattice.

When the concentration of defects is high, as in the V_4 super-cell, there is virtually no undistorted cubic region in the statically relaxed super-cell, every oxygen atom is either itself a neighbour of a vacant site, or at least four of its six neighbouring oxygen atoms are. Thus there is virtually no region in which the local atomic environment is close to fluorite, which could undergo the tetragonal distortion, and the radial distortions around the vacancies dominate the finite-temperature equilibrium configuration. The resulting atomic structure is cubic only by averaging over a relatively large number of atoms, but the shot-range atomic structure does not have cubic symmetry.

These results show that the stabilization of the t* and c* structures may be achieved in theory by doping zirconia crystal with oxygen vacancies only, and support the idea that the

electronic and structural properties of stabilized zirconia are controlled by the structural disorder around the oxygen vacancies, rather than by the substitutional dopant cations.

In this paper, the t-ZrO_2 content in the oxide films of zirconium alloys is high at the beginning of corrosion. This could be explained by V_1 super-cell structure stabilization. That's to say, the vacancy concentration caused by the alloying element oxidation is low, which is good to t-ZrO_2 stabilization. With the corrosion process, Nb takes part in the oxidation and forms Nb_2O_3, which increases the vacancy concentration. When the vacancies array arrange along certain direction, V_4 super-cell structure is formed. So t-ZrO_2 transforms to m-ZrO_2 to minimize the system energy. Subsequently, the cracks are produced by the large volume expand of Nb oxidation, thus the corrosion transition

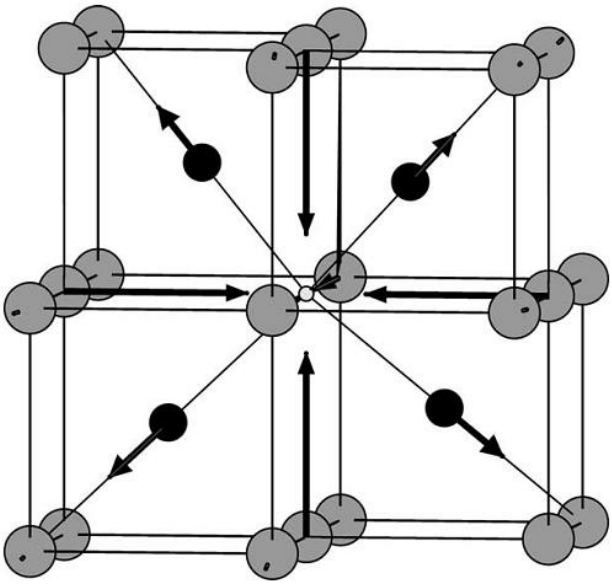

Fig. 8-1 Crystal relaxation of the atoms neighbouring an isolated vacancy in a fluorite lattice. Key: Zr black, O dark grey, vacancy light grey

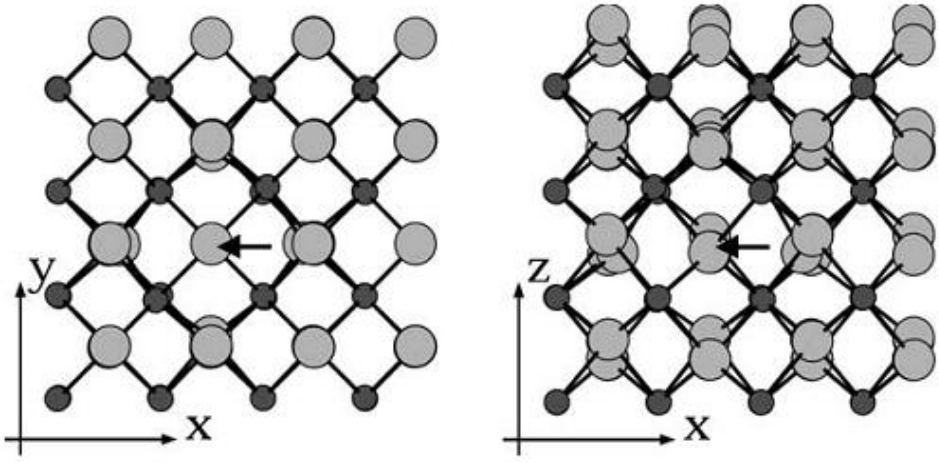

Fig. 8-2. Equilibrium crystal structure of the V_1 supercell. The arrows point to the oxygen columns containing the vacancies

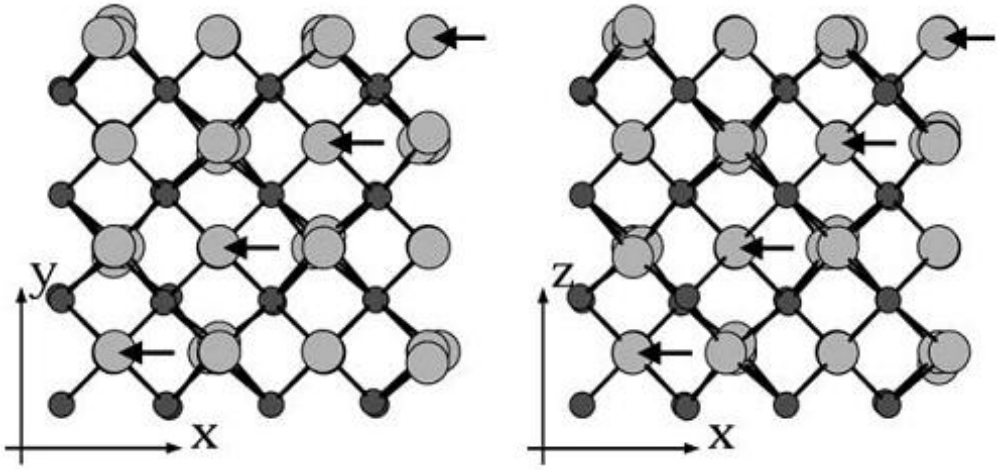

Fig. 8-3 Equilibrium crystal structure of the V_4 supercell. The arrows point to the oxygen columns containing the vacancies.

The amount of c-ZrO_2 in post-transition oxide films increases until Nb is oxidized to Nb_2O_5, and at this time c-ZrO_2 will transform to m-ZrO_2.

8.1.2 The stabilization mechanism of compressive stresses

According to the compressive stress-temperature diagram of ZrO_2, t- ZrO_2 can exist stably under 3000MPa compressive stresses. The P.B ratio of Zr/ZrO_2 system is 1.56. There are high compressive stresses caused by the volume expander in the oxide film when Zr is oxidized to ZrO_2. The compressive stresses make t- ZrO_2 stable. With the oxidation process, the oxide film/metal interface advances, and the t-ZrO_2 formed previously transforms to m-ZrO_2, which leads to the decreasing of t-ZrO_2 away from the interface. The high compressive stresses remain in the new oxide film and the compressive stresses release in the oxide formed previously.

Many researchers tested the stress and the distribution in the oxide film by different methods [219-221]. They found there were high compressive stresses and there was a stress gradient in the oxide films. The compressive stresses at oxide/metal interface are higher than those at the surface.

In this study, the average residual stresses in the oxide films were tested by XRD method. The average compressive residual stress in the NZ2 alloy oxide film is 1.5 ~ 3.8 GPa, and the higher the compressive stresses are, the higher the t-ZrO_2 content is. The high compressive stresses stabilize t-ZrO_2.

8.2 The stress release mechanisms in the oxide films

The early stress study about Zr-2 alloy oxide film indicated that the break mechanism of oxide film was related to the mechanics destroy of the oxide films [222]. At the early stage of the corrosion, the compressive stresses in the oxide film are high, subsequently the oxide film breaks. And the stresses are the highest at the break point. However, the compressive stresses are much lower in the oxide films of zirconium crystal and the break process is not observed.

There are many reasons of the stress existence [223,224]. The most important reason is the volume increase with the oxidation of metal surface. The oxide growth is a process of oxygen diffusing into the interior, thus the oxide/metal is restricted while the new oxide layer forms. Furthermore the stress release happens either in the metal (the plastic deformation of metal matrix), or in the oxide films (the plastic deformation of oxide), or in both of metal and oxide.

The plastic deformation rate of the oxide depends on its growth rate. At the early stage of the oxide growth, the deformation rate is large. The plastic deformation of the oxide makes the internal stresses release. The initial growth rate of the oxide is high, so the local diffusing rate is high enough to make stresses release by the plastic deformation. When the oxide thickness increases, the diffusing rate decreases to a certain degree, thus the release rate is too slow and the oxide film breaks. At this moment, the cracks appear in the oxide film and the corrosion transition happens, the internal average stress also reduces to a steady value.

In this study, SEM images of NZ2 alloy oxide film show that there are cracks in the oxide film of post-transition sample, and the stress measurement results show that the compressive stress reaches maximum at about 2μm oxide thickness, and then the corrosion transition happens. Furthermore the compressive stresses in the post-transition samples are low and remain steady. So we think the compressive stresses release by the plastic deformation in this study.

8.3 The corrosion mechanisms of new zirconium alloys

Many researchers studied the corrosion resistance of zirconium alloys and the corrosion mechanism. Investigation on the corrosion mechanism is to explain the corrosion process, corrosion transition phenomenon and to establish the corrosion kinetics regulation by study the oxide crystal structure, the defect evolvement and function during corrosion. Zhou B.X. et al [225,226] studied the effects of water chemical and alloying composition on the crystal structure and growth of the oxide film, and put forward some new ideas for the corrosion mechanism.

About Zr-4 alloy corrosion mechanism, some people approve the hypothesis of the oxygen vacancy reaction [227,228]. However other people support the hypothesis of the phase transformation induced by stresses [229,230]. Every hypothesis emphasizes the importance of t-ZrO_2. The t-ZrO_2 content changes with corrosion kinetics. It transforms to m-ZrO_2, which is used to explain why the oxide film loses protective function. Some experimental results show that the t-ZrO_2 content at the oxide/metal is high (30 ~ 40%) [231].

In this paper, the matrix microstructure studies show that small and well-distributed precipitates containing Nb are good to improve the corrosion resistance because the precipitates containing Nb make the Nb content in the matrix less than the equilibrium solid limit. The results of oxide crystal structure show that t-ZrO_2 content decreases and m-ZrO_2 content increases with the corrosion process, and the c-ZrO_2 appears before corrosion transition happens. There are cracks in the post-transition oxide film. In addition, the stress measurement results suggest that the compressive stresses increase at the beginning of oxidation. The compressive stresses in the oxide films exceed the critical value and the stress relaxation occurs when the oxide film thickness reaches a certain value (about 2 μm). This relaxation induces some cracks and porosities in the oxide layers. The cracks and porosities degrade the protective properties of the oxide and accelerate further attack, corresponding to the kinetics transition. The compressive stresses are very low in the samples of post-transition (about 1.9 GPa for the samples in 360°C lithiated water and 1.6 GPa for the samples in 400°C steam). Therefore, the transition seems associated with a sudden stress release. Also, the higher compressive stresses in the samples are corresponding to the better corrosion resistance.

From these results, we try to propose a mechanism for the oxidation of new zirconium alloys. The first oxide layers that are formed are going to create a high level stress due to the difference in volume between the oxide and the metal. This will give compressive stresses in the oxide and tensile stresses in the underlying metal. Also the alloying elements in the matrix take part in the oxidation. The local compressive stresses and oxygen vacancies produced by the oxidation have an effect on the t-ZrO_2 stabilization. In addition, the precipitates play a role

in the generation of additional stresses in the oxide layer. When the matrix oxidation occurs, the precipitates are not oxidized at the same time as the surrounding metal. They are incorporated in the oxide as intermetallic precipitates. Starting at some distance from the metal/oxide interface, they are going to be progressively oxidized. The zirconium that has the highest reactivity towards oxygen is oxidized first. Because Fe, Cr, Nb, which make up the precipitate, have low solubility in ZrO_2, only small amounts are incorporated into the ZrO_2. This makes it possible to stabilize the tetragonal phase by forming vacancies in their crystal lattice. The remaining metal atoms are rejected towards the precipitates/oxide interface where they will segregate.

When the zirconium in the precipitate is oxidized to form ZrO_2, stresses are caused by the volume differences between the initial precipitate and the newly-formed ZrO_2 (Fig. 8-4). The differential oxidation of the precipitates inside the oxide layers provides a new source of stresses that can keep the surrounding t-ZrO_2 stable. The t-ZrO_2 is stabilized by the compressive stresses and vacancies.

Subsequently, almost at the end of oxidation for some of the precipitates, Nb in the precipitate is oxidized, which makes the vacancy concentration is high enough to form the vacancy cluster along a certain direction, t-ZrO_2 will transform first to c-ZrO_2 to minimize the system energy[229]. And the large volume expander caused by the Nb oxidation accelerates the crack formation and makes the compressive stresses release. Thus kinetics transition happens, which corresponds to the end of oxidation of precipitates. At this time the oxygen vacancy concentration in the oxide film is the highest and the precipitates would no longer locally produce additional stresses in the oxide. This can be used to explain the phenomenon of the c-ZrO_2 content increasing after corrosion transition. The c-ZrO_2 nucleates during the transformation of t-ZrO_2 to m-ZrO_2. With the corrosion process, the oxide/metal interface advances. There are high compressive stresses in the new-formed oxide layer and the compressive stresses in previous-formed layer are released. So the t-ZrO_2 content decreases. The c-ZrO_2 is stabilized by the vacancies produced by the Nb oxidation.

As a whole, there is a decrease in the overall t-ZrO_2 volume fraction in the oxide, and a stress relaxation in the oxide thickness corresponds to the kinetics transition. During kinetics transition, in the outside region of the oxide, some of t-ZrO_2 does not undergo the phase transformation to m-ZrO_2. The t-ZrO_2 probably results from the zirconium oxidation that makes up the precipitates and that is chemically stabilized by the presence of Fe, Cr, Nb in its crystal lattice. This is confirmed by the Raman spectroscopy analyses and the grazing XRD analyses, namely, at the external layers, there is only a low concentration of t-ZrO_2 stabilized by the additive elements in the precipitates. This is consistent with the results of Cox [228]. So the t-ZrO_2 mainly is stabilized by the compressive stresses, however, the c-ZrO_2 mainly is stabilized by the vacancies caused by the Nb oxidation.

In addition, the precipitates that are too small will be rapidly oxidized, decreasing the pre-transition period. On the other hand, large precipitates take more time to oxidize, but are less effective in stabilizing t--ZrO_2. A compromise in precipitate size will optimize the corrosion resistance of the zirconium alloys.

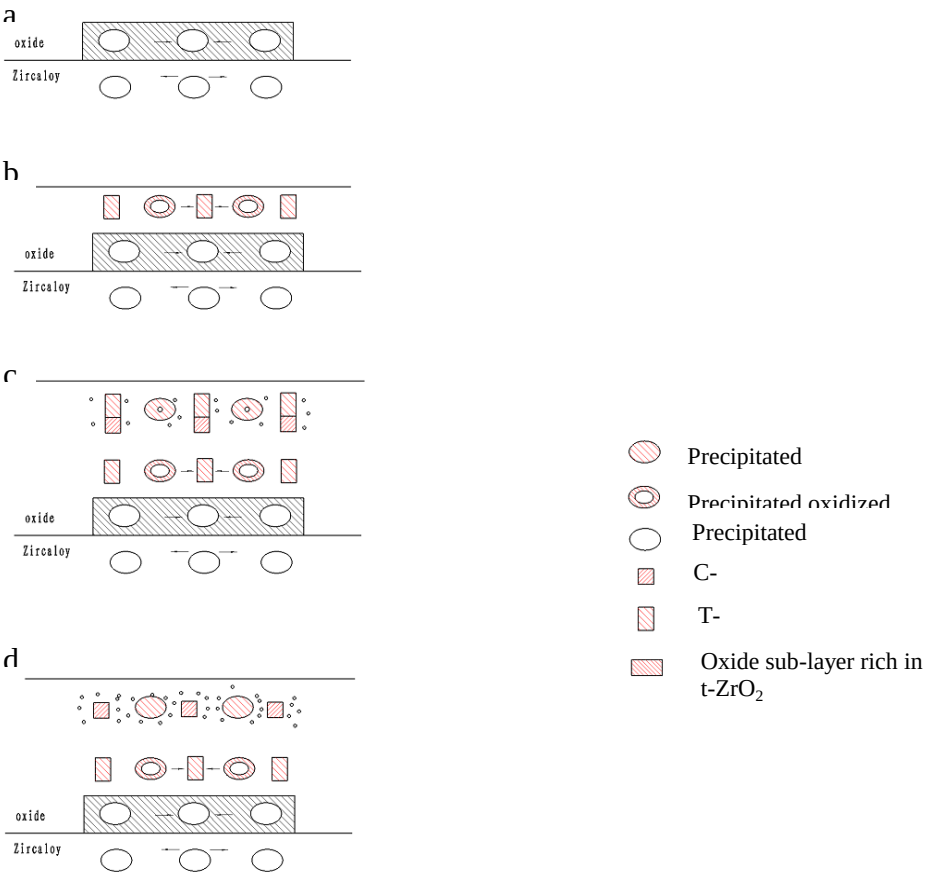

Fig. 8-4 Corrosion mechanisms of new Zircaloys

Chapter 9

Main Conclusions

Chapter 9 Main Conclusions

In this work, the corrosion behaviours of NZ2 and NZ8 alloys were investigated after testing in superheated steam at 400°C/10.3 MPa and in 70 ppm LiOH aqueous solution at 360°C/18.6 MPa. The impacts of alloy elements and the second precipitate particles on corrosion behaviour during corrosion tests were discussed. The relations of the structure change, internal stress in the oxide films and corrosion resistance were studied. The corrosion mechanism of new zirconium alloy was built. The main experimental results and conclusions are as follows:

1. The corrosion resistance of new zirconium alloys containing Nb is much better than that of Zr-4 alloy in 360°C/18.6 MPa LiOH aqueous solution, that's to say, the addition of Nb is benefit to improve the corrosion resistance of zirconium alloys. The corrosion resistance of NZ8 alloy with high Nb addition is worse than that of NZ2 alloy with low Nb in both mediums, which depends on the second precipitate particles and the alloy element content in the matrix. Also, the corresponding oxide film thicknesses of both alloys are identical (2~3 μm) when the transitions happen. In addion, smaller and dispersion distributing precipitates can shorten the pre-transition time of NZ2 alloy in 400°C/10.3 MPa steam, but improve the post-transition corrosion resistance.

2. The corrosion resistance of new zirconium alloys is correlated to the Nb content in the matrix and the degree of supersaturation. The Nb content in NZ2 matrix is lower than the equilibrium solid solubility, which is benefit to improve the corrosion resistance of NZ2 alloy. The oxidation of supersaturated Nb in NZ8 matrix makes the oxide film volum increase seriously, even the oxide film breaks, which promotes the transformation from t-ZrO_2 to m-ZrO_2, thus the corrosion rate increases.

3. The corrosion resistance of zirconium alloy is related to the characteristic, the quantity and the size of the precipitates. The oxidation rate of the β-Zr precipitates in NZ8 alloy is higher than that of the precipitates containing Nb in NZ2 alloy, and the β-Zr precipitates accelerate the transformation from t-ZrO_2 to m- ZrO_2. So the t-ZrO_2 content of NZ8 alloy oxide film is lower than that of NZ2 alloy, and post-transition corrosion rate of NZ8 alloy is also much higher. In addition, the volume fraction of the precipitates is another influencing factor of corrosion resistance. After a large quantity of precipitates in NZ8 alloy are oxidized, the additional compressive stresses are generated. Thus the volume of oxide film increases and the cracks are formed, which accelerates the corrosion rate. However, the precipitates of NZ2 alloy are benefit to improve the corrosion resistance.

4. The oxide films of NZ2 and NZ8 alloys are composed of m-ZrO_2 mainly, including a kind of distorted t-ZrO_2. With the corrosion, the average t-ZrO_2 content in the oxide film decreases and the t-ZrO_2 transforms to t-ZrO_2. Also the t-ZrO_2 content in the oxide film decreases from oxide/metal to the oxide surface. When the oxide thickness reaches to 2 μm (pre-transition), the c-ZrO_2 appears, and the c-ZrO_2 content increases obviously after the transition happens. So it's considered that the c-ZrO_2 is the transition phase of the transformation from t-ZrO_2 to m-ZrO_2. There are two kinds of phase transformations during corrosion: t-ZrO_2→m-ZrO_2 and t-ZrO_2→c-ZrO_2 →m-ZrO_2. The t-ZrO_2 is stabilized by the compressive stresses and vacancies caused by the alloying element oxidation, and the c-ZrO_2 is stabilized by the vacancies. The t-ZrO_2 transform rate is a determination factor of corrosion resistance. The faster t-ZrO_2 transform rate is, the lower t-ZrO_2 content is, the higher corrosion rate is. There is no sudden decrease of t-ZrO_2 content during corrosion. The local compressive stresses caused by the oxidation of the precipitates could stabilize the t-ZrO_2.

5. The high compressive stresses exist in the oxide films of NZ2 alloy. The sudden release of the compressive stresses in the oxide films is related to corrosion transition. The compressive stresses and the t-ZrO_2 content in the oxide film of NZ2 alloy corroded in 360^{o}C Li water are higher than those in 400^{o}C steam. Higher t-ZrO_2 content and compressive stresses in the oxide films can improve the corrosion resistance of zirconium. The macroscopic compressive stresses in the oxide films have an important effect on the t-ZrO_2 stabilization. In addition, the local stresses in the oxide films also stabilize the t-ZrO_2.

References

[1] 杨文斗主编，反应堆材料学[M]，北京: 原子能出版社，（2006).

[2] 周邦新，改善锆合金耐腐蚀性能的概述[J].金属热处理学报，(1997)18(3): 8-15.

[3] (2006) 年中国核电行业分析及投资咨询报告.

[4]能源发展战略及”十一五”的重点咨询研究报告.2004.12，中国工程院能源与矿业工程学部

[5] 中国电力百科全书: 核能及新能源发电卷[M].北京: 中国电力出版 (1995).

[6] Keams J.J., Terminal solubility and partitioning of hydrogen in the alpha phase of zirconium，Zircaloy-2 and Zircaloy-4[J].J. Nucl. Mater.（1967）22: 292-303.

[7]卡恩，R.W.,哈森，P.，克雷默，E.J.主编，周邦新等译.核应用中的锆合金[M]，在‘材料科学与技术丛书一核材料(10B卷)中. 北京: 科学出版社（1999）pp.1-5.

[8] Perryman E.C.W., Pickering Pressure Tube Cracking Experience[J]. Nucl. Energy (1978) 17: 95.

[9] Simpson，C.J. and Ells，C.E.，Delayed Hydrogen Embrittlement in Zr-2.5Nb%[J]. J.Nucl.Mat. (1974) 52: 289.

[10]周邦新，郑斯奎，汪顺新，Zr2合金中应力和应变诱发氢化锆析出过程的电子显微镜原位研究[J].金属学报 (1989）25: A190-195.

[11]周邦新,姚美意等，氧化-氢化引起的锆合金焊接件开裂问题[J]. 核动力工程(2006）27(l): 34-36.

[12] Lustman B. and Kerze F[M]. The metallurgy of Zr, McGraw Hill, N.Y. (1955).

[13] Holt R. A. and Causey A. R., The effects of intergranular constraints in irradiation growth of Zry2 at 320^{o}C [J]. J. Nucl. Mater. 150 (1987) 306-318.

[14] R.W卡恩，P.哈森，E.J.克雷默主编，核应用中的锆合金[M]. 材料科学与技术丛书，核材料，10B卷，科学出版社（1999）1-45.

[15]陈鹤鸣，马春来，白新德主编，核反应堆材料腐蚀及其防护[M].北京:

原子能出版社 (1984) pp.188-235.

[16] 杨文斗主编, 反应堆材料学[M]. 北京: 原子能出版社 (2006) 259-289.

[17] Charquet D., Hahn R., Ortlieb E., Gros J. P. and Wadier J. F.,"Solubility limits and formation of intermetallic precipitates in Zr-Sn-Fe-Cr alloys"[C]. Zirconium in the Nuclear Industry: 8th Int. Symp., ASTM-STP-1023, (Van Swam L.F. P., Eucken C.M., Eds.), American Society for Testing and Materials, W. Conshohocken, PA. (1989) 405-422.

[18] Charquet D. and Alheritiere E., Second phase particles and matrix properties on Zircaloys [R]. Proc. Workshop on second phase particles in Zircaloys, Erlangen FRG, Kern Tech. Gesell. (1985) 5-11.

[19] Shebaldov, P.V., Perregud, M.M., et al., E110 alloy cladding tube properties and their interrelation with alloy structure-phase condition and impurity content [C]. Zirconium in Nuclear Industry: 12th Int. Symp., ASTM STP 1354 (2000) pp.545-559.

[20] Mardon, J. P., Charquet, D., and Senevat, J., Influence of composition and fabrication process on out-of-pile and in-pile properties of M5 alloy [C]. Zirconium in the Nuclear Industry: 12th Int. Symp., ASTM STP 1354 (2000) pp. 505-524.

[21] Warr, B.D., Van Der Heidi, P. A. W., and Maguire, M. A., Oxide characteristics and corrosion and hydrogen uptake in Zr-2.5Nb CANDU pressure tubes [C]. Zirconium in the Nuclear Industry: 11th Int. Symp., ASTM STP 1295 (1996) pp.265-291.

[22] Chakravartty J.K. et al, Characterization of hot deformation behavior of Zr-2.5Nb-0.5Cu using processing maps [J]. J. Nucl. Mater., 218 (1995) 247.

[23] Williams C. D. and Gilbert R. W., Tempered structure of a Zr-2.5%Nb alloy [J]. J. Nucl. Mater. 18 (1966) 161-166.

[24] Cheadle B. A. and Aldridge S. A., Transformation and age hardening behavior of Zr-19%Nb [J]. J. Nucl. Mater. 47 (1973) 255-258.

[25] Choo, K. N., Kang, Y. H., Pyun, S. I., et al. Effect of composition and heat treatment on the microstructure and corrosion behavior of Zr-Nb alloys [J]. J. Nucl. Mater. (1994) 209: 226-235.

[26] Sabol, G. P., Kilp, G. R., Balfour, M. G., et al., Development of a cladding alloy for higher burnup [C]. Zirconium in the Nuclear Industry: 8th Int. Symp., ASTM STP 1023 (1989) pp. 227-244.

[27] Sabol, G. P., Comstock, R. J., Weiner, R. A. et al, In-reactor corrosion performance of ZIRLO^{TM} and Zircaloy-4 [C]. Zirconium in the Nuclear Industry: 10th Int. Symp., ASTM STP 1245 (1994) pp. 724-744.

[28] Comstock, R. J., Schoenberger, G., and Sable, G. P., Influence of processing variables and alloy chemistry on the corrosion behavior of ZIRLO nuclear fuel cladding [C]. Zirconium in the Nuclear Industry: 11th Int. Symp., ASTM STP 1295 (1996) 710-725.

[29] Sabol, G. P., ZIRLO^{TM}-An alloy development success [C]. Zirconium in the Nuclear Industry: 14th Int. Symp., ASTM STP 1467 (2004) pp. 3-24.

[30] Nikulina, A. V., Markelov, V. A., Peregud, M. M., et al., Zirconium alloy E635 as a material for fuel rod cladding and other components of VVER and RBMK cores [C]. Zirconium in the nuclear industry: 11th Int. Symp., ASTM STP 1295, 1996, pp. 785-804.

[31] 鸟语正男等, 加压水轻水水炉(PWR)燃料 [J]. 原子力工业 (1993) 39 (5): 40.

[32] Y. H. Jeong et al, Development of high corrosion resistance zirconium alloys [C]. Technical Meeting on Behavior of High Corrosion Resistance Zr-based Alloys, 24-27 (2005) The National Library, Buenos Aires, Argentina.

[33] 刘建章, 国内核动力堆用锆合金的研究动向 [J]. 稀有金属材料与工程 (1990) 6: 32-35.

[34] 郑杰, 牛惠玲等, Zr-4合金工艺改进的研究 [J]. 稀有金属 (1995) 19 (4): 260-263.

[35] 李佩志, 邝用庚等, Nb含量对锆合金腐蚀性能的影响 [C].“96中国材料研讨会, 生物及环境材料, Ⅲ-2”, 北京: 化学工业出版社 (1997) pp. 179-182.

[36]周邦新,郑斯奎,汪顺新,真空电子束焊接对锆2合金熔区中成分、组织及腐蚀性能的影响 [J]. 核科学与工程 (1988) 8 (2): 130-137.

[37] 周邦新, 赵文金等, 新锆合金的研究 [C]. “96中国材料研讨会, 生物及环境材料, Ⅲ-2”, 北京: 化学工业出版社 (1997) pp. 183-186.

[38] 周邦新, Zr-Sn-Nb系合金的显微组织研究[C].“96中国材料研讨会, 生物及环境材料, Ⅲ-2”, 北京: 化学工业出版社 (1997) pp. 187-191.

[39] 周邦新, 李强, 黄强等, 水化学对锆合金耐腐蚀性能影响的研究 [J]. 核动力工程 (2000) 21 (5): 439-447.

[40] 周邦新, 赵文金, 蒋有荣等, Zr-4合金元素的表面偏聚 [J]. 核动力工程 (1998) 19 (6): 506-508.

[41] 赵文金, 苗志, 蒋宏曼等, Zr-Sn-Nb合金的腐蚀行为研究 [J]. 中国腐蚀与防护学报 (2002) 22 (2): 124-128.

[42] 李佩志, 李中奎等, 合金元素对Zr.-Nb合金耐蚀性能的影响 [J]. 稀有金属材料与工程 (1998) 27 (6): 356-359.

[43]李中奎,刘建章等, 新锆合金在两种不同介质中的耐蚀性能 [J]. 稀有金属材料与工程 (1999, 28 (2)) 101-104.

[44] 朱梅生, 刘建章等, 8#新锆合金的组织与耐蚀性能的研究 [J]. 稀有金属材料与工程 (1996) 25 (4): 34-38.

[45] 邝用庚, Zr-Nb系合金耐蚀性能研究 [J]. 稀有金属材料与工程 (1995) 24 (3): 41-45.

[46]刘文庆,合金元素及水化学对锆合金耐腐蚀性能影响的研究[D].上海大学博士学位论文 (2002).

[47]李中奎,刘建章等,合金元素对Zr-Sn-Fe-Cr-Nb合金性能的影响[J].

稀有金属材料与工程 (1996) 25 (5): 43-48.

[48]姚美意,合金成分及热处理对锆合金腐蚀和吸氢行为影响的研究 [D].

上海大学博士学位论文 (2007).

[49] Broy Y., Garzarolli F., Seibold A., and Van Swam L.F., Influence of transition elements Fe, Cr, and V on long-time corrosion in PWRs[C]. Zirconium in the Nuclear Industry: 12th Int. Symp., ASTM STP 1354 (2000) 609-622.

[50] Sabol G., Comstock R.J., and Nayak U.P., Effect of dilute alloy additions of Mo, Nb, V on zirconium corrosion[C]. Zirconium in the Nuclear Industry: 12th Int. Symp., ASTM STP 1354 (2000) 524-544.

[51] Hong, H. S., Moon, J. S., et al., Investigation on the oxidation characteristics of copper-added modified Zircaloy-4 alloys in pressurized water at 360°C [J]. J. Nucl. Mater. (2001) 297: 113-119

[52] Eueken, C. M., Finden, P. T., et al., Influence of chemical composition on uniform corrosion of zirconium-base alloys in autoelave tests [C]. Zirconium in the Nuclear Industry: 8th Int. Symp., ASTM STP 1023 (1989) pp. 113-127.

[53] Garzarolli F., Broy Y. and Busch R.A., Comparison of the long-time corrosion behaviour of certain Zr alloys in PWR, BWR, and laboratory [C]. Zirconium in the nuclear industry: 11th Int. Symp., ASTM STP 1295 (1996) pp. 850-864.

[54] Graham R.A., Tosdale J.P., and Finden P.T., Influence of chemical composition and manufacturing variables on autoclave corrosion of the Zircaloys [C]. Zirconium in the Nuclear Industry: 8th Int. Symp., ASTM STP 1023 (1989) pp. 334-345.

[55] Harada M., Kim Para M. and Abe K., Effect of alloying elements on uniform corrosion resistance of zirconium-based alloys in 360°C water and 400°C steam [C]. Zirconium in the Nuclear Industry: 9th Int. Symp., ASTM STP 1132 (1991) pp.368-391.

[56] Isobe T., and Matsuo Y., Development of highly corrosion resistant zirconium-based alloys [C]. Zirconium in the Nuclear Industry: 9th Int. Symp., ASTM STP 1132 (1991) pp. 346-367.

[57] Isobe T., Matsuo Y. and Mae Y., Micro-characterization of corrosion resistant zirconium-based alloys [C]. Zirconium in the Nuclear Industry: 10th Int. Symp., ASTM STP 1245 (1994) pp.437-449.

[58] Park J. Y., Choi B. K. et al., Corrosion behaviour of Zr alloys with a high Nb content [J]. J. Nucl. Mater. (2005) 340: 237-246.

[59] Yueh H. K., Kesterson R. L., Comstock R. J., et al., Improved ZIRLO™ cladding performance through chemistry and process modifications[C]. Zirconium in the Nuclear Industry: 14th Int. Symp., ASTM STP 1467 (2004) pp.330-346.

[60] Steinberg E., Weidinger H. G., and Schaa A., Analytical approach and experimental verification to describe the influence of cold work and heat treatment on the mechanical properties of Zircaloy cladding tubes[C]. Zirconium in the Nuclear Industry: 6th Int. Symp., ASTM STP 824 (1984) pp. 106-122.

[61] Cox B., Some thoughts on the mechanisms of in-reactor corrosion of zirconium alloys [J]. J. Nucl. Mat. (2005) 336: 331-368.

[62] Garzarolli G., Steinberg E. and Weiginger H. G., Microstructure and corrosion studies for PWR and BWR Zircaloy cladding [C]. Zirconium in the Nuclear Industry: 8th Int. Symp., ASTM STP 1023 (1989) pp. 202-212.

[63] Thorvaldsson T., Andersson T. et al., Corrosion between 400°C steam corrosion behaviour, heat treatment and microstructure of Zircaloy-4 tubing [C]. Zirconium in the Nuclear Industry: 8th Int. Symp., ASTM STP 1023 (1989) pp.128-140.

[64] Franklin D. G. and Lang P. M., Zirconium-alloy corrosion: a review based on an

International atomic energy agency (IAEA) meeting [C]. Zirconium in the Nuclear Industry: 9th Int. Symp., ASTM STP 1132 (1991) pp. 3-32.

[65] Foster P., Dougherty J., Burke M.G. et al., Influence of final recrystallization heat treatment on Zircaloy-4 strip corrosion [J]. J. Nucl. Mat. (1990) 173 (2): 164-178.

[66] Wadman B. and Andrén H.Q., Direct measurement of matrix composition in Zircaloy-4 by atom probe microanalysis [C]. Zirconium in the Nuclear Industry: 8th Int. Symp., ASTM STP 1023 (1989) pp. 423-434.

[67] Garzarolli F., Schumann R. and Steinberg E., Corrosion optimized zircaloy for boiling water reactor (BWR) fuel elements [C]. Zirconium in the Nuclear Industry: 10th Int. Symp., ASTM STP 1245 (1994) pp. 709-723.

[68] Zhou, B., Zhao W., Miao Z. et al., The effect of heat treatment on the corrosion behaviour of Zircaloy-4 [R]. China Nuclear Seience and Technology Report, CNIC-01074, SINRE-0066, China Nuclear Information Centre Atomic Energy Press (1996).

[69] Li C., Zhou B. X. et al., Determination of Fe and Cr content in α-Zr solid solution of Zircaloy-4 with different heat-treated states[J]. J. Nucl. Mater. (2002) 134-138.

[70] Kim J.M., Jeong Y.H. and Jung Y.H., Correlation of heat treatment and corrosion behaviour of Zr-Nb-Sn-Fe-Cu alloys [J]. J. Mater. Proc. Tech. (2000) 104: 145-149.

[71] Sabol G.P., Comstock R.J. and Nayak U.P., Effect of dilute alloy additions of Molybdenum, niobium, and vanadium on zirconium corrosion [C]. Zirconium in the Nuclear Industry: 12th Int. Symp., ASTM STP 1354 (2000) pp. 525-544.

[72]刘文庆,李强,周邦新等,热处理制度对N18新合金耐腐蚀性能的影响[J].核动力工程

(2005)26 (3): 249-253.

[73] Jeong Y.H., Lee K.O. and Kim H.G, Correlation between microstructure and corrosion behaviour of Zr-Nb binary [J]. J. Nucl. Mater (2002)302: 9-19.

[74] Jeong Y.H., Kim H.G. and Kim T.H., Effect of β-phase, Precipitate and Nb-concentration in matrix on corrosion and oxide characteristics of Zr1-xNbx alloys [J]. J. Nucl. Mat. (2003)317: l-12.

[75] Jeong Y.H., Kim H.G and Kim D.J., Influence of Nb concent ration in the α-matrix on the corrosion behaviour of Zr1-xNbx binary alloys [J]. J. Nucl. Mater. (2003), 323: 72-80.

[76] Kim H.G, Jeong Y.H. and Kim T.H., Effect of isothermal annealing on the corrosion behaviour of Zr1-xNbx alloys [J]. J. Nucl. Mater. (2004)326: 125-131.

[77] Li Z.K., Zhou L., Zhao W.J. et al., Effect of intermediate annealing on out-of pile corrosion resistance of zirconium-based alloy [J]. 稀有金属材料与工程 (2001)30 (增刊l): 52-54.

[78]刘文庆，李强，周邦新等，显微组织对ZIRLO锆合金耐腐蚀性的影响[J].核动力工程 (2003)24 (l): 33-36.

[79] Komarek K.L. and Silver M., Thermodynamic properties of zirconium-oxygen, titanium-oxygen and hafnium-oxygen alloys [R]. Thermodynamics of nuclear materials, Proc. Int. Conf., IAEA, Vienna (1962) 749-774.

[80] Zhang C-S, Flinn B.J., Mitchell I.V and Norton P. R., The intial oxidation of Zr (0001), 0 to 0.5 monolayers [J]. Surf. Sci., 245 (1991) 373-379.

[81] Tapping R.L., X-ray photoelectron and ultraviolet photoelectron studies of the oxidation and hydriding of zirconium [J]. J. Nucl. Mater., 107 (1982) 151-158.

[82] Amsel G., David D., Beranger G, Boisot P., De Gelas B. and Lacombe P., Analyse à l'aide d'une méthode nucléaire des impuretés introduites dans les métaux par leurs préparations d'état de surface: application au zirconium [J]. J. Nucl. Mater., 29 (1969) l44-153.

[83] Cox B., Oxidation of zirconium and its alloys [R]. Ady. in Corr. Sci. and Tech., Vol. 5, (Fontana M.G, Staehle R.W., Eds.), Plenum, N. Y. (1976) 173-391.

[84] Kass S., The development of the zircaloys, Corrosion of Zirconium Alloys[R]. ASTM-STP-368, American Society for Testing and Materials, Conshohocken W., PA. (1964) 3-27.

[85] Cox B., Recent development in zirconium alloy corrosion technology [R]. Progress in Nuclear Energy, Series IV, Technology, Engineering and Safety, Vol.4, Ch.3-3, (Nicholls C. M., Ed.), Pergamon, Oxford, (1961) 166-188.

[86] Cox B. and Roy C., Transport of oxygen in oxide films on zirconium determined by the nuclear reaction O^{17} (He^3, α) O^{16} [J]. Electrochem. Tech., 4 (1966) 121-127.

[87] Cox B. and Pemsler J.P., Diffusion of oxygen in growing zirconia films [J]. J. Nucl. Mater. 28 (1968) 73-78.

[88] Ploc R.A., Transmission of electron microscopy of thin (<200 nm) thermally formed ZrO_2 films [J]. J. Nucl. Mater., 28 (1968) 48-60.

[89] David G., Geschier R and Roy C., Etude de la croissance de l'oxyde sur le zirconium et le Zircaloy-2 [J]. J. Nucl. Mater. 38 (1971) 329-339.

[90] Ploc R.A., Electron diffraction analysis of ZrO_2 on α-Zr (1120) [J]. J. Nucl. Mater., 113 (1983) 75-80.

[91] Ploc R.A., A theoretical treatment of Zr/ZrO_2 epitaxy [R]. Can. Rep. AECL 2751, Atomic Energy of Canada Ltd., Chalk River Nuclear Laboratories (1967).

[92] Godlewski J., Gros J-P., Lambertin M., Wadier J-F and Weidinger H., "Raman spectroscopy study of the tetragonal-to-monoclinic transition in zirconium oxide scales and determination of overall oxygen diffusion by nuclear microanalysis of ^{18}O" [C]. Zirconium in in the Nuclear Industry, 9th Int. Symp., ASTM-STP-1132, (Eueken C. M., Garde A. M., Eds.), American Society for Testing and Materials, W. Conshohocken, PA. (1991) 416-436.

[93] Godlewski J., "How the tetragonal zirconia is stabilized in the oxide scale formed on zirconium alloys corroded at 400°C in steam" [C]. Zirconium in the Nuclear Industry, 10th Int. Symp., ASTM-STP-1245, (Garde A. M., Bradley E. R., Eds.), American Society for Testing and Materials, Conshohocken W., PA. (1994) 663-683.

[94] Peters H.R., Improved characterization of aqueous corrosion kinetics of Zircaloy-4 [C]. Zirconium in the Nuclear Industry, 6th Int. Symp., ASTM-STP-824, (Franklin D.G, Adamson R.B., Eds.), American Society for Testing and Materials, Conshohocken W., PA. (1984) 507-518.

[95] Cox B., Processes occurring during the breakdown of oxide films on zirconium alloys [J]. J. Nucl. Mater., 29 (1969) 50-66.

[96] Bradhurst D.H., Heuer P.M., The influence of oxide stress on the breakaway oxidation of Zircaloy-2 [J]. J. Nucl. Mater., 37 (1970) 35.

[97] Cox B., Comments on the paper, The influence of oxide stress on the breakaway oxidation of Zircaloy-2 [J]. J. Nucl. Mater., 41 (1971) 96-100.

[98] Urbanic V.F. and Gilbert R.W., Effect of microstructure on the corrosion of Zr-2.5%Nb alloy [C]. Proc. Tech. Comm. Mtg. on Fundamental Aspects of Zr Based Alloys in Water Reactor Environment, IWGFPT/34, International Atomic Energy Agency Vienna, (1990) 262-272.

[99] Ambartsumyan R.S., Kiseley A.A., Grebennikov R.V, Myshkin V.A., Tsuprun L.J. and Nikulina A.V., Mechanical properties and corrosion resistance of zirconium and its alloys in water, steam and gases at elevated temperature [C]. Proc. 2nd Int. Conf. on the

Peaceful Uses of Atomic Energy, Geneva, CH, (Aug. 1958), Vol. 6, p. 12, United Nations, New York.

[100] Vrtilkova V., Valach M. and Molin L., Oxiding and hydriding properties of Zr-lNb cladding material in comparison with Zircaloys [C]. Proc. Tech. Comm. Mtg. on Influence of Water Chemistry on Fuel Cladding Behavior, Rez, Czech. ReP., (Oct. 4-8, 1993), IAEA-TECDOC-927, Vienna (1997) 227-251.

[101] B.R.T弗罗斯特主编. 材料科学与技术丛书(10B卷), 核材料(第II部分): 第7章 核应用中的锆合金，赵文金译. 北京: 科学出版社（1999) 17-28.

[102] IAEA-TECDOC-996. Waterside corrosion of zirconium alloys in nuclear power plants [C].

[103] 陈鹤鸣，马春来等编著，核反应堆材料腐蚀及其防护. 北京: 原子能出版社，1984

[104] 杨文斗. 反应堆材料学. 北京: 原子能出版社（2000).

[105] Godlewski J., Gros J.P., Lambertin M., Wadier J.F., Weidingen H. (1991), 9th Int. Conf. Zr Nucl. Ind., Nov. 1990, Kobe, Japan: ASTM-STP 1132. Philadelphia, PA: Am. Soc. Test. Mat., pp. 416-436.

[106] 黄强，锆合金耐腐蚀性能研究综述. 核动力工程 (1996）17: 262.

[107]刘文庆，周邦新.Zr-4合金在LiOH水溶液中腐蚀机理的概述. 核动力工程 (2001）22: 65

[108] Cox B. et al. Transient Effects of Lithium Hydroxide and Boric Acid on Zircaloy Corrosion [J]. J. Nucl. Mater, (1993) 199: 272-284.

[109] Cox B. et al., Dissolution of Zirconium Oxide Films in 300^{o}C LiOH [J]. J. Nucl. Mater, (1995) 224: 169-178.

[110] Ramasubramanian N. et al., Aqueous Chemistry of Lithium Hydroxide and Boric Acid and Corrosion of Zr-4 and Zr-2.5Nb Alloy. Zirconium in the Nuclear Industry: 10th Int. Symp., ASTM STP 1245, in: Grade A.M and Bradley E R Eds. American Society for Testing and Materials, Philadelphia, PA (1994) 378-399.

[111] Pecheur D et al. Zirconium in the Nuclear Industry [C]. 12th Int. Symp., ASTM-STP 1354, in: Bradley E.R and Sabol G.P Eds., America Society for Testing and Materials (1998).

[112] Godlewski J. et al. Raman Spectroscopy Study of the Tetragonal-to-Monoclinic Transition in Oxide Scales and Determination of ^{18}O [C]. Zirconium in the Nuclear Industry

[C]. 9th Int. Symp., ASTM-STP 1132, in: Eucken C M and Grade A M Eds. America Society for Testing and Materials, Philadelphia, PA (1991) 416-435.

[113] 周邦新, 李强等, 锆-4合金在高压釜中腐蚀时氧化膜显微组织的演化. 核动力工程, (2005) 26: 364.

[114] IAEA-TECDOC-996. Waterside corrosion of zirconium alloys in nuclear power plants [C].

[115] Wadman B., Zonghe Lai., Andren.H.O., Nystrom A.L., Rudling P. and Pettersson H., Microstructure of oxide layers formed during autoclave testing of zirconium alloys, Zirconium in the Nuclear Industry, 10th Int. Symp., ASTM STP 1245, (Garde A.M., Bradley E.R., Eds.), American Society for Testing and Materials, W. Conshohocken, PA. 1994, PP. 579-598.

[116] Anada H. and Takeda K., Microstructure of oxide on Zircaloy-4, 1.0Nb Zircaloy-4, and Zircaloy-2 formed in 10.3 MPa steam at 673 K, Zirconium in the Nuclear Industry, 10th Intemational Symposium, ASTM STP 1295, E.R. Bradley and G.P. Sabol, Eds., American Society for Testing and Materials（1996）pp. 35-54.

[117] Lee S.J., Park C.J., Lim Y.S. and Kwon H., Influences of laser surface alloying with niobium (Nb) on the corrosion resistance of Zircaloy-4, Journal of Nuclear Materials（2003）321: 177-183.

[118] Gosmain L., Valot C., Ciosmak D., Sicardy O., Study of stress effects in the oxidation of Zircaloy-4, Solid State Ionics141-142（2001) 633-640.

[119] 周邦新等，水化学对锆合金耐腐蚀性能影响的研究，核动力工程，21 （2000) 439-447.

[120] Barberis P., Zirconia powders and Zircaloy oxide film: tetragonal phase evolution during 400°C autoclave test, Journal of Nuclear Materials，226（1995) 34-43.

[121] Garcia E.A. and Beranger G., Diffusion model for the oxidation of Zircaloy-4 at 400°C in steam. The influence of metallurgical structure (precipitates and grain size), Journal of Nuclear Materials，273（1999) 221-227.

[122] Motta A.T., Yilmazbayhan A., Comstock R.J., Partezana J., Sabol G.P., Lai B. and Zhonghou Cai, Microstructure and growth mechanism of oxide layers formed on Zr

alloys studied with micro-beam synchrotron radiation，Journal of ASTM International，2 (5)（2005) 205-230.

[123] Yilmazbayhan A.，Breval E.，Motta A.T. and Comstock R.J.，Transmission electron microscopy examination of oxide layers formed on Zr alloys，Journal of Nuclear Materials，349（2006) 265-281

[124] Pecheur D.，Godlewski J.，Peybernes J.，Fayette L.，Noe M.，Frichet A. and Kerrec O.，Contribution to the understanding of the effect of the water chemistry on the oxidation kinetics of Zircaloy-4 cladding，Zirconium in the Nuclear Industry，12th Int. Symp.，ASTM STP 1354，Sabol G.P. and Moan G.D. Eds.，American Society for Testing and Materials，West Conshohocken，PA（2000) pp. 793-811.

[125] Jeong Y.H.，Baek J.H.，Kim S.J.，Kim H.G. and Ruhmann H.，Corrosion characteristics and oxide microstructures of Zircaloy-4 in aqueous alkali hydroxide solutions，Journal of Nuclear Materials，270（1999) 322-333.

[126]刘文庆，陈文觉等，水化学对Zr-4合金氧化膜形貌的影响，核动力工程，25 (6)（2004) 517-521.

[127] Pecheur D.，Godlewski J.，Billot P. and Thomazet J.，Microstructure of oxide films formed during the waterside corrosion of the Zircaloy-4 cladding in lithiated environment，Zirconium in the Nuclear Industry，11th Int. Symp.，ASTM STP 1295，Bradley E.R. and Sabol G.P. Eds.，American Society for Testing and Materials（1996）pp. 94-113.

[128] Godlewski J.，How the tetragonal zirconia is stabilized in the oxide scale formed on zirconium alloys corroded at 400°C in steam，Zirconium in the Nuclear Industry，10th Int. Symp.，ASTM-STP-1245 (Garde A.M.，Bradley E.R.，Eds.)，American Society for Testing and Materials，Conshohocken W.，PA. (1994) 663-683.

[129] Bryner J.S., The cyclic nature of corrosion of Zircaloy-4 in 633 K water. Journal of nuclear materials (1979) 82: 84-101.

[130] Cox B., Ungurelu M., Wong Y.M., and Wu C., Mechanisms of LiOH Degradation and H_3BO_3 Repair of ZrO_2 Films, Zirconium in the Nuclear Industry, 11th Int. Symp., ASTM STP 1295, Bradley E.R. and Sabol G.P. Eds., American Society for Testing and Materials (1996) pp. 114-136.

[131周邦新等,锆-4合金在400°C过热蒸汽中均匀腐蚀时出现第二次转折的研究.

核燃料及材料重点实验室年报, 中国核动力研究设计院 (1993) p66.

[132] 杨文斗. 反应堆材料学. 北京: 原子能出版社 (2000).

[133] Pecheur D., Lefebvre F., Motta A.T., Lemaignan C. and Wadier J., J. Nucl. Mater. 189 (1992) 318.

[134] Liu W.Q., Li Q., Zhou B.X. and Yao M.Y., Nuclear Power Engineering (2003) 24(1): p.33-36.

[135] Hillner E., Low A.L. and Perry G.W. (Eds.), Zirconium in the Nuclear Industry, ASTM Spec. Tech. Publ. 633 (1977) p.211.

[136] Zhao W.J., Nuclear Power Engineering (2001) 22(1): p.60-64.

[137] Baek J.H. and. Jeong Y.H. Nucl . Mater.304 (2002) p.107.

[138] Paxton T. and Finnis M.W., Act Materiala, 50 (2002) p.5171.

[139] Takeda K. and Anada H., ASTM STP 1354 (2000) p.592.

[140] Jeong Y.H., Kim H.G. and Kim T.H, J. Nucl. Mater. 317(1), 2003, p 1.

[141] Barberis P., Ahlberg E., Simic N., Charquet D., Lemaignan C., Wikmark **G.**, Dahlback M., Limback M., Tagtstrom P. and Lehtinen B., 13th Int. Symp. on Zirconium in the Nuclear Industry, ASTM STP 1423 (2002) p.33.

[142] R.W.卡恩，P.哈森，E.J.克雷默主编，核应用中的锆合金[M].

材料科学与技术丛书, 核材料，10B卷，科学出版社（1999）1-45.

[143] Zhou B.X., Li Q., Yao M.Y. et al., Effect of Water Chemistry and Composition on Microstructural Evolution of Oxide on Zr Alloys [J]. Journal of ASTM International, Vol.5, No.Paper ID JAI 10112, available online at www.astm.org.

[144] Garvie R.C. and Nicholson P.S. *J. Am. Ceram. Soc*. (1972) 55:303.

[145] Garzarolli F,.Seidel H,.Tricot R,.Gros J.P. in:Proceedings of 9th Int. Symp. on Zirconium in the Nuclear Industry, vol.1132, ASTM-STP (1991) p.395.

[146] Li Zh.K., Liu J.Zh., Zhou L., Li C.and Zhang J.J. Rare Metal Materials and Engineering (2002) 31(4):261-265.

[147] Wang D.N., Guo Y.Q., Liang K.M. and Tao K. Science in China (series A) (1998) 8(9):823-829.

[148] Barberis P., Merle-Méjean T. and Quintard P., On Raman Spectroscopy of Zirconium Oxide Films, Journal of Nuclear Materials, 246 (3), 232 (1997).

[149] Barbéris P., Corolleur-Thomas G., Guinebretière R., Merle-Mejean T., Mirgorodsky A., and Quintard P., Raman Spectra of Tetragonal Zirconia: Powder to Zircaloy Oxide Frequency Shift. Journal of Nuclear Materials, 288 (3), 241(2001).

[150] Godlewski J., Gross J.P., Lambertin M., Wadier J.F. and Weidinger H., Raman Spectroscopy Study of the Tetragonal to Monoclinic Transition in Oxide Scales and Determination of Overall Oxygen Diffusion by Nuclear Microanalysis of O^{18}, in Zirconium in the Nuclear Industry, 9th Int. Symp., edited by Eucken C M and Grade A M., America, ASTM Spec.Tech.Publ.1132 (1991) p.416.

[151] Zhang H., Li Z., Fruchart D., Zhang T., Zhang J., Zhou J. and Zhou L., Rare Metal Materials and Engineering, Crystal Structure Analysis of Oxide Film of New Zirconium Alloys, 35 (12), 1908 (2006).

[152] Arima T., Miyata K., Inagaki Y. and Idemistu K., Oxidation Properties of Zr-Nb Alloys at 500-600℃ under Low Oxygen Potentials, Corrosion Science, 47, 435 (2005)

[153] Arima T. , Miyata K., Inagaki Y., and Idemitsu K., Oxidation Properties of Zr-Nb Alloys at 500-600℃ under Low Oxygen Potentials, Corrosion Science, 47, 435 (2005).

[154] Li Z., Liu J., Zhou L., Li C.and Zhang J., Rare Metal Materials and Engineering, Study on Microstructure of Oxide Film for New Zirconium Alloys, 31 (4), 261 (2002).

[155] Jeong Y.H., Lee K.O.and Kim H.G., Correlation between Microstructure and Corrosion Behaviour of Zr-Nb Binary Alloy, Journal of Nuclear Materials, 302, 9 (2002).

[156] Jeong Y.H., Kim H.G. and Kim T.H., Effect of β Phase precipitate and Nb-concentration in Matrix on Corrosion and Oxide Characteristics of Zr-xNb Alloys, Journal of Nuclear Materials, 317, 1 (2003).

[157] Maroto A.J.G., Bordoni R., Villegas M., Olmedo A.M., Blesa M.A., Iglesias A. and Koenig P., Growth and Characterization of Oxide Layers on Zirconium Alloys, Journal of Nuclear Materials, 229, 79 (1996).

[158] Bouvier P., Godlewski J. and Lucazeau G., A. Raman Study of the Nanocrystallite Size Effect on the Pressure-temperature Phase Diagram of Zirconia Grown by Zirconium-based Alloys Oxidation, Journal of Nuclear Materials, 300, 118 (2002).

[159] Jeong Y.H., Baek J.H., Kim S.J., Kim H.G. and Ruhmann H., Corrosion Characteristics and Oxide Microstructures of Zircaloy-4 in Aqueous Alkali Hydroxide Solution, Journal of Nuclear Materials, 270, 322 (1999).

[160] Pétigny N., Barberis P., Lemaignan C., Valot Ch. and Lallemant G., In Situ XRD Analysis of the Oxide Layers Formed by Oxidation at 743K on Zircaloy-4 and Zr-1NbO, Journal of Nuclear Materials, 280, 318 (2000).

[161] Barberis P., Zirconia Powders and Zircaloy Oxide Films: Tetragonal Phase Evolution during 400℃ Autoclave Tests, Journal of Nuclear Materials, 226, 34 (1995).
[162] Pilling N.B. and Bedworth R.E., J. Inst. Met. 29 (1923) 529.
[163] Dollins C.C. and Jursich M., J. Nucl. Mater. 113 (1983) 19.
[164] Evans H.E., Norfolk D.J. and Swan T., J. Electrochem. Soc.125 (1978) 180.
[165] IAEA-TECDOC-996. Waterside corrosion of zirconium alloys in nuclear power plants[C]. IAEA, Vienna (1998).
[166] 刘文庆, 李强, 周邦新. 锆锡合金腐蚀转折机理的讨论, 稀有金属材料与工程, 30 (2) (2001) 81-84.
[167] Godlewski J., Bouvier P., Lueazeau G., and Fayette L., Stress distribution measured by Raman spectroscopy in Zirconia films formed by oxidation of Zr-based alloys, Zirconium in the Nuelear Industly: Twelfth Int. Symp., ASTM STP 1354, Sabol G.P. and Moan G.D., Eds. Ameriean Soeiety for Testing and Materials, Conshohoeken W., PA (2000) PP. 877-900.
[168] Hong H.S., Kim S.J. and Lee K.S. Long-term oxidation characteristics of oxygen-added modified Zircaloy-4 in 360℃ water, Journal of Nuclear Materials. 273(1999): 177-181.
[169] 刘文庆, 李强, 周邦新, 姚美意. 水化学对Zr-4合金氧化膜/基体界面处压应力的影响, 稀有金属材料与工程, 33 (10) (2004) 1112-1115
[170] 邵淑英, 等. 薄膜应力研究, 激光与光电子学进展, 42 (1) (2005) 22.
[171] Anada H and Takeda K., Proceedings of the 11th Int. Symp. on Zirconium in the Nuclear Industry, ASTM-STP (1996) p.35.
[172] Arima T., Miyata K., Inagaki Y. and Idemitsu K., Corros. Sci.47 (2005) 435.
[173] Zhiyaev A.P. and Szpunar J.A., J. Nucl. Mater.264 (1999) 327.
[174] Glavicic M.G., PhD Thesis, McGill University (1998).
[175] Pétigny N., Barberis P., Lemaignan C., Valot Ch. and Lallemant G., J. Nucl. Mater. 280 (2000) 318.
[176] Oskarsson M., Ahlberg E., Andersson U. and Pettersson K., J.Nucl.Mater.297 (2001) 77
[177] Godlewski J., PhD, UTC Compiègne (1990).
[178] Garzarolli F., Seidel H., Tricot R. and Gros J.P., ASEM-STP 1132 (1991) 395-415.
[179]. Godlewski J. et al., ASTM-STP 1132 (1991) 416.
[180] Bechade J.L. et al., High Temp. Mater. Process. 2 (1998) 359.
[181] Hauk O.V., Adv. X-ray Anal. 39 (1997) 181.
[182] Beie H.J., Mitwalsky A., Garzarolli F., Ruhmann H. and Sell H.J., ASTM-STP 1245 (1994) 615.

[183] Parise M., Sicardy O. and Cailletaud G., J. Nucl. Mater. 256 (1998) 35.
[184] Lin Y.P., Woo O.T. and Lockwood D.J., Mater. Res. Soc. Symp. Proc. 343 (1994) 487.
[185] Bechade J.L. et al., in: Proc. ICRS-5, Linköping, Sweden, 16–18 June 1997.
[186] Kröner E., J. Mech. Phys. Solids 15 (1967) 319.
[187] Reuss A., Z. Angew, Math. Mech. 9 (1929) 49.
[188] Cox B., Kritsky V.G, Lemaignan C. et al., Waterside corrosion of zirconium alloys in nuclear power plants, Tec. Doc 996, IAEA (1998).
[189] Iltis X., Lefebvre F. and Lemaignan C., J. Nucl. Mater. 224 (1995) 109.
[190] Bechade J.L. et al., High Temp. Mater. Process. 2 (1998) 359
[191] Gosmain L., Valot C., Ciosmak D. and Sicardy O., Solid State Ionics, 141-142 (2001) 633-640.
[192] Roy C. and Burgess B., Oxid. Met. 2 (1970) 235.
[193] Godlewski J., Bouvier P., Lucazeau G. and Fayette L., ASEM STP 1354 (2000) 877.
[195] McCullogh J.D. and Trueblood K.N. Acta Crystallogr (1959) 12: 507.
[196] Smith D.K. and Newkirk H.W., Acta Crystallogr (1965) 18: 983.
[197] Howard C.J., Hill R.J. and Reichert B.E.. Acta Crystallogr (1988) B44: 116.
[198] Teufer G., Acta Crystallogr (1962) 15: 1187.
[199] Aldebert P. and Traverse J.P., J. Am. Ceram. Soc (1985) 68: 34.
[200] Ackermann R.J., Garg S.P. and Rauh E.G., J. Am Ceram. Soc. (1977) 60: 341.
[201] Subbarao E.C., Zirconia -an overview. In: Heuer A.H., Hobbs L.W., editors. Science and Technology of Zirconia. Advances in Ceramics, vol. 3. Columbus, OH: The American Ceramic Society (1981).
[202] Grain C.F., J. Am. Ceram. Soc (1967) 50: 288.
[203] Stubican V.S. and Ray S.P., J.Am. Ceram. Soc 1977; 60: 534.
[204] Goff J.P., Hayes W., Hull S., Hutchings M.T. and Clausen K.N., Phys. Rev. B (1999) 59: 14202.
[205] Stefanovich E.V., Shluger A.L. and Catlow C.R.A., Phys. Rev. B (1994) 49: 11560.
[206] Finnis M.W., Paxton A.T., Methfessen M. and van Schilfgaarde M., Phys. Rev. Lett (1998) 81: 5149.
[207] Fabris S., Paxton A.T. and Finnis M.W., Phys. Rev. B (2000) 61: 6617.
[208] Fabris S., Paxton A.T. and Finnis M.W., Phys. Rev. B (2001) 63: 94101.
[209] Li P., Chen I. and Penner-Hahn J.E., Phys. Rev. B (1993) 48: 10063.
[210] Li P., Chen I. and Penner-Hahn J.E., Phys. Rev. B (1993) 48: 10074.
[211] Li P., Chen I. and Penner-Hahn J.E., Phys. Rev. B (1993) 48: 10082.

[212] Li P., Chen I. and Penner-Hahn J.E., J. Am. Ceram. Soc. (1994) 77: 118.

[213]. Li P., Chen I. and Penner-Hahn J.E., J. Am. Ceram. Soc. (1994) 77: 1281.

[214] Li P., Chen I. and Penner-Hahn J.E., J. Am. Ceram. Soc. (1994) 77: 1289.

[215] Stapper G., Bernasconi M., Nicoloso N. and Parrinello M., Phys. Rev. B (1999) 59, 797.

[216] Bogicevic A., Wolverton C., Crosbie G.M. and Stechel E.B., Phys Rev. B (2001) 64, 14106.

[217] Rossell H.J.. J. Solid State Chem (1976) 19: 103.

[218] Stubican V.S., Hink R.C., Ray S.P. J. Am. Ceram. Soc. (1978) 61: 17.

[219] Garzarolli F., Seidsl H., Tricot R. et al. Oxide Growth Mechanism on Zircaloy. In: Eucken C.M. and Grade A.M. eds, Zirconium in the Nuclear Industry, Ninth Int. Symp.[C], Philadelphia: America Society for Testing and Materials (1991) 395.

[220] Zhou B.X. and Jiang Y.R., Oxidation of Zircaloy-2 in air from 500^{o}C to 800^{o}C. In: Guan H.G., Wu W.T., Shen J.N. and Li T.F. eds. High Temperature Corrosion and Protection, Proc Inter Sym [C], Shengyang, China: Liaoning Science and Technology Publishing House (1991) 121.

[221] Godlewski J., How the Tetragonal Zirconia is Stabilized in the Oxide Scale That is Formed on a Zirconium Alloy Corroded at 400^{o}C in Steam. In: Bradley E.R. and Sabol G.P. eds. Zirconium in the Nuclear Industry, 10th Int. Symp.[C], Philadelphia: America Society for Testing and Materials (1994) 663.

[222] Bradhurst D.H. and Heuer P.M., J. Nucl. Mater. 37 (1970) 35-47.

[223] Bradhurst D.H. and Leach J.S.L., Trans. Brit. Ceram.Soc. 62 (1963) 793.

[224] Bradhurst D.H. and Leach J.S.L., J. Electrochem. Soc. 113 (1966) 671.

[225] Zhou B.X., Li Q., Yao M.Y., et al., Effect of Water Chemistry and Composition on Microstructural Evolution of Oxide on Zr Alloys [J]. Journal of ASTM International, Vol. 5, No. (paper ID JAI 10112, available online at www.astm.org).

[226]周邦新，李强，刘文庆，姚美意，褚于良，水化学及合金成分对锆合金腐蚀时氧化膜显微组织演化的影响[J].稀有金属材料与工程35(7) (2006) 1009−1016.

[227] IAEA-TECDOC-996. Waterside corrosion of zirconium alloys in nuclear power plants [C].

[228] Cox B. et al. Transient Effects of Lithium Hydroxide and Boric Acid on Zircaloy Corrosion [J]. J. Nucl. Mater, (1993) 199: 272-284.

[229] Godlewski J. et al. Raman Spectroscopy Study of the Tetragonal-to-Monoclinic Transition in Oxide Scales and Determination of ^{18}O [C]. in the Nuclear Industry [C]. 9th Int. Symp., ASTM-STP 1132, in: Eucken C.M. and Grade A.M. Eds. America Society for Testing and Materials, Philadelphia, PA, (1991) 416-435.

[230] Beie H.J., Mitwalsky A., Garzarolli F. et al, Examination of the Corrosion Mechanisms of Zirconium Alloys [C]. Zirconium in the Nuclear Industry, New York, ASTM STP 1245, (1994) 615-643.

[231] Godlewski J., "How the Tetragonal Zirconia is Stabilised in the Oxide Scale Formed on Zirconium Alloys Corroded at 400°C in Steam", Zirconium in the Nuclear Industry, 10th Int. Symp., ASTM-STP-1245, (Garde A.M., Bradley E.R., Eds.), American Society for Testing and Materials, W.Conshohocken, PA. (1994) 663-683.